Mesoscale Lattice Boltzmann Modelling of Redox-Mediated Electrochemical Systems

A study on modelling reaction-precipitation phenomena through the coupled Poisson-Nernst-Planck equations

Master Thesis

R.H.J.A. Tol



Delft University of Technology

TU Delft

Mesoscale Lattice Boltzmann Modelling of Redox-Mediated Electrochemical Systems

A study on modelling reaction-precipitation phenomena through the coupled Poisson-Nernst-Planck equations

by

R.H.J.A. Tol

to obtain the degree of Master of Science
at the Delft University of Technology.

Student number:	4815726	
Project duration:	September 29th, 2025 – June 23th, 2026	
Thesis committee:	dr. ir. M. Rohde,	TU Delft
	dr. E. M. Kelder,	TU Delft
	dr. K. Chatzipapas,	TU Delft
Supervisor:	dr. ir. M. Rohde,	TU Delft
Daily supervisors:	A. K. Kodyingal,	TU Delft
	dr. M. C. Kwakernaak,	TU Delft

An electronic version of this thesis will be available at `http://repository.tudelft.nl/`.

TU Delft

Preface

This Master thesis was performed as a part of the ReZilient project at the Storage of Electrochemical Energy (SEE) research group in the Radiation Science and Technology (RST) department at the Delft University of Technology (TU Delft) over a planned time span of nine months starting September 2025, none of which would have been possible without my supervisors always having my back.

Anish, for the countless good-spirited arguments we've had over the months, and being my guide through whatever chemistry I struggled to grasp. Throughout many a benchmark, your enthusiasm stayed unmatched, and I can't thank you enough for everything you've done to help me.

Always keeping everyone's spirits up, keeping any situation down-to-earth, derailing every meeting into conversations no-one could ever predict beforehand. Thank you Mark, for having been supportive every step of the way, from laboratory lows to modelling highs.

Thanks Martin, for keeping me thinking like a physicist would and should.

Ruben Tol

Delft, June 2026

Highlights

- A simulation was created using the Lattice Boltzmann Method to simulate the evolution of species inside the charge-carrying bead of a zinc redox-mediated flow battery, including reaction-precipitation phenomena.
- A method was developed to adapt the Poisson equation into a pseudo-transient equation, allowing it to be modelled using the Lattice Boltzmann Method through iteration in pseudo-time.
- A demonstration was performed to show 1) zinc oxide precipitate growing on the zinc particle anode, impacting the current generated by the oxidation reaction taking place at the anode, and 2) the effects of nearby charged zinc particles on their respective electric potentials.

Abstract

As the demand for electrochemical energy storage increases, a need for high-density, safe and cost-effective battery technology is warranted. Zinc redox-mediated flow batteries have the ability to overcome these challenges. The ReZilient project, working on the development of this battery technology, utilizes an approach where the charge transfer between the electrochemical storage and the electrodes is carried out by redox mediator shuttle molecules. The charges these molecules transport originate from beads, which are made up of alginate, carbon black strands and zinc particles. The stored zinc inside the beads undergoes oxidation, producing zincate, which will eventually precipitate as zinc oxide. This zinc oxide can cover the available zinc, impacting the battery's performance.

In this thesis, a simulation is created of this reaction-precipitation phenomena. The simulation simulates the coupled Poisson-Nernst-Planck equations, which dictate the evolution of the species present in the electrolyte and the electric potential. A zinc particle inside a bead is modelled as an anode, confined by carbon-black-alginate and surrounded by electrolyte. The transport of the concentration of each species in the electrolyte is governed by diffusion and migration. A current density is produced when the zinc undergoes oxidation at the anodic boundary, providing for a oxidation molar flux which introduces zincate to the system. The zincate, based on its solubility, is then able to precipitate on a nearby (partly) solid boundary.

The coupled Poisson-Nernst-Planck equations are then recast through the Lattice Boltzmann Method, which discretizes the simulation space and iterates the simulation over discrete time steps. This method is based on kinetic theory, where a framework for the transient Nernst-Planck equation is defined. Only the steady-state solution of the Poisson equation is required by the simulation, but as the Poisson equation is not transient, kinetic theory can not be applied. A pseudo-kinetic theory is conceived, which defines a pseudo-diffusivity coefficient, iterating over the Poisson equation in pseudo-time until it reaches pseudo-steady-state. The (pseudo-)kinetic interactions are described by the Bhatnagar–Gross–Krook collision operator, which implements the (pseudo-)diffusivity through the use of a relaxation (pseudo-)time. The simulation is then defined, consisting of multiple solvers to obtain the macroscopic quantities required for the two Lattice Boltzmann Method models; one to iterate over the concentration, and one to iterate over the electric potential.

The equations following from the Lattice Boltzmann Method are then re-written to be in dimensionless units based on the characteristic values of the quantities involved. Here, the restrictions of the discretization process and the impact of the relaxation (pseudo-)time are emphasised. The simulation is then benchmarked to verify its validity. The benchmarking process first compares a one-dimensional steady-state analytical solution for the coupled Poisson-Nernst-Planck equations against the Lattice Boltzmann Method models, where no reactions take place. First, the models are benchmarked separately to observe the effects of the relaxation (pseudo-)time on the deviation from the analytical solutions. This yields preferred values for the relaxation (pseudo-)time to run the simulation with; this is then confirmed by having the two models run in a combined simulation. The simulation shows to be conform with the analytical solution. The one-dimensional simulation is then ran including reactions (but no precipitation) and is compared to a COMSOL simulation running under the same conditions, where similar behaviour between the simulations is observed.

The full two-dimensional simulation is then ran including reactions and precipitation, where the growth of precipitate is observed. A drop in current is observed as the anode gets progressively more covered in precipitate. The simulation is repeated, where now the domain is exposed to an external electric field to observe the effects on the precipitation growth, which were minimal.

Nomenclature

Abbreviations

BGK	Bhatnagar-Gross-Krook
EDL	Electric Double Layer
EES	Electrochemical Energy Storage
LBM	Lattice Boltzmann Method
LIB	Lithium-Ion Battery
PNP	Poisson-Nernst-Planck
RFB	Redox Flow Battery
RMFB	Redox-Mediated Flow Battery
RMSE	Root Mean Square Error
SSRFB	Semi-Solid Redox Flow Battery

Physical Constants

ϵ_0	Vacuum permittivity	$8.854 \times 10^{-12}\,\mathrm{C\,V^{-1}\,m^{-1}}$
e	Elementary charge	$1.602 \times 10^{-19}\,\mathrm{C}$
F	Faraday constant	$96.485\,\mathrm{C\,mol^{-1}}$
k_B	Boltzmann constant	$1.381 \times 10^{-23}\,\mathrm{V\,C\,K^{-1}}$
R	Gas constant	$8.314\,\mathrm{V\,C\,mol^{-1}\,K^{-1}}$

Unit Conversion Factors

$\mathcal{C}$	Charge conversion factor	C
$\mathcal{D}$	Degrees of temperature conversion factor	K
$\mathcal{M}$	Mole conversion factor	mol
$\mathcal{P}$	Potential conversion factor	V
$\mathcal{S}$	Space conversion factor	m
$\mathcal{T}$	Time conversion factor	s
$\mathcal{V}$	Variable conversion factor	*
a	Unit exponent	–

Symbols

$\delta\Omega$	Boundary set
Γ	Boundary
Ω	Domain
d	Dimension
q	Number of lattice vector directions
DdQq	Velocity set

Indices

i	Species
j	Discretized velocity direction

Physical Variables

α_a	Anodic charge transfer coefficient	–
ΔG	Gibbs free energy	$\mathrm{V\,C}$
ϵ	Permittivity	$\mathrm{C\,V^{-1}\,m^{-1}}$
η	Overpotential	V
κ	Conductivity	$\mathrm{C\,V^{-1}\,m^{-1}\,s^{-1}}$
$\mathbf{E}$	Electric field	$\mathrm{V\,m^{-1}}$
$\mathbf{F}$	Force	$\mathrm{V\,C\,m^{-1}}$
$\mathbf{J}$	Current density	$\mathrm{C\,m^{-2}\,s^{-1}}$
$\mathbf{N}$	Molar flux	$\mathrm{mol\,m^{-2}\,s^{-1}}$
$\mathbf{u}$	Velocity (2D)	$\mathrm{m\,s^{-1}}$
$\mathbf{x}$	Position (2D)	m
μ	Ionic strength	$\mathrm{mol\,m^{-3}}$
ν	Stoichiometric coefficient	–
ϕ	Electric potential	V
ρ	Charge density	$\mathrm{C\,m^{-3}}$
θ	Angle	–
A	Area	$\mathrm{m^2}$
c	Concentration	$\mathrm{mol\,m^{-3}}$
D	Diffusivity	$\mathrm{m^2\,s^{-1}}$
E	Oxidation potential	V
I	Current	$\mathrm{C\,s^{-1}}$
J	Current density	$\mathrm{C\,m^{-2}\,s^{-1}}$
K	Solubility constant	$\mathrm{mol\,m^{-3}}$
k	Reaction rate	$\mathrm{s^{-1}}$
M	Molar volume	$\mathrm{m^3\,mol^{-1}}$
N	Molar flux	$\mathrm{mol\,m^{-2}\,s^{-1}}$
n	Number of moles of electrons	–
p	Precipitate fraction	–
Q	Reaction quotient	–
S	Source/Sink term	$\mathrm{mol\,m^{-3}\,s^{-1}}$
T	Temperature	K

t	Time	s
u	Velocity (1D)	$\mathrm{m\,s^{-1}}$
V	Volume	$\mathrm{m^3}$
x	Position (1D)	m
z	Valence	–

LBM Variables

$\boldsymbol{\xi}$	Particle velocity	$\mathrm{m\,s^{-1}}$
$\boldsymbol{\zeta}$	Potential pseudo-velocity	m
χ	Pseudo-diffusivity	$\mathrm{m^2}$
Δt	Time step	s
Δx	Lattice spacing	m
δ	Threshold	–
γ	Scaling constant	–
$\mathbf{e}$	Lattice vector	$\mathrm{m\,s^{-1}}$
Φ	Potential collision operator	$\mathrm{V\,m^{-3}\,s^{-1}}$
Ψ	Particle collision operator	$\mathrm{mol\,m^{-3}\,s^{-1}}$
σ	Relaxation pseudo-time	–
τ	Relaxation time	s
ε	Convergence	–
f	Particle distribution function	$\mathrm{mol\,m^{-3}}$
g	Potential distribution function	V
H	Domain height	m
h	Lattice height	–
L	Domain length	m
l	Lattice length	–
s	Pseudo-time	–
v	Lattice speed	$\mathrm{m\,s^{-1}}$
w	Lattice vector weight	–

Contents

1 Introduction **1**
- 1.1 Electrochemical Energy Storage 1
  - 1.1.1 Lithium-Ion Battery Technology . 1
  - 1.1.2 Redox Flow Battery Technology . 1
  - 1.1.3 Redox-Mediated Flow Battery Technology 2
- 1.2 Zinc Redox-Mediated Flow Batteries . . . 2

2 Electrochemistry **4**
- 2.1 Defining the Simulation Space 4
  - 2.1.1 The Domain 4
  - 2.1.2 The Boundaries 4
- 2.2 Anodic Reactions 5
  - 2.2.1 Oxidation 5
  - 2.2.2 Precipitation 7
- 2.3 Transport Phenomena 8
  - 2.3.1 Diffusion 8
  - 2.3.2 Advection and Migration 8
  - 2.3.3 The Nernst-Planck Equation . . . 8
- 2.4 Electrostatics 9
  - 2.4.1 The Poisson Equation 9
  - 2.4.2 Migration 9
  - 2.4.3 Conductivity 10
  - 2.4.4 The Electric Double Layer 10
- 2.5 System Constraints 11
  - 2.5.1 Initial Conditions 11
  - 2.5.2 Boundary Conditions 11
- 2.6 The Poisson-Nernst-Planck Equations . . 12

3 Discretization **13**
- 3.1 Kinetic Theory 13
  - 3.1.1 Mesoscopic Interactions 14
  - 3.1.2 Boltzmann Kinetics 14
  - 3.1.3 Pseudo-Kinetic Theory 15
- 3.2 The Lattice Boltzmann Method 17
  - 3.2.1 Grid Discretization 17
  - 3.2.2 Initialization 19
  - 3.2.3 Computation 19
  - 3.2.4 Relaxation 20
  - 3.2.5 Propagation 20
  - 3.2.6 Iteration 22
- 3.3 The Simulation Solvers 24
  - 3.3.1 The Electrostatics Solver 24
  - 3.3.2 The Electrokinetics Solver 24
  - 3.3.3 The Migrative Velocity Solver . . . 24
  - 3.3.4 The Precipitation Kinetics Solver . 25

4 Non-Dimensionalization **26**
- 4.1 Unit Conversion Factors 26
- 4.2 Non-Dimensional Numbers and Restrictions 28
  - 4.2.1 Propagation Limits 28
  - 4.2.2 Relaxation Time Limits 28
  - 4.2.3 Resolution Limits 29
- 4.3 Non-Dimensional Equations 29

5 Benchmarking **32**
- 5.1 Gouy-Chapman Theory 33
- 5.2 Analytical Benchmarks 33
  - 5.2.1 $c_i(t)$-LBM Model Benchmark . . . 35
  - 5.2.2 $\phi(s)$-LBM Model Benchmark . . . 38
  - 5.2.3 Combined $c_i(t)$-LBM and $\phi(s)$-LBM Models Benchmark 41
- 5.3 COMSOL Benchmark 43

6 Application **46**
- 6.1 Precipitation Demonstration 47
- 6.2 External Electric Potential Demonstration 55
  - 6.2.1 Perpendicular Electric Potential . 56
  - 6.2.2 Diagonal Electric Potential 61
  - 6.2.3 Parallel Electric Potential 66

7 Discussion **71**
- 7.1 Validation and Practicality 71
  - 7.1.1 Resolution Limitations 71
  - 7.1.2 Analytical Conformity 71
  - 7.1.3 COMSOL Discrepancy 71
  - 7.1.4 Precipitation Evolution 72
- 7.2 Further Research 72
  - 7.2.1 Relaxation Time Dependency . . . 72
  - 7.2.2 Experimental Verification 72
  - 7.2.3 Mediator Molecule Precipitation . 72
  - 7.2.4 Precipitation Methodology 73
  - 7.2.5 GPU Acceleration 73

8 Conclusion **74**

A Appendix **75**
- A.1 On the Process of Non-Dimensionalization 75
- A.2 Effects of the Relaxation (Pseudo-)time on the (Pseudo-)Steady-State Solutions . . . 75

Bibliography **78**

1 Introduction

1.1 Electrochemical Energy Storage 1
1.1.1 Lithium-Ion Battery Technology 1
1.1.2 Redox Flow Battery Technology 1
1.1.3 Redox-Mediated Flow Battery Technology 2
1.2 Zinc Redox-Mediated Flow Batteries 2

The demand for electrochemical energy storage (EES) is increasing as the energy transition accelerates. In this section, the need for EES is explained, followed by an overview of EES technology and research. An emphasis on zinc redox-mediated flow battery (ZRMFB) technology is made, where the aim of this thesis is introduced.

1.1 Electrochemical Energy Storage

The stability of a (hybrid) power system is crucial to enable the supply and demand of power over the grid. The hybrid grid, through its accompaniment of solar and wind energy generation, faces significant fluctuations in grid stability due to varying solar intensity and wind speeds impacting the amount of power generated. To improve the stability of the hybrid grid, (stationary) electrochemical energy storage (EES) is deployed to deal with the fluctuations in power generation, storing and releasing excess energy when necessary.[1,2]

1.1.1 Lithium-Ion Battery Technology

The most prevailing EES battery technology of the past decades have been lithium-ion batteries (LIB). LIBs use lithium ions (Li^+) as charge carriers, where Li^+ is introduced within LIBs by lithiated metal oxide cathodes, a high-density charge carrier storage medium. A regular issue LIBs face regards the metal oxide cathode degrading throughout its cycling life, which enables excess Li^+ to engage in side reactions, forming crystal dendrites at the anode. These crystal formations pose thermal and short-circuit safety risks, and also cut out available Li^+ to be cycled, reducing the battery capacity over time. To still enable sufficient battery capacity, the electrodes are required to be scaled with the charge carrier storage, which is expensive. LIBs therefore do not suit the longer term needs for stationary EES whilst remaining safe and cost-effective.[2,3,4,5]

1.1.2 Redox Flow Battery Technology

Redox flow battery (RFB) technology is able to overcome the downsides of LIBs when used for stationary EES by separating the energy storage from the electrode interface. RFBs have their charge-carrying ions kept separate from the electrodes in storage tanks, where the ions continually flow between these tanks and the electrodes of the battery. Battery technologies such as the vanadium RFB (VRFB) is able to overcome the safety risks imposed by LIB technology by having all charge-carrying ions be kept aqueous albeit at a lower energy density. Lithium semi-solid RFB (SSRFB) are able to overcome the capacity limitations of LIBs through the use of a more viscous electrolyte, losing efficiency through higher battery operation requirements.[4,6,7,8,9]

1.1.3 Redox-Mediated Flow Battery Technology

Redox-mediated flow battery (RMFB) technology are able to overcome the disadvantages of using charge-carrying particles through the use of redox mediator molecules. These mediator molecules now take the role of transporting the charges between the charge carriers and the electrode, while the charge carriers remain inside the storage tank. The electrolyte now no longer requires to be as viscous as with SSRFBs, offering an increase in efficiency by requiring less power to be spent on pumping. This battery technology approach allows for both high energy densities and high efficiency.[9,10]

1.2 Zinc Redox-Mediated Flow Batteries

Of interest to us are the zinc redox-mediated flow batteries (ZRMFBs) developed by the ReZilient project (see Figure 1.1). On this type of ZRMFBs specifically, a relatively low amount of research has been performed. The performance of these ZRMFBs relies on the charge transfer through the electrolyte between zinc-carrying beads and redox mediator shuttle molecules. These zinc-carrying beads are made of alginate, carbon black strands, and high-density zinc particles (see Figure 1.2). They are porous and highly conductive, allowing the zinc particles to undergo oxidation through exposure to the electrolyte, having the released charge be conducted throughout the bead throughout carbon black connections. These charges are then transferred to the redox mediator shuttle molecules at the surface of the beads, which can then transport these charges through the electrolyte to the electrode.[11]

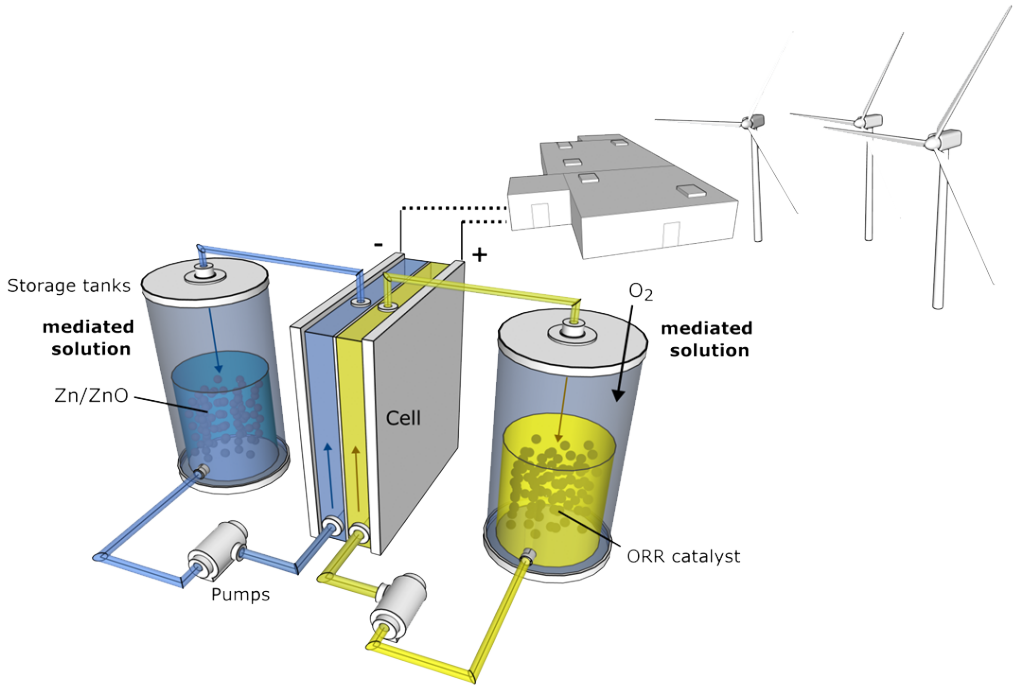


Figure 1.1: Schematic of a zinc-mediated flow battery (ZRMFB), and their EES application. The zinc (Zn) is contained as particle in beads, which themselves are stored inside a storage tank. After the zinc undergoes oxidation, their charges are transferred to redox mediator shuttle molecules present in the mediated solution, which is pumped from the storage tank to the electrode and back.[11]

The oxidation reaction using up the zinc in the beads is therefore of interest, including the precipitation of zincate to zinc oxide (ZnO), which impacts the performance of ZRMFBs. As many electrochemical processes take place simultaneously, it is therefore of interest to have a computer simulation or ”digital twin” be developed, to be able to simulate the charge transfer in ZRMFBs.

1.2
Zinc Redox-Mediated Flow Batteries

Through taking inspiration from past studies, this thesis develops a new approach to modelling the redox-mediated reaction-precipitation phenomena inside ZRMFBs through the creation of a simulation in the Julia programming language. First, the theory regarding the relevant electrochemistry is covered in Section 2, where the coupled Poisson-Nernst-Planck equations are introduced. A way to solve the coupled equations is given in Section 3, where the lattice Boltzmann method is used to discretize the simulation domain and all governing equations through kinetic theory. Following the discretization process, the simulation is converted to run in dimensionless units in Section 4, yielding the finalized version of the simulation. The simulation is the benchmarked in Section 5 against analytical steady-state solutions for the coupled Poisson-Nernst-Planck equations and a COMSOL simulation. After the simulation is shown to yield accurate results, the simulation is applied to show the evolution of reaction-precipitation phenomena in Section 6. This is followed by a discussion on the simulation in Section 7, where conclusions are drawn in Section 8.

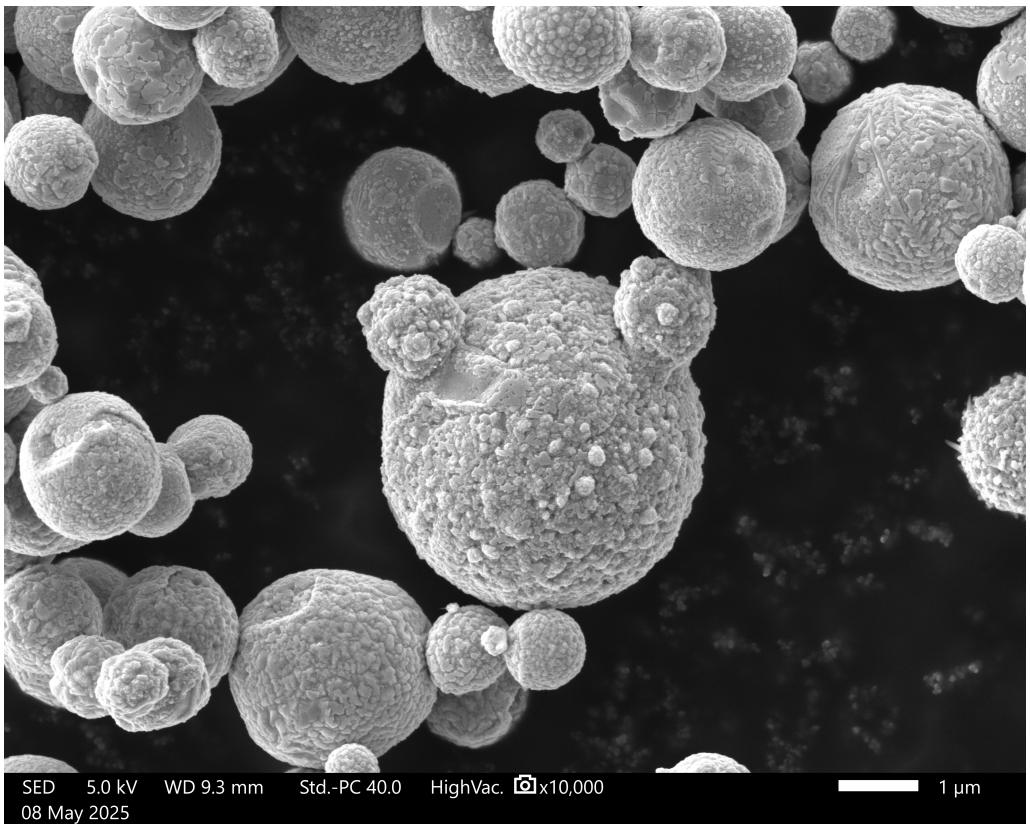


Figure 1.2: SEM image taken of zinc powder. These zinc particles are contained inside the beads. Parts of the particles have already undergone oxidation, and are covered in zinc oxide.

2 Electrochemistry

2.1 Defining the Simulation Space 4
2.1.1 The Domain 4
2.1.2 The Boundaries 4
2.2 Anodic Reactions 5
2.2.1 Oxidation 5
2.2.2 Precipitation 7
2.3 Transport Phenomena 8
2.3.1 Diffusion 8
2.3.2 Advection and Migration 8
2.3.3 The Nernst-Planck Equation 8
2.4 Electrostatics 9
2.4.1 The Poisson Equation 9
2.4.2 Migration 9
2.4.3 Conductivity 10
2.4.4 The Electric Double Layer 10
2.5 System Constraints 11
2.5.1 Initial Conditions 11
2.5.2 Boundary Conditions 11
2.6 The Poisson-Nernst-Planck Equations 12

In this section, all equations regarding the evolution of species in a battery cell are laid out. The main source for this section has been "Electrolysers, Fuel Cells and Batteries: Analytical Modelling" by W. Haverkort.[12]

2.1 Defining the Simulation Space

As we are only interested in the reaction-precipitation phenomena taking place inside a ZRMFB, the simulation concerns only a small section on the inside of a bead, referred to as the domain Ω.

2.1.1 The Domain

The domain Ω refers to a small, three-dimensional slice taken inside the bead. This slice contains a zinc particle, which is partially exposed to the electrolyte, and is surrounded by an alginate/carbon-black mixture. All aqueous species are present in the electrolyte, and the alginate/carbon-black mixture is assumed to be solid and non-reactive. Inside the domain Ω, the initial conditions of the simulation are imposed at a time of $t = 0$.

2.1.2 The Boundaries

The boundary of the domain $\delta\Omega$ consists of three types of boundary Γ:

- the anodic boundary Γ_{a}, which refers to the reactive anode/the zinc particle;
- the bulk boundary Γ_{b}, which refers to the non-solid bounds placed on the simulation inside the electrolyte;
- the carbon-black-alginate boundaries Γ_{c}, which refer to the non-reactive, solid bounds on the simulation which surrounds the anode.

The boundary of the domain $\delta\Omega$ is then fully described by these boundaries: $\delta\Omega = \Gamma_{\mathrm{a}} \cup \Gamma_{\mathrm{b}} \cup \Gamma_{\mathrm{c}}$.

2.2 Anodic Reactions

The aqueous species present in the electrolyte are able to flow freely throughout the domain Ω, and are able to undergo oxidation and precipitation depending on the boundaries Γ they interact with. These aqueous species i present in the electrolyte are

- potassium (K^+) and
- hydroxide (OH^-), which make up the electrolyte in equal parts, and
- zincate ($Zn(OH)_4{}^{2-}$), which is formed at the anode.

Throughout the thesis, the electrolyte is assumed to consist of water, where KOH is added to have the electrolyte reach a pH of 11, yielding bulk concentrations of $c_{K^+,0} = c_{OH^-,0} = 1\,\mathrm{mol\,m^{-3}}$.

2.2.1 Oxidation

When the ZRMFB is discharging, zinc (Zn) is oxidised, forming tetrahydroxozincate ($Zn(OH)_4{}^{2-}$), more commonly referred to as zincate:[13,14]

$$Zn\,(s) + 4\,OH^-(aq) \longrightarrow Zn(OH)_4{}^{2-}(aq) + 2\,e^- \text{with } E^\circ = -1.199\,V, \tag{2.1}$$

where E° is the standard oxidation potential for the zinc oxidation.

The oxidation of Zn releases two electrons (e^-). It is assumed that the charges are conducted through the carbon black strands present in the bead. On the surface of the beads, the electrons are able to be transferred to the mediator molecule ferricyanide ($[Fe(CN)_6]^{3-}$), forming ferrocyanide ($[Fe(CN)_6]^{4-}$):

$$[Fe(CN)_6]^{3-}\,(aq) + e^- \longrightarrow [Fe(CN)_6]^{4-}\,(aq). \tag{2.2}$$

The electrons released through oxidation (see Equation 2.1) flow into the anode, and the zincate ions flow away from the anode. The flux of charge is expressed through the current density $\mathbf{J}$, and the flux of zincate is expressed through the oxidation molar flux $\mathbf{N}_i^{ox}$, which both are defined at a position $\mathbf{x}$ on the anode: $\mathbf{x}_a \in \Gamma_a$. These flows are assumed to be perpendicular to the surface of the anode (see Figure 2.1), yielding their magnitudes as[12]

$$J(\mathbf{x}_a, t) = |\mathbf{J}(\mathbf{x}_a, t)|; \tag{2.3}$$

$$N_i^{ox}(\mathbf{x}_a, t) = |\mathbf{N}_i^{ox}(\mathbf{x}_a, t)|. \tag{2.4}$$

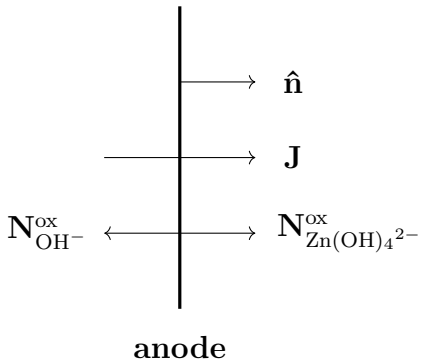


Figure 2.1: The normal to the anode $\hat{\mathbf{n}}$, the current density $\mathbf{J}$, and the two oxidation molar fluxes $\mathbf{N}^{ox}_{Zn(OH)_4{}^{2-}}$ and $\mathbf{N}^{ox}_{OH^-}$.

The oxidation molar flux $\mathbf{N}_i^{\text{ox}}$ is governed by the current density $\mathbf{J}$, with their proportionality given by Faraday's law:[12,15]

$$\mathbf{N}_i^{\text{ox}}(\mathbf{x}_\text{a}, t) = \mathbf{J}(\mathbf{x}_\text{a}, t)\frac{\nu}{nF}, \tag{2.5}$$

where ν is the stoichiometric coefficient of the species i, $n = 2$ is the charge number equal to the released amount of electrons, and F is Faraday's constant.

The current density $\mathbf{J}$ is driven by the overpotential η through the Tafel equation[i] as[12,16]

$$\mathbf{J}(\mathbf{x}_\text{a}, t) = \mathbf{J}_0 \exp\!\left(\frac{\alpha_\text{a} F}{RT}\eta(\mathbf{x}_\text{a}, t)\right), \tag{2.6}$$

where $\mathbf{J}_0$ is the exchange current density (which is a reaction dependent value), α_a the anodic charge transfer coefficient[ii], R the universal gas constant, and T the temperature.

The overpotential η describes the difference between the solid electric potential of the anode ϕ_s and the liquid electric potential near the anode ϕ_l, from now on referred to as just ϕ, relative to the oxidation potential E_ox:[12]

$$\eta(\mathbf{x}_\text{a}, t) = \phi_\text{s} - \phi(\mathbf{x}_\text{a}, t) - E_\text{ox}(\mathbf{x}_\text{a}, t). \tag{2.7}$$

The oxidation potential E_ox is dependent on the reaction quotient Q[iii] near the anode, which is described by the Nernst equation as[16]

$$E_\text{ox}(\mathbf{x}_\text{a}, t) = E_\text{ox}^\circ + \frac{RT}{nF}\ln Q(\mathbf{x}_\text{a}, t), \tag{2.8}$$

$$Q(\mathbf{x}_\text{a}, t) = \frac{c_{\text{Zn(OH)}_4{}^{2-}}(\mathbf{x}_\text{a}, t)}{c^4_{\text{OH}^-}(\mathbf{x}_\text{a}, t)} \cdot 10^9\,\text{mol}^3/\text{m}^9 \tag{2.9}$$

The oxidation potential E_ox acts as a measure for the reaction rate at which Equation 2.1 takes place, where a higher oxidation potential E_ox results in a higher overpotential η, which results in a higher current density J and therefore a higher oxidation molar flux N_i^{ox}.

The oxidation potential E_ox also acts as a threshold for if Equation 2.1 is able to take place spontaneously. This is expressed through the Gibbs free energy:[12]

$$\Delta G(\mathbf{x}_\text{a}, t) = -nFE_\text{ox}(\mathbf{x}_\text{a}, t). \tag{2.10}$$

When $\Delta G < 0$, the reaction is able to occur spontaneously; It follows then that $E_\text{ox} > 0$ is the required potential for the oxidation reaction to take place at the anode.[12]

[i] The Tafel equation is an approximation of the Butler-Volmer equation, which describes the current density over both the anode and the cathode. As we're only concerned with the anode, the Tafel equation is used, which only describes the current density at the anode.[12]

[ii] The anodic charge transfer coefficient is assumed to be constant and equal to $\alpha_\text{a} = 0.5$.[12]

[iii] Q has concentrations in mol/L. They are converted here to mol/m^3 by multiplying with $10^9\,\text{mol}^3/\text{m}^9$.

2.2.2 Precipitation

As the battery operates, zinc continues to oxidise into zincate. When the zincate concentration $c_{\mathrm{Zn(OH)_4{}^{2-}}}$ locally becomes too high, the zincate in the electrolyte is able to saturate, precipitating into zinc oxide (ZnO)[iv]:[13,17]

$$\mathrm{Zn(OH)_4{}^{2-}(aq)} \longrightarrow \mathrm{ZnO\ (s) + 2\,OH^-\ (aq) + H_2O\ (l)} \tag{2.11}$$

The solubility product K of zincate depends on the standard Gibbs free energy of reaction $\Delta G^\circ_{\mathrm{rxn}}$. This itself depends on the standard Gibbs free energy of formation $\Delta G^\circ_{\mathrm{f}}$ of the species involved in Equation 2.11:[17]

$$\Delta G^\circ_{\mathrm{rxn}} = \Delta G^\circ_{\mathrm{f,Zn(OH)_4{}^{2-}}} - (\Delta G^\circ_{\mathrm{f,ZnO}} + 2\Delta G^\circ_{\mathrm{f,OH^-}} + \Delta G^\circ_{\mathrm{f,H_2O}}), \tag{2.12}$$

$$\Delta G^\circ_{\mathrm{rxn}} = -RT\ln K \Longrightarrow K = \exp\left(-\frac{\Delta G^\circ_{\mathrm{rxn}}}{RT}\right). \tag{2.13}$$

The precipitation of zincate into zinc oxide then takes place whenever the concentration of zincate $c_{\mathrm{Zn(OH)_4{}^{2-}}}$ exceeds the solubility constant K. It is assumed that this takes place at a constant rate k. This yields a source/sink term S_i for the involved species i with respective stoichiometry ν_i following from Equation 2.11 as[18]

$$\begin{cases} S_i(\mathbf{x},t) = \nu_i k(c_{\mathrm{Zn(OH)_4{}^{2-}}}(\mathbf{x},t) - K), & c_{\mathrm{Zn(OH)_4{}^{2-}}} > K; \\ S_i(\mathbf{x},t) = 0, & c_{\mathrm{Zn(OH)_4{}^{2-}}} \leq K. \end{cases} \tag{2.14}$$

The zinc oxide precipitates as a solid, covering the exposed area A of the anode, reducing the amount of oxidation reactions able to take place, therefore impacting the current I of the bead:

$$I(t) = \iint_A \mathbf{J}(\mathbf{x},t)\cdot\hat{\mathbf{n}}\,\mathrm{d}A. \tag{2.15}$$

The precipitate at a position $\mathbf{x}$ occupies a volume V based on its molar volume M. The fraction p_{ZnO} of a volume V occupied by solid zinc oxide obtained by integrating the source/sink term S_{ZnO} over a span of time t:[18]

$$p(\mathbf{x},t) = M\int_t S_{\mathrm{ZnO}}(\mathbf{x},t)\,\mathrm{d}t. \tag{2.16}$$

This precipitate fraction p equals the amount of the zinc oxide which occupied volume V at a position $\mathbf{x}$. Aqueous species i can then still flow through the zinc oxide based on its precipitate fraction p, which ranges from 0 (no precipitate) to 1 (only precipitate)

A restraint placed on the precipitation of zincate to zinc oxide is the availability of a solid bound nearby for the precipitation to take place. We allow Equation 2.11 to take place only on the anodic boundary Γ_{a}, the carbon-black-alginate boundaries Γ_{c}, and next to positions $\mathbf{x}$ where the precipitate fraction p is high enough where precipitation can take place on the nearly-solid zinc oxide itself: $p \geq p_{\min}$.

[iv] The electrolyte comprises mainly of water (H_2O) — this will not be modelled, even if it is a product of the precipitation of zincate to zinc oxide (see Equation 2.11), as H_2O does not impact the simulation at any point.

2.3 Transport Phenomena

The transport of a species i in the electrolyte can be described through the following continuity equation:[12]

$$\frac{\partial c_i(\mathbf{x},t)}{\partial t} = -\nabla \cdot \mathbf{N}_i(\mathbf{x}_\mathrm{a},t) + S_i(\mathbf{x},t), \tag{2.17}$$

where c_i is the concentration, and $\mathbf{N}_i$ the Nernst-Planck molar flux.

The Nernst-Planck molar flux $\mathbf{N}_i$ is comprised of three components, a diffusive molar flux $\mathbf{N}_i^\mathrm{d}$, an advective molar flux $\mathbf{N}_i^\mathrm{a}$, and a migrative molar flux $\mathbf{N}_i^\mathrm{m}$:[12,16]

$$\mathbf{N}_i(\mathbf{x},t) = \mathbf{N}_i^\mathrm{d}(\mathbf{x},t) + \mathbf{N}_i^\mathrm{a}(\mathbf{x},t) + \mathbf{N}_i^\mathrm{m}(\mathbf{x},t). \tag{2.18}$$

2.3.1 Diffusion

The diffusive molar flux $\mathbf{N}_i^\mathrm{d}$ is given by

$$\mathbf{N}_i^\mathrm{d}(\mathbf{x},t) = -D_i \nabla c_i(\mathbf{x},t), \tag{2.19}$$

where D_i is the diffusivity of the species i.

The diffusive molar flux $\mathbf{N}_i^\mathrm{d}$ drives a species i to spread out from a region of higher concentration c_i to one lower, where the diffusivity D_i is the rate at which this occurs in the electrolyte.

2.3.2 Advection and Migration

The advective molar flux $\mathbf{N}_i^\mathrm{a}$ and the migrative molar flux $\mathbf{N}_i^\mathrm{m}$ are given by similar equations:[12]

$$\mathbf{N}_i^\mathrm{a}(\mathbf{x},t) = \mathbf{u}^\mathrm{a}(\mathbf{x},t) c_i(\mathbf{x},t); \tag{2.20}$$

$$\mathbf{N}_i^\mathrm{m}(\mathbf{x},t) = \mathbf{u}_i^\mathrm{m}(\mathbf{x},t) c_i(\mathbf{x},t), \tag{2.21}$$

where $\mathbf{u}^\mathrm{a}$ is the advective flow velocity and $\mathbf{u}_i^\mathrm{m}$ is the migrative velocity of a species i.

The diffusive molar flux $\mathbf{N}_i^\mathrm{a}$ drives particles through the advective flow velocity $\mathbf{u}^\mathrm{a}$, which is a velocity which acts on the entire electrolyte. It is assumed, however, that there exists no advective flow velocity in the electrolyte ($\mathbf{u}^\mathrm{a} = \mathbf{0}$), therefore $\mathbf{N}_i^\mathrm{a} = \mathbf{0}$.

Subsection 2.4 expands further on the migrative molar flux $\mathbf{N}_i^\mathrm{m}$ and the migrative velocity $\mathbf{u}_i^\mathrm{m}$.

2.3.3 The Nernst-Planck Equation

We can substitute Equation 2.18, Equation 2.19, Equation 2.20 and Equation 2.21 into Equation 2.17 to yield the Nernst-Planck equation:[12]

$$\frac{\partial c_i(\mathbf{x},t)}{\partial t} = -\nabla \cdot (D_i \nabla c_i(\mathbf{x},t) + \mathbf{u}_i^\mathrm{m} c_i(\mathbf{x},t)) + S_i(\mathbf{x},t). \tag{2.22}$$

The Nernst-Planck equation describes the evolution of a species i in the electrolyte.

2.4 Electrostatics

As we're dealing with ionic species, their charges affect their transport through the electrolyte through repulsion and attraction. This is expressed through the electric potential ϕ and the migrative velocity $\mathbf{u}_i^{\mathrm{m}}$, which follows as a result of it.

2.4.1 The Poisson Equation

The liquid electric potential ϕ in the electrolyte is obtained through Poisson's equation:[19]

$$\nabla^2\phi(\mathbf{x},t) = -\frac{\rho(\mathbf{x},t)}{\epsilon}, \tag{2.23}$$

where ρ is the (free) charge density, and ϵ the permittivity of the electrolyte.

Note how the Poisson equation is time-independent. It is, however, quasi-static, as the charge density ρ depends on the concentrations c_i, which are transient. The charge density ρ is obtained by summing up the charges all ions carry within the electrolyte:[12]

$$\rho(\mathbf{x},t) = F\sum_i z_i c_i(\mathbf{x},t). \tag{2.24}$$

Substituting Equation 2.23 into Equation 2.24 yields

$$\nabla^2\phi(\mathbf{x},t) = -\frac{F}{\epsilon}\sum_i z_i c_i(\mathbf{x},t). \tag{2.25}$$

2.4.2 Migration

The gradient in the electric potential ϕ yields an electric field $\mathbf{E}$. This electric field $\mathbf{E}$ yields a Coulomb force $\mathbf{F}$, which acts on the ions:[12]

$$\mathbf{E}(\mathbf{x},t) = -\nabla\phi(\mathbf{x},t); \tag{2.26}$$

$$\mathbf{F}(\mathbf{x},t) = z_i e\mathbf{E}(\mathbf{x},t), \tag{2.27}$$

where e is the elementary charge.

The Coulomb force $\mathbf{F}$ then causes the migrative velocity $\mathbf{u}_i^{\mathrm{m}}$, which is given through the Einstein-Smoluchowski relation:[12]

$$\mathbf{u}_i^{\mathrm{m}}(\mathbf{x},t) = \frac{D_i}{k_{\mathrm{B}}T}\mathbf{F}(\mathbf{x},t), \tag{2.28}$$

where k_{B} is the Boltzmann constant.

Combining Equation 2.26, Equation 2.27, and Equation 2.28 yields

$$\mathbf{u}_i^{\mathrm{m}}(\mathbf{x},t) = -\frac{z_i e D_i}{k_{\mathrm{B}}T}\nabla\phi(\mathbf{x},t) = -\frac{z_i F D_i}{RT}\nabla\phi(\mathbf{x},t), \tag{2.29}$$

where $e/k_{\mathrm{B}} = F/R$.

Substituting Equation 2.29 into Equation 2.22 yield an expanded version of the Nernst-Planck equation containing the electric potential ϕ:

$$\frac{\partial c_i(\mathbf{x},t)}{\partial t} = -\nabla\cdot\left(D_i\left(\nabla c_i(\mathbf{x},t) - \frac{z_i F}{RT}c_i(\mathbf{x},t)\nabla\phi(\mathbf{x},t)\right)\right) + S_i(\mathbf{x},t). \tag{2.30}$$

2.4.3 Conductivity

The migrative molar flux $\mathbf{N}_i^{\mathrm{m}}$ also follows from Ohm's law through

$$\mathbf{N}_i^{\mathrm{m}}(\mathbf{x},t) = -\frac{\kappa(\mathbf{x},t)}{z_i F}\nabla\phi(\mathbf{x},t), \tag{2.31}$$

where κ is the conductivity of the electrolyte.

The conductivity κ itself depends on the ionic strength μ of the ions present in the electrolyte through the Nernst-Einstein relation:[12]

$$\kappa(\mathbf{x},t) = \sum_i \kappa_i; \tag{2.32}$$

$$\kappa_i(\mathbf{x},t) = \sum_i \frac{F^2 D_i z_i^2}{RT} c_i(\mathbf{x},t). \tag{2.33}$$

2.4.4 The Electric Double Layer

Due to the oxidation reaction releasing electrons at the anode, the anode is charged negatively. Due to this, positive ions present in the electrolyte are attracted to the anode due to the Coulomb force to balance out this negative charge (see Figure 2.2). This produces a screening layer of the negative charge of the anode by the positive ions, which is known as the electric double layer (EDL). The EDL therefore represents the space around the anode where more positive ions are present to maintain electroneutrality in the electrolyte. The distance from the anode in which the EDL has effectively screened the negative charge of the anode is known as the Debye length λ. The Debye length λ is given by[12,20]

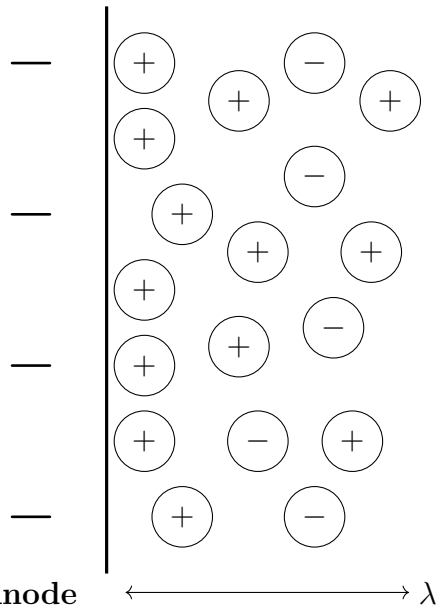


Figure 2.2: The electric double layer (EDL), forming a screening layer around the negatively charged anode. The screening effect of the EDL is present up until the Debye length λ. Not to scale.

$$\lambda = \sqrt{\frac{\epsilon RT}{2F^2\mu(\mathbf{x}_{\mathrm{a}}, t=0)}}, \tag{2.34}$$

where the ionic strength μ is given by

$$\mu(\mathbf{x},t) = \frac{1}{2}\sum_i z_i^2 c_i(\mathbf{x},t), \tag{2.35}$$

with the assumption that the ionic strength μ is taken at the anode under initial conditions.

Initially, the electrolyte only contains supporting ions at an initial concentration c_0 and no reactants. Equation 2.35 then gives us for the Debye length λ[21]

$$\mu(\mathbf{x},t) = \frac{1}{2}\sum_i (-1)^2 c_0 + (1)^2 c_0 = c_0 \Longrightarrow \lambda = \sqrt{\frac{\epsilon RT}{2F^2 c_0}}. \tag{2.36}$$

Through assuming electroneutrality[v], the electric potential ϕ at the anodic boundary Γ_{a} is given by Ohm's law:[12,18]

$$\nabla_{\mathrm{n}}\phi(\mathbf{x}_{\mathrm{a}},t) = -\frac{\mathbf{J}(\mathbf{x}_{\mathrm{a}},t)}{\kappa(\mathbf{x}_{\mathrm{a}},t)} \tag{2.37}$$

[v]This assumption omits the interaction of individual ions in the EDL — this is not accounted for in the modelling methods used in this thesis (see Subsection 3.1).[20]

2.5 System Constraints

The partial differential equations which the simulation will model are the Nernst-Planck equation (see Equation 2.22) and the Poisson equation (see Equation 2.23). These require both initial and boundary conditions to be solved.

2.5.1 Initial Conditions

Concentration

For the concentration c_i of a species i, it is assumed that at $t = 0$ all species which make up the electrolyte start uniformly at an initial concentration $c_{i,0}$, which are:

$$c_{\mathrm{K}^+}(\mathbf{x}, t = 0) = c_0, \quad (2.38) \qquad c_{\mathrm{OH}^-}(\mathbf{x}, t = 0) = c_0, \quad (2.39) \qquad c_{\mathrm{Zn(OH)_4}^{2}}(\mathbf{x}, t = 0) = 0. \quad (2.40)$$

Electric Potential

Note how these initial conditions yield $\rho(\mathbf{x}) = 0$ at $t = 0$ (see Equation 2.24), which is in accordance with the electroneutrality of the electrolyte. We therefore find

$$\phi(\mathbf{x}, t = 0) = 0. \tag{2.41}$$

2.5.2 Boundary Conditions

Concentration

At the anodic boundary Γ_a, the reactant species are introduced through the oxidation molar flux N_i^{ox} through the Nernst-Planck molar flux $\mathbf{N}_i$ (see Subsection 2.3):

$$\nabla_\mathrm{n} c_i(\mathbf{x}_\mathrm{a}, t) = -\frac{\mathbf{N}_i^{\mathrm{ox}}}{D_i} - \frac{z_i F}{RT} c_i(\mathbf{x}_\mathrm{a}, t) \nabla\phi(\mathbf{x}_\mathrm{a}, t). \tag{2.42}$$

At the carbon-black-alginate boundaries Γ_c, all species collide with the boundary and bounce back. The normal concentration gradient $\nabla_\mathrm{n} c_i$ is then simply given as:

$$\nabla_\mathrm{n} c_i(\mathbf{x}_\mathrm{c}, t) = \mathbf{0}. \tag{2.43}$$

At the bulk boundary Γ_b, we have the species i flowing into/leaving the system. This is given by the following Dirichlet boundary condition:

$$c_i(\mathbf{x}_\mathrm{b}, t) = c_{i,0}. \tag{2.44}$$

Electric Potential

At the anode Γ_a, the gradient normal to the anode is given through Ohm's law (see Equation 2.37. As the carbon-black-alginate boundaries Γ_c are non-reactive, their gradient normal to the surface is equal to zero. These are given by the following Neumann boundary conditions:[12,22]

$$\nabla_\mathrm{n}\phi(\mathbf{x}_\mathrm{a}, t) = -\frac{\mathbf{J}(\mathbf{x}_\mathrm{a}, t)}{\kappa(\mathbf{x}_\mathrm{a}, t)}. \quad (2.45) \qquad \nabla_\mathrm{n}\phi(\mathbf{x}_\mathrm{c}, t) = \mathbf{0}. \quad (2.46)$$

At the bulk boundary Γ_b it is assumed that the electrolyte is electrically neutral, therefore the electric potential is zero. We obtain the following Dirichlet boundary condition:

$$\phi(\mathbf{x}_\mathrm{b}, t) = 0; \tag{2.47}$$

2.6 The Poisson-Nernst-Planck Equations

The system we're interested in describes the evolution of each species i in the domain Ω. These are described by the Nernst-Planck equation (see Equation 2.30) and the Poisson equation (see Equation 2.25). The Poisson-Nernst-Planck (PNP) equations form a system of coupled non-linear partial differential equations.

Nernst-Planck Partial Differential Equation

$$\frac{\partial c_i(\mathbf{x},t)}{\partial t} = -\nabla \cdot \left(D_i \left(\nabla c_i(\mathbf{x},t) - \frac{z_i F}{RT} c_i(\mathbf{x},t) \nabla \phi(\mathbf{x},t) \right) \right) + S_i(\mathbf{x},t), \quad \mathbf{x} \in \Omega, t \geq 0;$$

$$c_i(\mathbf{x}, t=0) = c_{i,0}; \qquad c_i(\mathbf{x}_\mathrm{b}, t) = c_{i,0};$$

$$\nabla_\mathrm{n} c_i(\mathbf{x}_\mathrm{a}, t) = -\frac{\mathbf{N}_i^\mathrm{ox}}{D_i} - \frac{z_i F}{RT} c_i(\mathbf{x}_\mathrm{a}, t) \nabla \phi(\mathbf{x}_\mathrm{a}, t); \qquad \nabla_\mathrm{n} c_i(\mathbf{x}_\mathrm{c}, t) = \mathbf{0}.$$

Poisson Differential Equation

$$\nabla^2 \phi(\mathbf{x},t) = -\frac{F}{\epsilon} \sum_i z_i c_i(\mathbf{x},t), \quad \mathbf{x} \in \Omega, t \geq 0;$$

$$\phi(\mathbf{x}, t=0) = 0; \qquad \phi(\mathbf{x}_\mathrm{b}, t) = 0;$$

$$\nabla_\mathrm{n} \phi(\mathbf{x}_\mathrm{a}, t) = -\frac{\mathbf{J}(\mathbf{x}_\mathrm{a}, t)}{\kappa(\mathbf{x}_\mathrm{a}, t)}; \qquad \nabla_\mathrm{n} \phi(\mathbf{x}_\mathrm{c}, t) = \mathbf{0}.$$

Only when the system is 1D and in steady-state equilibrium ($\frac{\partial c_i}{\partial t} = 0$) does it have a known solution (see Section 5), otherwise no analytical solutions exist. To solve for this system, we apply discretization methods.

3 Discretization

3.1 Kinetic Theory 13
3.1.1 Mesoscopic Interactions 14
3.1.2 Boltzmann Kinetics 14
3.1.3 Pseudo-Kinetic Theory 15
3.2 The Lattice Boltzmann Method 17
3.2.1 Grid Discretization 17
3.2.2 Initialization 19
3.2.3 Computation 19
3.2.4 Relaxation 20
3.2.5 Propagation 20
3.2.6 Iteration 22
3.3 The Simulation Solvers 24
3.3.1 The Electrostatics Solver 24
3.3.2 The Electrokinetics Solver 24
3.3.3 The Migrative Velocity Solver 24
3.3.4 The Precipitation Kinetics Solver 25

In this section, the PNP equations are recast through the Lattice Boltzmann Method (LBM). To use this discretization method, we first need to apply kinetic theory to have the PNP equations work on the mesoscopic scale. Then, the LBM allows us to solve the PNP equations through iteration. This section mainly follows the methods laid out in "The Lattice Boltzmann Method: Principles and Practice" by T. Krüger.[23]

3.1 Kinetic Theory

The Nernst-Planck equation can be divided up in a transient, diffusive, migrative, and reactive term:

$$\underbrace{\frac{\partial c_i(\mathbf{x},t)}{\partial t}}_{\text{transient}} = -\underbrace{D_i\nabla^2 c_i(\mathbf{x},t)}_{\text{diffusive}} - \underbrace{\nabla\cdot(\mathbf{u}_i^{\text{m}}(\mathbf{x},t)c_i(\mathbf{x},t))}_{\text{migrative}} + \underbrace{S_i(\mathbf{x},t).}_{\text{reactive}} \tag{3.1}$$

The Nernst-Planck equation describes the evolution of the concentrations c_i present in the electrolyte over time t. From this equation, we want to obtain its *macroscopic* quantity: the concentration c_i and the migrative velocity $\mathbf{u}_i^{\text{m}}$. The processes involved, however, are *microscopic*, concerning the collisions and streaming of individual particles. To approximate the microscopic interactions we rely on kinetic theory, which states that if we operate on length and time scales sufficiently large, we can average out the particle interactions. The interactions between these averages now take place on a scale between the microscale and the macroscale, known as the *mesoscale*.[23]

3.1.1 Mesoscopic Interactions

Mesoscopically, we speak of distributions of particles, described through the particle distribution function f_i, also referred to as a particle population. We no longer assume that particles interact, but populations of particles do.[23]

Microscopically, the particles are assumed to have its own particle velocity $\boldsymbol{\xi}$. The concentration c_i at a position $\mathbf{x}$ and a time t is divided up into particle populations f_i based on the particle velocity $\boldsymbol{\xi}$: $f_i = f_i(\mathbf{x}, \boldsymbol{\xi}, t)$. It follows then that the macroscopic quantity concentration c_i can be obtained from the particle populations f_i by integrating them over velocity space:[23]

$$c_i(\mathbf{x}, t) = \int f_i(\mathbf{x}, \boldsymbol{\xi}, t)\, \mathrm{d}^3\boldsymbol{\xi}. \tag{3.2}$$

3.1.2 Boltzmann Kinetics

In the electrolyte, it is assumed the particles undergo elastic collisions. When the particle populations f_i collide, all individual particle velocities $\boldsymbol{\xi}$ tend to that of the velocity of the bulk, which is the migrative velocity $\mathbf{u}_i^{\mathrm{m}}$. After enough time t has passed, the particle populations f_i tend towards a particle equilibrium population f_i^{eq}.

The particle equilibrium population f_i^{eq} is described by the Maxwell-Boltzmann distribution, which is given by[23]

$$f_i^{\mathrm{eq}}(\mathbf{x}, |\boldsymbol{\xi}|, t) = c_i(\mathbf{x}, t) \left(\frac{1}{2\pi RT}\right)^{3/2} \exp\left(-\frac{\left|\boldsymbol{\xi} - \mathbf{u}_i^{\mathrm{m}}(\mathbf{x}, t)\right|^2}{2RT}\right), \tag{3.3}$$

which has the velocity distribution shifted by the migrative velocity $\mathbf{u}_i^{\mathrm{m}}$.

The evolution of populations towards equilibrium is described by a collision operator. The collision operator used in this thesis is the Bhatnagar–Gross–Krook (BGK) collision operator. This operator is a simple description of population collisions which remains physically accurate. For the particle populations f_i we find the respective BGK collision operators Ψ as[23]

$$\Psi(f_i) = -\frac{f_i - f_i^{\mathrm{eq}}}{\tau_i}; \tag{3.4}$$

where τ_i is the relaxation time, which depends on the diffusivity D of the species i.

Through taking the time derivative of the particle populations f_i we find the Boltzmann equations describing the evolution of the particle populations f_i:[23]

$$\frac{\partial f_i}{\partial t} + \boldsymbol{\xi}\nabla f_i + \frac{\mathrm{d}\boldsymbol{\xi}}{\mathrm{d}t}\frac{\partial f_i}{\partial \boldsymbol{\xi}} = \Psi(f_i); \tag{3.5}$$

3.1.3 Pseudo-Kinetic Theory

As the PNP equations are coupled, we need to solve for the Poisson equation to be able to solve for the Nernst-Planck equation (and vise versa). To solve the Poisson equation through discretization, we apply theory similar to that of the kinetic theory for particles, where instead of populations of particles interacting, we assume that only populations of potential interact.

As stated before in Subsection 2.4, the Poisson equation (see Equation 2.25) is quasi-static. This translates into the assumption that any (temporal) change in concentration c_i is immediately[vi] reflected in the electric potential ϕ. To model the electric potential ϕ through mesoscopic interactions, we will have to adapt the Poisson equation to become pseudo-transient whilst still being physically accurate.

To make the Poisson equation pseudo-transient, the following adaptation are necessary:

1. we need an analogous term for the diffusivity D to account for the "diffusive" transport of electric potential ϕ, which can deal with both precipitate and electrolyte;
2. we need to define a pseudo-time through which the "transient" evolution of the macroscopic quantity electric potential ϕ is solved;
3. when the pseudo-transient Poisson equation has reached pseudo-steady-state in pseudo-time, the original Poisson equation needs to be recovered.

Firstly, we will use the relative permittivity of the electrolyte ϵ_r to account for the "diffusive" transport of electric potential ϕ, which is obtained from splitting the permittivity ϵ into the relative permittivity ϵ_r and the vacuum permittivity ϵ_0: $\epsilon = \epsilon_\mathrm{r}\epsilon_0$. We find that[21]

$$\nabla^2\phi(\mathbf{x},t) = -\frac{\rho(\mathbf{x},t)}{\epsilon_\mathrm{r}\epsilon_0} \implies \epsilon_\mathrm{r}\nabla^2\phi(\mathbf{x},t) = -\frac{\rho(\mathbf{x},t)}{\epsilon_0} \tag{3.6}$$

Throughout modelling, we will encounter two materials through which the electric potential ϕ permeates: the electrolyte $\epsilon_{\mathrm{r,e}}$, and the zinc oxide precipitate $\epsilon_{\mathrm{r,p}}$. The relative permittivity ϵ_r therefore becomes dependent on the binary medium at a position $\mathbf{x}$, the time t, and the precipitate fraction p (see Equation 2.16):

$$\epsilon_\mathrm{r}(\mathbf{x},t) = (1-p(\mathbf{x},t))\epsilon_{\mathrm{r,e}} + p\epsilon_{\mathrm{r,p}}. \tag{3.7}$$

Now, we will also multiply the Poisson equation by the scaling constant γ, for which the need will be expanded on later (see Subsubsection 4.2.2). The product of the relative permittivity $\epsilon_\mathrm{r}(\mathbf{x},t)$ and the scaling constant γ gives us our pseudo-diffusivity χ. We find that[18,24]

$$\chi(\mathbf{x},t) = \gamma\epsilon_\mathrm{r}(\mathbf{x},t), \text{ with } \chi(\mathbf{x},0) = \gamma\epsilon_{\mathrm{r,e}} = \chi_0, \text{ so} \tag{3.8}$$

$$\gamma\epsilon_\mathrm{r}(\mathbf{x},t)\nabla^2\phi(\mathbf{x},t) = -\frac{\gamma\rho(\mathbf{x},t)}{\epsilon_0} \implies \chi(\mathbf{x},t)\nabla^2\phi(\mathbf{x},t) = -\frac{\gamma\rho(\mathbf{x},t)}{\epsilon_0}. \tag{3.9}$$

We then have Equation 3.9 equal a "transient" term through introducing the pseudo-time s:

$$\underbrace{\frac{\partial\phi(\mathbf{x},t,s)}{\partial s}}_{\text{"transient"}} = \underbrace{\chi(\mathbf{x},t)\nabla^2\phi(\mathbf{x},t,s)}_{\text{"diffusive"}} + \underbrace{\frac{\gamma\rho(\mathbf{x},t)}{\epsilon_0}}_{\text{"reactive"}}. \tag{3.10}$$

[vi] "Immediately", as the propagation speed of the electric potential ϕ is equal to the speed of light, which can be assumed to be instant on the time-scale which the particles operate on.

These adaptations to make the Poisson equation pseudo-transient yields the following partial differential equation to be solved.

Pseudo-Transient Poisson Differential Equation

$$\frac{\partial\phi(\mathbf{x},t,s)}{\partial s} = \chi(\mathbf{x},t)\nabla^2\phi(\mathbf{x},t,s) + \frac{\gamma F}{\epsilon_0}\sum_i z_i c_i(\mathbf{x},t), \quad \mathbf{x}\in\Omega, t\geq 0;$$

$$\phi(\mathbf{x},t=0,s) = 0; \qquad \phi(\mathbf{x}_\mathrm{b},t,s) = 0;$$

$$\nabla_\mathrm{n}\phi(\mathbf{x}_\mathrm{a},t,s) = -\frac{\mathbf{J}(\mathbf{x}_\mathrm{a},t)}{\chi(\mathbf{x},t)\kappa(\mathbf{x}_\mathrm{a},t)}; \qquad \nabla_\mathrm{n}\phi(\mathbf{x}_\mathrm{c},t,s) = \mathbf{0}.$$

Observe how when pseudo-steady-state is reached in pseudo-time ($\frac{\partial\phi(\mathbf{x},t,s)}{\partial s} = 0$), the scaling factor γ drops out of the equation, returning the original quasi-static Poisson equation. The pseudo-transient Poisson equation has transformed the Poisson equation into a continuity equation, where it now describes the transport of electric potential ϕ over pseudo-time s in the same vein as the transient Nernst-Planck equation describes the transport of concentration c_i over time t.

Out aim is now to solve the pseudo-transient Poisson equation (see Equation 3.10) in pseudo-time to obtain the electric potential ϕ at a time t. To do this, we will first have to obtain the concentrations c_i from the transient Nernst-Planck equation, and then compute the charge density ρ at a time t. Then, the passing of time t will be paused, and the pseudo-transient Poisson equation will be solved in pseudo-time s until pseudo-steady-state is reached.[21,24]

Pseudo-kinetic theory for the pseudo-transient Poisson equation then has us work with potential populations g, which divides up electric potential ϕ based on its potential pseudo-velocity $\boldsymbol{\zeta}$: $g = g(\mathbf{x},\boldsymbol{\zeta},t,s)$. We similarly find that the macroscopic quantity electric potential ϕ can be obtained by integrating the potential populations g over pseudo-velocity space:[23]

$$\phi(\mathbf{x},t,s) = \int g(\mathbf{x},\boldsymbol{\zeta},t,s)\,\mathrm{d}^3\boldsymbol{\zeta}. \tag{3.11}$$

The potential pseudo-velocities $\boldsymbol{\zeta}$ will tend towards the pseudo-velocity of the bulk, which is zero ($\mathbf{0}$) as there is no advective or migrative term in the pseudo-transient Poisson equation (see Equation 3.10). After enough pseudo-time s has elapsed, the potential populations g tends to the potential equilibrium population g^eq:

$$g^\mathrm{eq}(\mathbf{x},|\boldsymbol{\zeta}|,t,s) = \phi(\mathbf{x},t,s)\left(\frac{1}{2\pi RT}\right)^{3/2}\exp\left(-\frac{|\boldsymbol{\zeta}|^2}{2RT}\right). \tag{3.12}$$

The potential populations g has its BGK collision operators Φ given by[23]

$$\Phi(g) = -\frac{g-g^\mathrm{eq}}{\sigma}, \tag{3.13}$$

where σ is the relaxation pseudo-time, which depends on the pseudo-diffusivity χ.

Through taking the pseudo-time derivative of the potential populations g we find the Boltzmann equations describing the evolution of the potential populations g:[23]

$$\frac{\partial g}{\partial s} + \boldsymbol{\zeta}\nabla g + \frac{\mathrm{d}\boldsymbol{\zeta}}{\mathrm{d}s}\frac{\partial g}{\partial\boldsymbol{\zeta}} = \Phi(g). \tag{3.14}$$

3.2 The Lattice Boltzmann Method

The methodology laid out in Subsection 3.1, which results in the mesoscale physics described by the Boltzmann equations (see Equation 3.5 and Equation 3.14), is still impossible to solve analytically. We aim to implement the system of the PNP equations through the reasoning of (pseudo-)kinetic theory by using the LBM. The LBM utilizes a time-step algorithm to solve these equations for the concentrations c_i and the electric potential ϕ iteratively through the particle and potential populations f_i and g respectively. For each concentration c_i of a species i we'll have a transient Nernst-Planck $c_i(t)$-LBM model, and for the potential ϕ the pseudo-transient Poisson $\phi(s)$-LBM model. The $c_i(t)$-LBM and $\phi(s)$-LBM models will be developed in the remainder of this chapter.[18,21,23]

3.2.1 Grid Discretization

To apply the LBM, we first need to discretize the particle and potential populations f_i and g to only have a limited amount of velocity directions. This requires the discretization of position $\mathbf{x}$, time t, particle velocity $\boldsymbol{\xi}$ and potential pseudo-velocity $\boldsymbol{\zeta}$.[23]

Space Discretization

Three-dimensional space is discretized by being divided up in nodes which lie on an evenly spaced cubic grid or lattice separated by a lattice distance Δx. The nodes now account for the concentrations c_i and electric potential ϕ in the cubic volume (of size Δx^3) which surrounds the node (see Figure 3.1). The LBM models take place on domains Ω comprising of slices of these nodes in three-dimensional (3D) space, allowing us to also model one-dimensional (1D) and two-dimensional (2D) spaces.

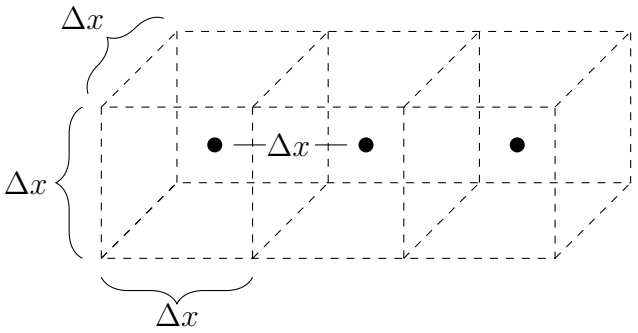


Figure 3.1: Nodes, spaced apart by a lattice spacing Δx, at the centre of their accounted for cubic volume.

For 1D, the domain Ω is defined as a rectangular line of lengths $L \times \Delta x \times \Delta x$, where the boundaries Γ lie at the ends of the line. For 2D, the domain Ω is defined as a square slab of length and height $L \times H \times \Delta x$, where the boundaries Γ lie on the edges of the slab. Movement in the 1D and 2D domains Ω is restricted to only be in 1D/2D by assuming the axes perpendicular to the domain Ω have periodic boundaries, effectively cancelling out movement in other axes. The domain Ω of length L (and height H if 2D) is divided up over the lattice length l (and lattice height h if 2D) in nodes. The particle and potential distributions f_i and g are taken over each of these cubes, and are defined on the nodes. These nodes are spaced apart evenly, separated by a lattice spacing Δx, given by[23]

$$\Delta x = \frac{L}{l} = \frac{H}{h}. \tag{3.15}$$

The boundaries Γ at the edges of the domain Ω are link-wise boundaries, implying that they midway on the lattice a distance of $\Delta x/2$ away from the nodes.

Time Discretization

Where the lattice spacing Δx represents a resolution of space, the time step Δt similarly represents the resolution of time. The LBM time-step algorithm progresses time forward in increments of Δt.[23]

Particle and Potential Velocity Discretization

The LBM dictates that populations now only move between neighbouring lattice nodes. The allowed distance a population can move in a time step Δt are towards neighbouring nodes (a distance of Δx), or remaining stationary. These velocity directions are given by the lattice vectors $\mathbf{e}_j$, where j indicates the lattice vector direction. These lattice vectors $\mathbf{e}_j$ form a velocity set DdQq, which denotes the dimension d and the number of lattice vector directions q. The velocity sets used in this thesis are D1Q3 and D2Q9 for 1D and 2D simulations respectively (see Figure 3.2).



(a) The D1Q3 velocity set. **(b)** The D2Q9 velocity set.

Figure 3.2: The D1Q3 and D2Q9 velocity sets and their lattice vectors $\mathbf{e}_j$.

The set of lattice vectors $(\mathbf{e}_j)$ for D1Q3 is given by (see Figure 3.2a)

$$(\mathbf{e}_j) = \begin{pmatrix} 0 & 1 & -1 \end{pmatrix} \frac{\Delta x}{\Delta t}; \tag{3.16}$$

and similarly for D2Q9 (see Figure 3.2b):

$$(\mathbf{e}_j) = \begin{pmatrix} 0 & 1 & 0 & -1 & 0 & 1 & -1 & -1 & 1 \\ 0 & 0 & 1 & 0 & -1 & 1 & 1 & -1 & -1 \end{pmatrix} \frac{\Delta x}{\Delta t}. \tag{3.17}$$

All populations now only move along the lattice vectors $\mathbf{e}_j$ in q directions. Similarly to Equation 3.2 and Equation 3.11, the macroscopic quantities concentration c_i and electric potential ϕ can be obtained from the discretized particle and potential populations $f_{i,j}$ and g_j by summing over discretized velocity space:[23]

$$c_i(\mathbf{x}, t) = \sum_{j=1}^{q} f_{i,j}(\mathbf{x}, t); \tag{3.18}$$

$$\phi(\mathbf{x}, t, s) = \sum_{j=1}^{q} g_j(\mathbf{x}, t, s). \tag{3.19}$$

The velocity sets D1Q3 and D2Q9 assigning each of the q lattice velocity directions a weight w_j. For the D1Q3 velocity set, we find[23]

$$w_j = \begin{cases} 2/3, & j = 1; \\ 1/6, & j = 2, 3; \end{cases} \tag{3.20}$$

and for the D2Q9 velocity set

$$w_j = \begin{cases} 4/9, & j = 1; \\ 1/9, & j = 2, 3, 4, 5; \\ 1/36, & j = 6, 7, 8, 9. \end{cases} \tag{3.21}$$

The weights w_i assigned to each of the lattice vectors $\mathbf{e}_j$ results in the LBM model to be conform with physical conservation laws.[23]

3.2.2 Initialization

To start the simulation, the particle and potential populations $f_{i,j}$ and g_j need to be initialized. To do this, we assume both the $c_i(t)$-LBM and the $\phi(s)$-LBM models to start in equilibrium. For the $c_i(t)$-LBM model, this is done by setting the concentration c_i to the initial concentration $c_{i,0}$ everywhere in the domain Ω, and obtain the particle (equilibrium) populations $f_{i,j}$ through the weights w_j:[23]

$$c_i(\mathbf{x}, t = 0) = c_{i,0}; \tag{3.22}$$

$$w_j c_i(\mathbf{x}, t = 0) = f_{i,j}(\mathbf{x}, t = 0). \tag{3.23}$$

For the $\phi(s)$-LBM model, the initial electric potential ϕ and potential populations g are initialized as being zero everywhere, as the electrolyte initially is electrically neutral.

After initialization, the LBM models iterate over its time-step algorithm in the now discretized domain Ω in discretized time steps Δt over discretized lattice vectors $\mathbf{e}_j$. This time-step algorithm allows (pseudo-)kinetic theory (see Subsection 3.1) to be expressed in a discretized form. The time-step algorithm consists of three main steps: the *computation* of the equilibrium population; the *relaxation* (or collision) of populations; and the *propagation* (or streaming) of populations.

3.2.3 Computation

The particle and potential equilibrium populations f_i^{eq} and g^{eq} seen in Equation 3.3 and Equation 3.12 respectively, have discretized counterparts.[vii]

For the $c_i(t)$-LBM model, the discretized particle equilibrium population f_i^{eq} is given by[23,21]

$$f_{i,j}^{\mathrm{eq}}(\mathbf{x}, t) = w_j c_i(\mathbf{x}, t) \left(1 + \frac{\mathbf{u}_i^{\mathrm{m}}(\mathbf{x}, t) \cdot \mathbf{e}_j}{v_{\mathrm{s}}^2} + \frac{(\mathbf{u}_i^{\mathrm{m}}(\mathbf{x}, t) \cdot \mathbf{e}_j)^2}{2v_{\mathrm{s}}^4} - \frac{\mathbf{u}_i^{\mathrm{m}}(\mathbf{x}, t) \cdot \mathbf{u}_i^{\mathrm{m}}(\mathbf{x}, t)}{2v_{\mathrm{s}}^2} \right), \tag{3.24}$$

where $v_{\mathrm{s}} = \frac{1}{\sqrt{3}} \frac{\Delta x}{\Delta t}$ is the lattice speed of sound.

To compute the discretized particle equilibrium population f_i^{eq} we first need to know the migrative velocity $\mathbf{u}_i^{\mathrm{m}}$ and the concentration c_i; these are obtained through Equation 2.29 and Equation 3.18 respectively.

For the $\phi(s)$-LBM model, the discretized potential equilibrium population g^{eq} is given simply[viii] by[21]

$$g_j^{\mathrm{eq}}(\mathbf{x}, t, s) = w_j \phi(\mathbf{x}, t, s). \tag{3.25}$$

Only the electric potential ϕ is required to compute the discretized potential equilibrium population g^{eq}, which is obtained through Equation 3.19.

[vii] Obtained through Hermite expansion[23] — this is omitted here.

[viii] Note how the discretized potential equilibrium population g^{eq} has no terms containing the pseudo-velocity $\boldsymbol{\zeta}$ as explained in Subsubsection 3.1.2.

3.2.4 Relaxation

On each node, the particle and potential distributions f_i and g collide locally and have their source/sink terms add/remove particles/potential from the nodes.

The local collisions have the particle and potential populations f_i and g approach their respective equilibrium populations f_i^{eq} and g^{eq} through their respective BGK collision operators Ψ and Φ (see Equation 3.4 and Equation 3.13).

For the $c_i(t)$-LBM, the concentration source/sink term S_i is distributed over the particle populations f_i in all q lattice directions through their respective weights w_j. The concentration source/sink term S_i then adds/removes concentration over a time step Δt, yielding the discretized source/sink term as $\Delta t w_j S_i$.[23]

For the $\phi(s)$-LBM, the right-hand side of the pseudo-transient Poisson equation (see Equation 3.10) is seen as a "source/sink"-term. The discretized pseudo-source/sink term is then similarly given as $\Delta s w_j \gamma \rho / \epsilon_0$.

The collision operators Ψ and the discretized source/sink term acts over a time step Δt — the collision operator Φ and the discretized pseudo-source/sink term acts over a pseudo-time step Δs. The particle and potential populations after collisions f_i^{col} and g^{col} are thus given by the lattice BGK equations as:[23,21,24]

$$\begin{aligned} f_{i,j}^{\text{col}}(\mathbf{x},t) &= f_{i,j}(\mathbf{x},t) + \Delta t\left(\Psi(f_{i,j}) + w_j S_i(\mathbf{x},t)\right) \\ &= f_{i,j}(\mathbf{x},t) + \Delta t\left(-\frac{f_{i,j}(\mathbf{x},t) - f_{i,j}^{\text{eq}}(\mathbf{x},t)}{\tau_i} + w_j S_i(\mathbf{x},t)\right); \end{aligned} \tag{3.26}$$

$$\begin{aligned} g_j^{\text{col}}(\mathbf{x},t,s) &= g_j(\mathbf{x},t,s) + \Delta s\left(\Phi(g_j) + w_j\frac{\gamma\rho(\mathbf{x},t)}{\epsilon_0}\right) \\ &= g_j(\mathbf{x},t,s) + \Delta s\left(-\frac{g_j(\mathbf{x},t,s) - g_j^{\text{eq}}(\mathbf{x},t,s)}{\sigma} + w_j\frac{\gamma\rho(\mathbf{x},t)}{\epsilon_0}\right). \end{aligned} \tag{3.27}$$

The relaxation time τ_i and relaxation pseudo-time σ are given by[23]

$$\tau_i = \frac{\Delta t}{2} + \frac{D_i}{v_{\text{s}}^2}; \tag{3.28}$$

$$\sigma = \frac{\Delta s}{2} + \frac{\chi(\mathbf{x},t)}{v_{\text{l}}^2}, \tag{3.29}$$

where $v_{\text{l}} = \frac{1}{\sqrt{3}}\frac{\Delta x}{\Delta s}$ is analogous to the lattice speed of light.

3.2.5 Propagation

By discretizing the Boltzmann equations (see Equation 3.5 and Equation 3.14) we find the lattice Boltzmann equations through which we can obtain the particle and population distributions for the next (pseudo-)time-step f_i^{next} and g_j^{next}:

$$f_{i,j}^{\text{next}}(\mathbf{x}+\mathbf{e}_j, t+\Delta t) = f_{i,j}^{\text{col}}(\mathbf{x},t); \tag{3.30}$$

$$g_j^{\text{next}}(\mathbf{x}+\mathbf{e}_j, t, s+\Delta s) = g_j^{\text{col}}(\mathbf{x},t,s). \tag{3.31}$$

The particle and potential populations after collisions f_i^{col} and g^{col} now have moved over to neighbouring nodes according to their lattice vectors $\mathbf{e}_j$. Note how on the boundaries $\delta\Omega$, we can not solve Equation 3.30 and Equation 3.31 for all directions j as $\mathbf{x}+\mathbf{e}_j$ refers to a node outside of the domain Ω. It is here where the boundary conditions (see Subsubsection 2.5.2) are imposed to fill in these missing particle and potential populations $f_{i,j}^{\text{next}}$ and g_j^{next}.

Halfway Bounce-Back (Neumann) Boundary Conditions

For the Neumann carbon-black-alginate boundaries Γ_c, we use the bounce-back approach to fill in the missing particle and potential populations $f_{i,j}$ and g_j. This approach has the populations which hit the solid boundary be reflected back to their original node, now moving in the opposite direction:[23]

$$f_{i,j}^{\text{next}}(\mathbf{x}_c, t+\Delta t) = f_{i,j'}^{\text{col}}(\mathbf{x}_c, t); \qquad (3.32) \qquad g_j^{\text{next}}(\mathbf{x}_c, t, s+\Delta s) = g_{j'}^{\text{col}}(\mathbf{x}_c, t, s), \qquad (3.33)$$

where j' denotes the lattice direction opposite to j.

This bounce-back approach is also used whenever a neighbouring lattice node has a precipitate fraction $p > 0$. Equation 3.30 is then expanded to incorporate the precipitate present in nearby lattice nodes:[ix18]

$$f_{i,j}^{\text{next}}(\mathbf{x}+\mathbf{e}_j, t+\Delta t) = (1-p(\mathbf{x}+\mathbf{e}_j, t))f_{i,j}^{\text{col}}(\mathbf{x}, t) + p(\mathbf{x}, t)f_{i,j'}^{\text{col}}(\mathbf{x}+\mathbf{e}_j, t) \qquad (3.34)$$

In the case of the Neumann anodic boundary Γ_a, the appropriate flux term is added/subtracted to the bounced-back population. In 2D, as the oxidation molar flux N_{ox} and the current density J are taken to be normal to the surface, they are divided up among the three lattice vectors $\mathbf{e}_j$ who have a component normal to the surface. This amount is normalized over the weights of these vectors (see Equation 3.21), where two-thirds is distributed along the lattice vector $\mathbf{e}_j$ perpendicular to the anode, and one-sixth to the lattice vectors $\mathbf{e}_j$ diagonal to the anode (see Figure 3.3). The equation for the bounce-back approach for the missing particle and potential populations $f_{i,j}^{\text{next}}$ and g_j^{next} are then given by[18,25,26]

$$f_{i,j}^{\text{next}}(\mathbf{x}_a, t+\Delta t) = f_{i,j'}^{\text{col}}(\mathbf{x}_a, t) + 6w_j N_{ox}(\mathbf{x}_a, t)\frac{\Delta t}{\Delta x}; \qquad (3.35)$$

$$g_j^{\text{next}}(\mathbf{x}_a, t, s+\Delta s) = g_{j'}^{\text{col}}(\mathbf{x}_a, t, s) + 6w_j \frac{J(\mathbf{x}_a, t)}{\kappa(\mathbf{x}_a, t)}\frac{\Delta s}{\Delta x}. \qquad (3.36)$$

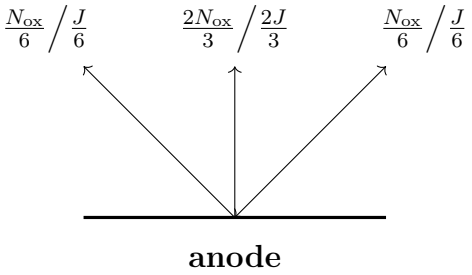


Figure 3.3: The division of the oxidation molar flux N_{ox} and the current density J, based on the weights w_j of the lattice vectors $\mathbf{e}_j$.

[ix] A method similar to what was used for the permittivity ϵ through a binary medium (see Equation 3.7) could be applied here too.[14]

Halfway Anti-Bounce-Back (Dirichlet) Boundary Conditions

For the Dirichlet bulk boundaries Γ_b, we use a similar approach known as the anti-bounce-back approach. In the anti-bounce-back approach, the difference between the population after collision and the equilibrium population which leave the system is "anti-bounced-back" to the missing population. These "anti-bounced-back" non-equilibrium populations are given as[23,25,27]

$$f_{i,j}^{\mathrm{next}}(\mathbf{x}_\mathrm{b}, t+\Delta t) - f_{i,j}^{\mathrm{eq}}(\mathbf{x}_\mathrm{b}, t) = -(f_{i,j'}^{\mathrm{col}}(\mathbf{x}_\mathrm{b}, t) - f_{i,j'}^{\mathrm{eq}}(\mathbf{x}_\mathrm{b}, t)); \tag{3.37}$$

$$g_{j}^{\mathrm{next}}(\mathbf{x}_\mathrm{b}, t, s+\Delta s) - g_{j}^{\mathrm{eq}}(\mathbf{x}_\mathrm{b}, t, s) = -(g_{j'}^{\mathrm{col}}(\mathbf{x}_\mathrm{b}, t, s) - g_{j'}^{\mathrm{eq}}(\mathbf{x}, t, s)). \tag{3.38}$$

At a boundary Γ, the concentration c_i and electric potential ϕ are imposed at some constant value c_0 and ϕ_0 respectively. As the equilibrium populations in opposite directions on the same node have their velocities cancel out (see Equation 3.24), they reduce the previous equations down to[23,25,27]

$$f_{i,j}^{\mathrm{next}}(\mathbf{x}_\mathrm{b}, t+\Delta t) = -f_{i,j'}^{\mathrm{col}}(\mathbf{x}_\mathrm{b}, t) + 2w_j c_0; \tag{3.39}$$

$$g_{j}^{\mathrm{next}}(\mathbf{x}_\mathrm{b}, t, s+\Delta s) = -g_{j'}^{\mathrm{col}}(\mathbf{x}_\mathrm{b}, t, s) + 2w_j \phi_0. \tag{3.40}$$

3.2.6 Iteration

Through the methods laid out so far, we can advance through the Nernst-Planck and Poisson equations both spatially and (pseudo-)temporally, by iterating over the computation, relaxation, and propagation steps. The stepping ahead through time t in steps of Δt meaningfully tells us about the evolution of concentrations c_i through solving the transient Nernst-Planck equation until a desired simulation time t_sim has been reached. However, we only require the results of the pseudo-transient Poisson equation when it has reached pseudo-steady-state for it to equal the actual Poisson equation. To know whenever the $\phi(s)$-LBM model has reached pseudo-steady-state, we check its convergence ε through:[21]

$$\varepsilon = \sqrt{\frac{1}{l}\sum_{\mathbf{x}} \left(\frac{\phi(\mathbf{x}, t, s) - \phi(\mathbf{x}, t, s-\Delta s)}{\phi(\mathbf{x}, t, s-\Delta s)} \right)^2} \tag{3.41}$$

A threshold δ is imposed on the convergence ε as a minimum value between the electric potential ϕ taken a pseudo-time step Δs apart to determine that the pseudo-transient Poisson equation has reached steady-state.

Combining what has been derived in Subsection 3.2, we have the following for the $c_i(t)$-LBM and $\phi(s)$-LBM models.

LBM Model Initialization

Concentration Initial Condition
$$c_i(\mathbf{x}, 0) = c_{i,0}$$

Electric Potential Initial Condition
$$\phi(\mathbf{x}, 0) = 0$$

Particle Population Initial Condition
$$w_j c_i(\mathbf{x}, 0) = f_{i,j}(\mathbf{x}, 0)$$

Potential Population Initial Condition
$$w_j \phi(\mathbf{x}, 0) = g_j(\mathbf{x}, 0, s)$$

The $c_i(t)$-LBM Model

Equilibrium Computation

$$f_{i,j}^{\mathrm{eq}}(\mathbf{x},t) = w_j c_i(\mathbf{x},t)\left(1 + \frac{\mathbf{u}_i^{\mathrm{m}}(\mathbf{x},t)\cdot\mathbf{e}_j}{v_{\mathrm{s}}^2} + \frac{(\mathbf{u}_i^{\mathrm{m}}(\mathbf{x},t)\cdot\mathbf{e}_j)^2}{2v_{\mathrm{s}}^4} - \frac{\mathbf{u}_i^{\mathrm{m}}(\mathbf{x},t)\cdot\mathbf{u}_i^{\mathrm{m}}(\mathbf{x},t)}{2v_{\mathrm{s}}^2}\right)$$

Relaxation

$$f_{i,j}^{\mathrm{col}}(\mathbf{x},t) = f_{i,j}(\mathbf{x},t) + \Delta t\left(-\frac{f_{i,j}(\mathbf{x},t) - f_{i,j}^{\mathrm{eq}}(\mathbf{x},t)}{\tau_i} + w_j S_i(\mathbf{x},t)\right)$$

Propagation

$$f_{i,j}^{\mathrm{next}}(\mathbf{x}+\mathbf{e}_j, t+\Delta t) = (1 - p(\mathbf{x}+\mathbf{e}_j,t)) f_{i,j}^{\mathrm{col}}(\mathbf{x},t) + p(\mathbf{x},t) f_{i,j'}^{\mathrm{col}}(\mathbf{x}+\mathbf{e}_j,t)$$

Anodic Boundary Condition

$$f_{i,j}^{\mathrm{next}}(\mathbf{x}_{\mathrm{a}}, t+\Delta t) = f_{i,j'}^{\mathrm{col}}(\mathbf{x}_{\mathrm{a}},t) + 6 w_j N_{\mathrm{ox}}(\mathbf{x}_{\mathrm{a}},t)\frac{\Delta t}{\Delta x}$$

Carbon-black-alginate Boundary Condition

$$f_{i,j}^{\mathrm{next}}(\mathbf{x}_{\mathrm{c}}, t+\Delta t) = f_{i,j'}^{\mathrm{col}}(\mathbf{x}_{\mathrm{c}},t)$$

Bulk Boundary Condition

$$f_{i,j}^{\mathrm{next}}(\mathbf{x}_{\mathrm{b}}, t+\Delta t) = -f_{i,j'}^{\mathrm{col}}(\mathbf{x}_{\mathrm{b}},t) + 2 w_j c_{i,0}$$

The $\phi(s)$-LBM Model

Equilibrium Computation

$$g_j^{\mathrm{eq}}(\mathbf{x},t,s) = w_j \phi(\mathbf{x},t,s)$$

Relaxation

$$g_j^{\mathrm{col}}(\mathbf{x},t,s) = g_j(\mathbf{x},t,s) + \Delta s\left(-\frac{g_j(\mathbf{x},t,s) - g_j^{\mathrm{eq}}(\mathbf{x},t,s)}{\sigma} + w_j\frac{\gamma\rho(\mathbf{x},t)}{\epsilon_0}\right)$$

Propagation

$$g_j^{\mathrm{next}}(\mathbf{x}+\mathbf{e}_j, t, s+\Delta s) = g_j^{\mathrm{col}}(\mathbf{x},t,s)$$

Anodic Boundary Condition

$$g_j^{\mathrm{next}}(\mathbf{x}_{\mathrm{a}}, t, s+\Delta s) = g_{j'}^{\mathrm{col}}(\mathbf{x}_{\mathrm{a}},t,s) + 6 w_j \frac{J(\mathbf{x}_{\mathrm{a}},t)}{\kappa(\mathbf{x}_{\mathrm{a}},t)}\frac{\Delta s}{\Delta x}$$

Carbon-black-alginate Boundary Condition

$$g_j^{\mathrm{next}}(\mathbf{x}_{\mathrm{c}}, t, s+\Delta s) = g_{j'}^{\mathrm{col}}(\mathbf{x}_{\mathrm{c}},t,s)$$

Bulk Boundary Condition

$$g_j^{\mathrm{next}}(\mathbf{x}_{\mathrm{b}}, t, s+\Delta s) = -g_{j'}^{\mathrm{col}}(\mathbf{x}_{\mathrm{b}},t,s)$$

3.3 The Simulation Solvers

The $c_i(t)$-LBM and $\phi(s)$-LBM models require some other macroscopic quantities as inputs to run. These are calculated in separate solvers before the models are ran.

3.3.1 The Electrostatics Solver

The Electrostatics Solver compoutes the macroscopic properties at a time t which are required to solve for the electric potential ϕ.

The Electrostatics Solver

Reaction Quotient
$$Q(\mathbf{x}_\mathrm{a}, t) = \frac{c_{\mathrm{Zn(OH)_4}^{2-}}(\mathbf{x}_\mathrm{a}, t)}{c^4_{\mathrm{OH}^-}(\mathbf{x}_\mathrm{a}, t)} \cdot 10^9\,\mathrm{mol}^3/\mathrm{m}^9$$

Nernst Equation
$$E_\mathrm{ox}(\mathbf{x}_\mathrm{a}, t) = E^\circ_\mathrm{ox} + \frac{RT}{nF}\ln Q(\mathbf{x}_\mathrm{a}, t)$$

Charge Density
$$\rho(\mathbf{x}, t) = F\sum_i z_i c_i(\mathbf{x}, t)$$

Conductivity
$$\kappa_i(\mathbf{x}, t) = \sum_i \frac{F^2 D_i z_i^2}{RT} c_i(\mathbf{x}, t)$$

Pseudo-Diffusivity
$$\chi(\mathbf{x}, t) = \gamma\Big((1-p)\epsilon_\mathrm{r,e} + p\epsilon_\mathrm{r,p}\Big)$$

Relaxation Pseudo-Time
$$\sigma = \frac{\Delta s}{2} + \frac{\chi(\mathbf{x}, t)}{v_\mathrm{l}^2}$$

3.3.2 The Electrokinetics Solver

The Electrokinetics Solver computes the macroscopic properties at a time t which are required to solve for the electric potential ϕ and for the oxidation reaction.

The Electrokinetics Solver

Overpotential
$$\eta(\mathbf{x}_\mathrm{a}, t) = \phi_\mathrm{s} - \phi(\mathbf{x}_\mathrm{a}, t) - E_\mathrm{ox}(\mathbf{x}_\mathrm{a}, t)$$

Tafel Equation
$$J(\mathbf{x}_\mathrm{a}, t) = J_0 \exp\left(\frac{\alpha_\mathrm{a} F}{RT}\eta(\mathbf{x}_\mathrm{a}, t)\right)$$

Faraday's Law
$$N_\mathrm{ox}(\mathbf{x}_\mathrm{a}, t) = J(\mathbf{x}_\mathrm{a}, t)\frac{\nu}{nF}$$

3.3.3 The Migrative Velocity Solver

The migrative velocity $\mathbf{u}_i^\mathrm{m}$ is obtained through the spatial derivative of the electric potential $\nabla\phi$ (see Equation 2.29). This derivative is solved through the finite difference method (FDM). We can split up the electric potential ϕ in its x-component and its y-component:[x]

$$\nabla\phi(\mathbf{x}, t) = \left(\frac{\partial\phi(\mathbf{x}, t)}{\partial x}\hat{\mathbf{x}} + \frac{\partial\phi(\mathbf{x}, t)}{\partial y}\hat{\mathbf{y}}\right). \tag{3.42}$$

[x]For 1D simulations we only use its x-component.

We then apply the FDM central difference scheme in the x-direction and the y-direction for $\mathbf{x} \in \Omega$, and FDM forward and backward difference schemes at the boundaries $\mathbf{x} \in \delta\Omega$.

The Migrative Velocity Solver

Central FDM, $\hat{x}$-direction
$$\frac{\partial\phi(x,y,t)}{\partial x} \approx \frac{\phi(x+\Delta x,y,t)-\phi(x-\Delta x,y,t)}{2\Delta x}$$

Central FDM, $\hat{y}$-direction
$$\frac{\partial\phi(x,y,t)}{\partial y} \approx \frac{\phi(x,y+\Delta x,t)-\phi(x,y-\Delta x,t)}{2\Delta x}$$

Forward FDM, $+\hat{x}$-direction
$$\frac{\partial\phi(x,y,t)}{\partial x} \approx \frac{-3\phi(x,y,t)+4\phi(x+\Delta x,y,t)-\phi(x+2\Delta x,y,t)}{2\Delta x}$$

Forward FDM, $+\hat{y}$-direction
$$\frac{\partial\phi(x,y,t)}{\partial x} \approx \frac{-3\phi(x,y,t)+4\phi(x,y+\Delta x,t)-\phi(x,y+2\Delta x,t)}{2\Delta x}$$

Backward FDM, $-\hat{x}$-direction
$$\frac{\partial\phi(x,y,t)}{\partial x} \approx \frac{-3\phi(x,y,t)+4\phi(x+\Delta x,y,t)-\phi(x+2\Delta x,y,t)}{2\Delta x}$$

Backward FDM, $-\hat{y}$-direction
$$\frac{\partial\phi(x,y,t)}{\partial x} \approx \frac{3\phi(x,y,t)-4\phi(x,y-\Delta x,t)+\phi(x,y-2\Delta x,t)}{2\Delta x}$$

3.3.4 The Precipitation Kinetics Solver

After the $c_i(t)$-LBM model has calculated the new concentrations c_i at a time $t+\Delta t$, we will calculate how much of the formed zincate precipitates into zinc oxide. This is done by first calculating the source/sink term S_i (see Equation 2.14). Then, the change in the precipitate fraction p is calculated through a discretized version of Equation 2.16.[18]

The Precipitation Kinetics Solver

For a position $\mathbf{x}$ with one of the following properties:

- $\mathbf{x} \in \Gamma_a \cup \Gamma_c$;
- has a neighbouring node $\mathbf{x} \pm \Delta\mathbf{x}$ where $p(\mathbf{x} \pm \Delta\mathbf{x}, t) \geq p_{\min}$,

Source/Sink Term Calculation
$$\begin{cases} S_i(\mathbf{x},t) = \nu_i k(c_{\mathrm{Zn(OH)_4{}^{2-}}}(\mathbf{x},t) - K), & c_{\mathrm{Zn(OH)_4{}^{2-}}} > K; \\ S_i(\mathbf{x},t) = 0, & c_{\mathrm{Zn(OH)_4{}^{2-}}} \leq K \end{cases}$$

If $(1 - p(\mathbf{x},t))/M_{\mathrm{ZnO}} > S_i(\mathbf{x},t)$ (meaning $p(\mathbf{x},t)$ will overshoot the available volume):

$$S_i(\mathbf{x},t) = (1 - p(\mathbf{x},t))/M_{\mathrm{ZnO}}$$

Updated Precipitate Fraction
$$p(\mathbf{x},t) = p(\mathbf{x},t-\Delta t) + S_i(\mathbf{x},t)M_{\mathrm{ZnO}}$$

The methods laid out in this chapter fully explain how to solve for the PNP equations. Before giving a full overview of both the $c_i(t)$-LBM and $\phi(s)$-LBM models, we will first simplify all relevant equation through non-dimensionalization, a process which has the physical units be linked to their characteristic scales.[23]

4 Non-Dimensionalization

4.1 Unit Conversion Factors 26
4.2 Non-Dimensional Numbers and Restrictions 28
4.2.1 Propagation Limits 28
4.2.2 Relaxation Time Limits 28
4.2.3 Resolution Limits 29
4.3 Non-Dimensional Equations 29

In working with the LBM, it is common to work in lattice units. This is done to have the simulation work with values which are expressed through their characteristic value, allowing us to use values close to unity, reducing floating-point errors and improving interpretability. The magnitude of these lattice units are obtained through unit conversion factors.[23]

4.1 Unit Conversion Factors

All variables in this thesis can be described with six independent units: the meter (m), second (s), mole (mol), volt (V), coulomb (C) and kelvin (K). We therefore need exactly six unit conversion factors $\mathcal{S}$, $\mathcal{T}$, $\mathcal{M}$, $\mathcal{P}$, $\mathcal{C}$, and $\mathcal{D}$ (which stand for the space, time, mole, potential, charge, and degrees of temperature conversion factor, respectively) to convert back and forth between physical units and lattice units.[xi] The six unit conversion factors are chosen based on characteristic/reference values to also improve the interpretability of those variables.[23]

Space and Time

As populations only move between lattice nodes in singular lattice spacings Δx and time steps Δt, they will be set to unity in lattice units. This introduces the lattice units ls (lattice space) and lt (lattice time): $\Delta\tilde{x} = 1\,\mathrm{ls}$ and $\Delta\tilde{t} = 1\,\mathrm{lt}$, therefore $1\ [\mathrm{ls}] \triangleq \Delta x\ [\mathrm{m}]$ and $1\ [\mathrm{lt}] \triangleq \Delta t\ [\mathrm{s}]$. It follows then that the space conversion factor $\mathcal{S}$ and time conversion factor $\mathcal{T}$ are given by the discretized lattice spacing and time step (in physical units):

$$\mathcal{S} = \frac{x}{\tilde{x}} = \frac{\Delta x}{\Delta\tilde{x}} = \frac{\Delta x\ [\mathrm{m}]}{1\ [\mathrm{ls}]} = \Delta x\ \ [\mathrm{m}/\mathrm{ls}]\,, \qquad (4.1)$$

$$\mathcal{T} = \frac{t}{\tilde{t}} = \frac{\Delta t}{\Delta\tilde{t}} = \frac{\Delta t\ [\mathrm{s}]}{1\ [\mathrm{lt}]} = \Delta t\ \ [\mathrm{s}/\mathrm{lt}]\,. \qquad (4.2)$$

Concentration

As were working with an initial concentration c_0, it is convenient to use it as a reference through normalizing the concentration c_i by this initial concentration c_0. This is done through the lattice unit lm (lattice mole) which is defined through having the initial concentration in lattice units be equal to unity: $\tilde{c}_0 = 1\,\mathrm{lm\,ls^{-3}}$. Multiplying by the lattice volume Δx^3 then gets us $1\ [\mathrm{lm}] \triangleq c_0\Delta x^3\ [\mathrm{mol}]$. For the mole conversion factor $\mathcal{M}$ we thus find

$$\mathcal{M} = \frac{c_i\Delta x^3}{\tilde{c}_i\Delta\tilde{x}^3} = \frac{c_0\Delta x^3}{\tilde{c}_0\Delta\tilde{x}^3} = \frac{c_0\Delta x^3\ [\mathrm{mol}]}{1\ [\mathrm{lm}]} = c_0\Delta x^3\ \ [\mathrm{mol}/\mathrm{lm}]\,. \qquad (4.3)$$

[xi] Note how everything converted to lattice units is dimensionless, i.e. without a unit. For clarity, we will still use lattice units to express and describe their physical unit counterparts.

Potential

For the electric potential ϕ we take the thermal potential ϕ_{T} as a reference[xii], given by[12]

$$\phi_{\mathrm{T}} = \frac{k_{\mathrm{B}}T}{e} = \frac{RT}{F}. \tag{4.4}$$

We set the thermal potential ϕ_{T} to be equal to unity in lattice units. Introducing the lattice unit lp (lattice potential) through $\tilde{\phi}_{\mathrm{T}} = 1\,\mathrm{lp}$, we have 1 [lp] $\triangleq RT/F$ [V]. We find for the potential conversion factor $\mathcal{P}$ that

$$\mathcal{P} = \frac{\phi}{\tilde{\phi}} = \frac{\phi_{\mathrm{T}}}{\tilde{\phi}_{\mathrm{T}}} = \frac{RT/F\ [\mathrm{V}]}{1\ [\mathrm{lp}]} = \frac{RT}{F}\,[\mathrm{V/lp}]\,, \tag{4.5}$$

Charge

Although we do not work with a variable which is only expressed in coulombs, we do relate charges to moles in Faraday's law (see Equation 2.5) using Faraday's constant F [$\mathrm{C\,mol^{-1}}$]. Through Faraday's constant F and the previous definition of the lattice concentration, we introduce the lattice unit lc (lattice charge) as 1 [lc] $\triangleq Fc_0\Delta x^3$ [C], and find for the charge conversion factor $\mathcal{C}$ that

$$\mathcal{C} = \frac{Fc_0\Delta x^3\ [\mathrm{C}]}{1\ [\mathrm{lc}]} = Fc_0\Delta x^3\ \ [\mathrm{C/lc}]\,. \tag{4.6}$$

Temperature

Even if we find no need to express the temperature T in lattice units, as it is already incorporated in the thermal potential ϕ_{T} (see Equation 4.4), we will still do so for the sake of completeness. Introducing the lattice unit ld (lattice degree) simply as 1 [ld] $\triangleq$ 1 [K], we find for the degree of temperature conversion factor $\mathcal{D}$ that

$$\mathcal{D} = \frac{T\ [\mathrm{K}]}{\tilde{T}\ [\mathrm{ld}]} = 1\,[\mathrm{K/ld}]\,. \tag{4.7}$$

For any variable, we can find its variable conversion factor $\mathcal{V}$ through applying the unit conversion factors $\mathcal{S}$, $\mathcal{T}$, $\mathcal{M}$, $\mathcal{P}$, $\mathcal{C}$, and $\mathcal{D}$ through[28]

$$\mathcal{V} = \mathcal{S}^{a_{\mathrm{m}}}\mathcal{T}^{a_{\mathrm{s}}}\mathcal{M}^{a_{\mathrm{mol}}}\mathcal{P}^{a_{\mathrm{V}}}\mathcal{C}^{a_{\mathrm{C}}}\mathcal{D}^{a_{\mathrm{K}}}, \tag{4.8}$$

where the unit exponents a represent the order of the physical units present in the variable.

Through Equation 4.8, any variable expressed in lattice units is then able to be converted back to physical units when multiplied by its variable conversion factor $\mathcal{V}$.

[xii] The thermal potential ϕ_{T} relates temperature to electron potential, and is used as a standard reference potential in literature.[12]

4.2 Non-Dimensional Numbers and Restrictions

Through converting variables with the variable conversion factors $\mathcal{V}$, we observe how the variable in lattice units represent non-dimensional numbers. These non-dimensional numbers impose limits on the LBM models.[28]

4.2.1 Propagation Limits

As all movement through the LBM is restricted to discretized steps of Δx and Δt, no movement can allow populations to move further than one lattice space Δx in one lattice time Δt. We find that the non-dimensional diffusivity $\tilde{D}$ and the non-dimensional migrative velocity $\tilde{\mathbf{u}}_i^{\mathrm{m}}$ equal two dimensionless numbers which act over one lattice node, namely the grid[xiii] Fourier number Fo_Δ and the grid Courant number Co_Δ:[28,29]

$$\tilde{D}_i = \frac{D_i}{\mathcal{V}_D} = \frac{D_i \mathcal{T}}{\mathcal{S}^2} = \frac{D_i \Delta t}{\Delta x^2} = \mathrm{Fo}_\Delta. \qquad (4.9) \qquad \tilde{\mathbf{u}}_i^{\mathrm{m}} = \frac{\mathbf{u}_i^{\mathrm{m}}}{\mathcal{V}_u} = \frac{\mathbf{u}_i^{\mathrm{m}} \mathcal{T}}{\mathcal{S}} = \frac{\mathbf{u}_i^{\mathrm{m}} \Delta t}{\Delta x} = \mathrm{Co}_\Delta. \qquad (4.10)$$

Equation 4.9 and Equation 4.10 combine in the grid Péclet number Pe_Δ:[28,21,30]

$$\mathrm{Pe}_\Delta = \frac{\mathrm{Co}_\Delta}{\mathrm{Fo}_\Delta} = \frac{\mathbf{u}_i^{\mathrm{m}} \Delta x}{D_i}. \qquad (4.11)$$

To have the simulation run stable and physically accurate, the grid Péclet number can not be more than 2, as this implies a migrative velocity $\mathbf{u}_i^{\mathrm{m}}$ overtaking the effects of the diffusivity D_i. This allows particle populations f_i to move more than one lattice space Δx in one lattice time Δt, resulting in negative particle populations f_i.[30]

4.2.2 Relaxation Time Limits

The relaxation time τ_i and the relaxation pseudo-time σ dictates the diffusivity D and pseudo-diffusivity χ of the LBM models respectively. The relaxation time τ_i is dependent on the lattice space Δx and the lattice time Δt; the relaxation pseudo-time σ is dependent on the lattice space Δx and the scaling constant γ[xiv]. The following regions are defined for the effects of the relaxation time τ_i and the relaxation pseudo-time σ on reaching equilibrium:[23]

- for $\tau_i, \sigma \leq 0.5$: this yields negative (pseudo-)diffusivity, which is unphysical;
- for $0.5 < \tau_i, \sigma \leq 0.55$: values too low can yield significant oscillation around equilibrium, better to stay clear;
- for $0.55 \leq \tau_i, \sigma < 1$: over-relaxation takes place, where the impacts of the (pseudo-)diffusivity are exaggerated over one (pseudo-)time step before reaching equilibrium;
- for $\tau_i, \sigma = 1$: the simulation relaxes fully, expressing the effects of the (pseudo-)diffusivity in one (pseudo-)time step towards equilibrium;
- for $\tau_i, \sigma > 1$: under-relaxation takes place, where the impacts of the (pseudo-)diffusivity take place over more than one (pseudo-)time step.

[xiii] Grid, referring to the discretization of space and time.

[xiv] As the lattice pseudo-time Δs has no value assigned to its "physical" counter-part, we use the scaling constant γ to change the pseudo-diffusivity χ and therefore the relaxation pseudo-time σ.

4.2.3 Resolution Limits

To model the EDL properly, we require the lattice space Δx to be (significantly) smaller than the Debye length λ ($\Delta x \ll \lambda$). The effects of the EDL are still significant at relatively far distance away from the anode; to fully model the EDL we have the length of the domain L to be ten times the Debye length λ ($L > 10\lambda$).

The ratio of the Debye length λ and the lattice space Δx is given by dimensionless Debye number De, which (interestingly) follows from the non-dimensional permittivity $\tilde{\epsilon}$:

$$\tilde{\epsilon} = \frac{\epsilon}{\mathcal{V}_\epsilon} = \frac{\epsilon \mathcal{P}\mathcal{S}}{\mathcal{C}} = \frac{\epsilon RT \Delta x}{F^2 c_0 \Delta x^3} = \frac{2}{\Delta x^2}\frac{\epsilon RT}{2F^2 c_0} = \frac{2\lambda^2}{\Delta x^2} = 2\mathrm{De}^2. \tag{4.12}$$

4.3 Non-Dimensional Equations

By applying the variable conversion factors $\mathcal{V}$ (see Equation 4.8) to any relevant equation, we find its dimensionless counterpart in lattice units. Notes on how the non-dimensionalization process has been carried out can be seen in Subsection A.1. The solvers and models which make up the simulation discussed previously will now only be used in dimensionless form, and are expanded upon now.

LBM Model Initialization (Dimensionless)

Concentration Initial Condition
$$c_i(\mathbf{x}, 0) = c_{i,0}$$

Electric Potential Initial Condition
$$\phi(\mathbf{x}, 0) = 0$$

Particle Population Initial Condition
$$w_j c_i(\mathbf{x}, 0) = f_{i,j}(\mathbf{x}, 0)$$

Potential Population Initial Condition
$$w_j \phi(\mathbf{x}, 0) = g_j(\mathbf{x}, 0, s)$$

The $c_i(t)$-LBM Model (Dimensionless)

Equilibrium Computation
$$f_{i,j}^{\mathrm{eq}}(\mathbf{x}, t) = w_j c_i(\mathbf{x}, t)\left(1 + 3\mathbf{u}_i^{\mathrm{m}}(\mathbf{x}, t)\cdot\mathbf{e}_j + \tfrac{9}{2}(\mathbf{u}_i^{\mathrm{m}}(\mathbf{x}, t)\cdot\mathbf{e}_j)^2 - \tfrac{3}{2}\mathbf{u}_i^{\mathrm{m}}(\mathbf{x}, t)\cdot\mathbf{u}_i^{\mathrm{m}}(\mathbf{x}, t)\right)$$

Relaxation
$$f_{i,j}^{\mathrm{col}}(\mathbf{x}, t) = f_{i,j}(\mathbf{x}, t) - \frac{f_{i,j}(\mathbf{x},t) - f_{i,j}^{\mathrm{eq}}(\mathbf{x},t)}{\tau_i} + w_j S_i(\mathbf{x}, t)$$

Propagation
$$f_{i,j}^{\mathrm{next}}(\mathbf{x} + \mathbf{e}_j, t+1) = (1 - p(\mathbf{x} + \mathbf{e}_j, t)) f_{i,j}^{\mathrm{col}}(\mathbf{x}, t) + p(\mathbf{x}, t) f_{i,j'}^{\mathrm{col}}(\mathbf{x} + \mathbf{e}_j, t)$$

Anodic Boundary Condition
$$f_{i,j}^{\mathrm{next}}(\mathbf{x}_{\mathrm{a}}, t+1) = f_{i,j'}^{\mathrm{col}}(\mathbf{x}_{\mathrm{a}}, t) + 6 w_j N_{\mathrm{ox}}(\mathbf{x}_{\mathrm{a}}, t)$$

Carbon-black-alginate Boundary Condition
$$f_{i,j}^{\mathrm{next}}(\mathbf{x}_{\mathrm{c}}, t+1) = f_{i,j'}^{\mathrm{col}}(\mathbf{x}_{\mathrm{c}}, t)$$

Bulk Boundary Condition
$$f_{i,j}^{\mathrm{next}}(\mathbf{x}_{\mathrm{b}}, t+1) = -f_{i,j'}^{\mathrm{col}}(\mathbf{x}_{\mathrm{b}}, t) + 2 w_j c_{i,0}$$

The $\phi(s)$-LBM Model (Dimensionless)

Equilibrium Computation
$$g_j^{\mathrm{eq}}(\mathbf{x},t,s) = w_j \phi(\mathbf{x},t,s)$$

Relaxation
$$g_j^{\mathrm{col}}(\mathbf{x},t,s) = g_j(\mathbf{x},t,s) - \frac{g_j(\mathbf{x},t,s) - g_j^{\mathrm{eq}}(\mathbf{x},t,s)}{\sigma} + w_j \frac{\chi_0 \rho(\mathbf{x},t)}{2\mathrm{De}^2}$$

Propagation
$$g_j^{\mathrm{next}}(\mathbf{x}+\mathbf{e}_j,t,s+1) = g_j^{\mathrm{col}}(\mathbf{x},t,s)$$

Anodic Boundary Condition
$$g_j^{\mathrm{next}}(\mathbf{x}_{\mathrm{a}},t,s+1) = g_{j'}^{\mathrm{col}}(\mathbf{x}_{\mathrm{a}},t,s) + 6w_j \frac{J(\mathbf{x}_{\mathrm{a}},t)}{\kappa(\mathbf{x}_{\mathrm{a}},t)}$$

Carbon-black-alginate Boundary Condition
$$g_j^{\mathrm{next}}(\mathbf{x}_{\mathrm{c}},t,s+1) = g_{j'}^{\mathrm{col}}(\mathbf{x}_{\mathrm{c}},t,s)$$

Bulk Boundary Condition
$$g_j^{\mathrm{next}}(\mathbf{x}_{\mathrm{b}},t,s+1) = -g_{j'}^{\mathrm{col}}(\mathbf{x}_{\mathrm{b}},t,s)$$

The Electrostatics Solver (Dimensionless)

Reaction Quotient
$$Q(\mathbf{x}_{\mathrm{a}},t) = \frac{c_{\mathrm{Zn(OH)_4}^{2-}}(\mathbf{x}_{\mathrm{a}},t)}{c^4_{\mathrm{OH}^-}(\mathbf{x}_{\mathrm{a}},t)} \cdot 10^9\,\mathrm{lm}^3/\mathrm{ls}^9$$

Nernst Equation
$$E_{\mathrm{ox}}(\mathbf{x}_{\mathrm{a}},t) = E^{\circ}_{\mathrm{ox}} + \tfrac{1}{n}\ln Q(\mathbf{x}_{\mathrm{a}},t)$$

Charge Density
$$\rho(\mathbf{x},t) = \textstyle\sum_i z_i c_i(\mathbf{x},t)$$

Conductivity
$$\kappa_i(\mathbf{x},t) = \textstyle\sum_i D_i z_i^2 c_i(\mathbf{x},t)$$

Pseudo-Diffusivity
$$\chi(\mathbf{x},t) = \gamma\Big((1-p)\epsilon_{\mathrm{r,e}} + p\epsilon_{\mathrm{r,p}}\Big)$$

Relaxation Pseudo-Time
$$\sigma = \tfrac{1}{2} + 3\chi(\mathbf{x},t)$$

The Electrokinetics Solver (Dimensionless

Overpotential
$$\eta(\mathbf{x}_{\mathrm{a}},t) = \phi_{\mathrm{s}} - \phi(\mathbf{x}_{\mathrm{a}},t) - E_{\mathrm{ox}}(\mathbf{x}_{\mathrm{a}},t)$$

Tafel Equation
$$J(\mathbf{x}_{\mathrm{a}},t) = J_0 \exp\left(\alpha_{\mathrm{a}}\eta(\mathbf{x}_{\mathrm{a}},t)\right)$$

Faraday's Law
$$N_{\mathrm{ox}}(\mathbf{x}_{\mathrm{a}},t) = J(\mathbf{x}_{\mathrm{a}},t)\tfrac{\nu}{n}$$

4.3
Non-Dimensional Equations

The Migrative Velocity Solver (Dimensionless)

Central FDM, $\hat{x}$-direction
$$\frac{\partial\phi(x,y,t)}{\partial x} \approx \frac{\phi(x+1,y,t)-\phi(x-1,y,t)}{2}$$

Central FDM, $\hat{y}$-direction
$$\frac{\partial\phi(x,y,t)}{\partial y} \approx \frac{\phi(x,y+1,t)-\phi(x,y-1,t)}{2}$$

Forward FDM, $+\hat{x}$-direction
$$\frac{\partial\phi(x,y,t)}{\partial x} \approx \frac{-3\phi(x,y,t)+4\phi(x+1,y,t)-\phi(x+2,y,t)}{2}$$

Forward FDM, $+\hat{y}$-direction
$$\frac{\partial\phi(x,y,t)}{\partial x} \approx \frac{-3\phi(x,y,t)+4\phi(x,y+1,t)-\phi(x,y+2,t)}{2}$$

Backward FDM, $-\hat{x}$-direction
$$\frac{\partial\phi(x,y,t)}{\partial x} \approx \frac{-3\phi(x,y,t)+4\phi(x+1,y,t)-\phi(x+2,y,t)}{2}$$

Backward FDM, $-\hat{y}$-direction
$$\frac{\partial\phi(x,y,t)}{\partial x} \approx \frac{3\phi(x,y,t)-4\phi(x,y-1,t)+\phi(x,y-2,t)}{2}$$

The Precipitation Kinetics Solver (Dimensionless)

For a position $\mathbf{x}$ with one of the following properties:

- $\mathbf{x} \in \Gamma_a \cup \Gamma_c$;
- has a neighbouring node $\mathbf{x} \pm 1$ where $p(\mathbf{x} \pm 1, t) \geq p_{\min}$,

Source/Sink Term Calculation
$$\begin{cases} S_i(\mathbf{x},t) = \nu_i k(c_{\mathrm{Zn(OH)_4{}^{2-}}}(\mathbf{x},t) - K), & c_{\mathrm{Zn(OH)_4{}^{2-}}} > K; \\ S_i(\mathbf{x},t) = 0, & c_{\mathrm{Zn(OH)_4{}^{2-}}} \leq K \end{cases}$$

If $(1 - p(\mathbf{x},t))/M_{\mathrm{ZnO}} > S_i(\mathbf{x},t)$ (meaning $p(\mathbf{x},t)$ will overshoot the available volume):

$$S_i(\mathbf{x},t) = (1 - p(\mathbf{x},t))/M_{\mathrm{ZnO}}$$

Updated Precipitate Fraction
$$p(\mathbf{x},t) = p(\mathbf{x},t-1) + S_i(\mathbf{x},t)M_{\mathrm{ZnO}}$$

All equations written in dimensionless units will have their tags in square brackets.

5 Benchmarking

5.1 Gouy-Chapman Theory 33
5.2 Analytical Benchmarks 33
5.2.1 $c_i(t)$-LBM Model Benchmark 35
5.2.2 $\phi(s)$-LBM Model Benchmark 38
5.2.3 Combined $c_i(t)$-LBM and $\phi(s)$-LBM Models Benchmark 41
5.3 COMSOL Benchmark 43

Now that the simulation is discretized and non-dimensionalized, we aim to benchmark the simulation to verify its validity through analytical benchmarks and a COMSOL benchmark.

After the non-dimensionalization process, we still have free reign over the space conversion factor $\mathcal{S}$ and the time conversion factor $\mathcal{T}$. The space conversion factor $\mathcal{S}$ determines how much physical space Δx equals the dimensionless distance between nodes $\Delta\tilde{x}$, and therefore dictates the spatial resolution of the simulation. Two things need to be taken into account for the lattice space Δx:

- the EDL needs to be modelled correctly, so $\Delta x \ll \lambda$ (see Subsubsection 4.2.3);
- the lattice volume Δx^3 needs to be large enough to encompass enough particles for kinetic theory to hold (see Subsection 3.1).

In the following benchmarks, the lattice spacing Δx will divide up the Debye length λ in either three, five, or ten dimensionless lattice spacings $\Delta\tilde{x}$,

The time conversion factor $\mathcal{T}$ determines how much physical time Δt passes for each one dimensionless time-step $\Delta\tilde{t}$. These affects the dimensionless relaxation time $\tilde{\tau}_i$, as the dimensionless diffusivity $\tilde{D}$ depends on Δt:

$$\tilde{\tau}_i = \frac{1}{2} + 3\tilde{D} = \frac{1}{2} + \frac{3D_i\Delta t}{\Delta x^2} \longrightarrow \Delta t = \frac{(\tilde{\tau}_i - \frac{1}{2})\Delta x^2}{3D}. \tag{5.1}$$

Similar reasoning can be applied to the relaxation pseudo-time σ:

$$\tilde{\sigma} = \frac{1}{2} + 3\tilde{\chi} = \frac{1}{2} + \frac{3\chi\Delta s}{\Delta x^2} \longrightarrow \Delta s = \frac{(\tilde{\sigma} - \frac{1}{2})\Delta x^2}{3\chi}. \tag{5.2}$$

Through these benchmarks, we can find the optimal values for Δx, Δt and Δs through changing the relaxation time τ_i and the relaxation pseudo-time σ respectively. The different benchmarks will be compared to an analytical solution of the PNP equations, and are compared through the root mean square error (RMSE).

The ability to simulate reaction phenomena is benchmarked through COMSOL, as no analytical solutions exist. COMSOL is widely used as an industry standard to model electrochemical systems.[22,31]

The precipitation phenomena will not be benchmarked, as there again exists no analytical solution, and neither does a standard method of implementing precipitation.[14,32,33]

5.1 Gouy-Chapman Theory

As mentioned before in Subsection 2.6, there exists an analytical solution for the PNP-system in the following case:[34]

- the simulation is one-dimensional (1D);
- we assume that the electric potential ϕ at the anode is held at a static electric potential ϕ_0;
- the electrolyte initially is a 1:1 symmetric solution of only monovalent ions p^+ and n^-, both present at a concentration c_0;
- the bulk a significant distance away from the anode is not impacted by the electric potential ϕ, and has the ionic concentrations p^+ and n^- held at c_0;
- the ions have the same diffusivity D;
- no reactions, and therefore no precipitation take place.

In this case, we find that the analytical solution for the concentrations$c_{\pm,\mathrm{a}}$ are given in steady-state ($\frac{\partial c_\pm}{\partial t} = 0$) by[34]

$$c_{\pm,\mathrm{a}}(x) = c_0 \exp\left(\mp \frac{F\phi(x)}{RT}\right), \tag{5.3}$$

$$c_{\pm,\mathrm{a}}(x) = \exp(\mp\phi(x)), \tag{5.4}$$

where the electric potential ϕ is given by

$$\phi_\mathrm{a}(x) = \frac{4RT}{F} \tanh^{-1}\left(\tanh\left(\frac{\phi_0 F}{4RT}\exp\left(-\frac{x}{\lambda}\right)\right)\right), \tag{5.5}$$

$$\phi_\mathrm{a}(x) = 4\tanh^{-1}\left(\tanh\left(\frac{\phi_0}{4}\exp\left(-\frac{x}{\mathrm{De}}\right)\right)\right). \tag{5.6}$$

5.2 Analytical Benchmarks

With the analytical solutions found in Equation 5.4 and Equation 5.6 we can perform the following benchmarks to verify the simulation's validity:

- keep the electric potential ϕ equal to the analytical solution (see Equation 5.6), run the $c_i(t)$-LBM model until steady-state, and compare the ionic concentrations c_+ and c_- to those given by the analytical solution (see Equation 5.4);
- the opposite: keep the ionic concentrations c_+ and c_- equal to the analytical solution (see Equation 5.4), run the $\phi(s)$-LBM model until steady-state, and compare the electric potential ϕ to that given by the analytical solution (see Equation 5.6);
- run both the the $c_i(t)$-LBM and the $\phi(s)$-LBM models until steady-state, and compare the electric potential ϕ and the ionic concentrations c_+ and c_- to the analytical solutions (see Equation 5.4 and Equation 5.6).

The dependency of the relaxation time τ_i/relaxation pseudo-time σ on the accuracy of the simulations is tested in these benchmarks. The values seen in Table 5.1 are used across all benchmarks. As the simulation is ran until steady-state and scales with the Debye length λ (see Equation 2.36 and Subsubsection 4.2.3), these values did not impact the simulation when changed.

Table 5.1: The values used to run the analytical benchmarks for the $c_i(t)$-LBM and the $\phi(s)$-LBM.

Constant	Value	Unit
Debye length λ	$9.71 \cdot 10^{-9}$	m
Domain length L	10λ	m
Simulation time t_{sim}	10^{-3}	s
Initial/Bulk concentrations c_0	1	$\text{mol}\,\text{m}^{-3}$
Static electric potential ϕ_0	$-\text{RT/F}$	V
Temperature T	298.15	K
Electrolyte relative permittivity $\epsilon_{\text{r,e}}$	80	-
Diffusivity D	10^{-9}	$\text{m}^2\,\text{s}^{-1}$

The domain Ω, which is one-dimensional (1D) (see Figure 5.1), has boundary conditions for the concentration $c_\pm$ and the electric potential ϕ seen in Table 5.2.

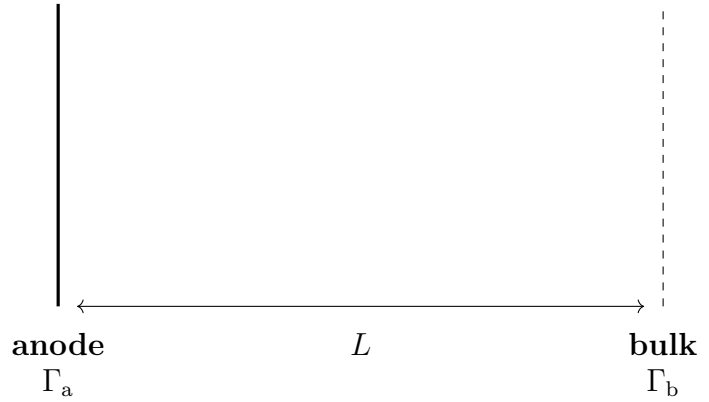


Figure 5.1: The one-dimensional (1D) domain Ω of length L, consisting of an anodic boundary Γ_a and a bulk boundary Γ_b.

Table 5.2: The boundary conditions applied in the one-dimensional domain Ω for the anodic boundary Γ_a and the bulk boundary Γ_b.

Boundary	Boundary Condition	
	$c_\pm$	ϕ
Anode Γ_a	$\frac{\partial c_\pm(x_\text{a},t)}{\partial x} = 0$	$\phi(x_\text{a},t) = \phi_0$
Bulk Γ_b	$c_\pm(x_\text{a},t) = 0$	$\phi(x_\text{b},t) = 0$

5.2.1 $c_i(t)$-LBM Model Benchmark

The benchmarking of the $c_i(t)$-LBM model follows the following flow chart (see Figure 5.2), where the Electrostatics Solver, the Electrokinetics Solver, and the $c_i(t)$-LBM model are replaced with the electric potential analytical solution $c_{\pm,\mathrm{a}}$.

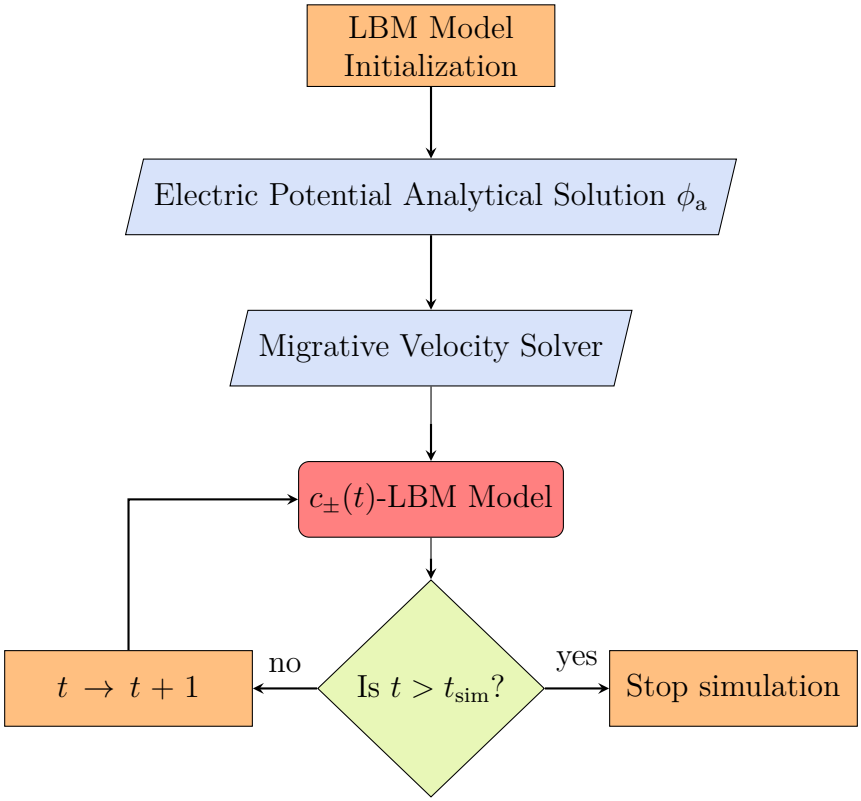


Figure 5.2: Flow chart of the simulation used for benchmarking the $c_i(t)$-LBM model.

The $c_\pm(t)$-LBM model is ran until a time of $t = t_\mathrm{sim}$ has been reached. Then, the output is compared to the analytical solution (see Equation 5.4) through the RMSE:

$$\mathrm{RMSE} = \sqrt{\frac{1}{l}\sum_x \Big(c_\pm(x, t = t_\mathrm{sim}) - c_{\pm,\mathrm{a}}(x)\Big)^2}. \tag{5.7}$$

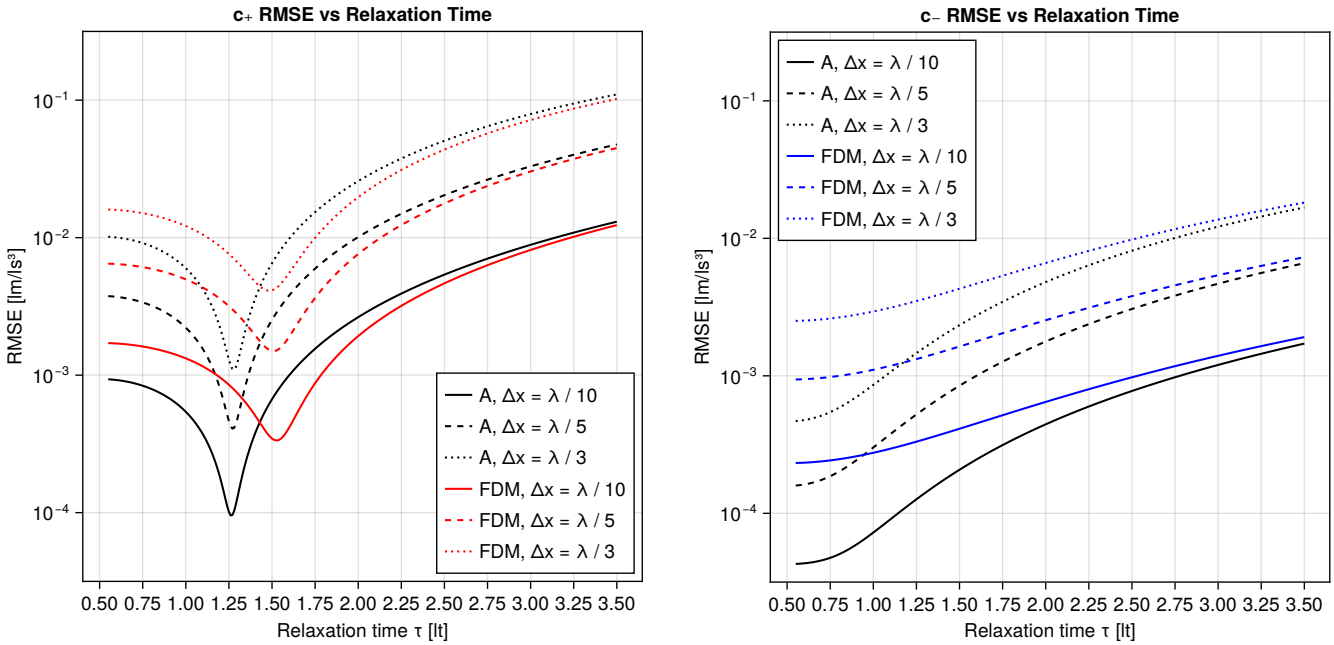
The RMSE gives an indication by how much the concentration $c_\pm$ deviates from the analytical solution for the concentration $c_{\pm,\mathrm{a}}$ in steady-state across the domain.

As the analytical solution to the electric potential ϕ is known, we can obtain the analytical spatial derivative of the electric potential $\frac{\partial \phi_\mathrm{a}}{\partial x}$ from Equation 5.6:

$$\frac{\partial \phi_\mathrm{a}(x)}{\partial x} = -\frac{2RT}{F\lambda}\sinh\left(\frac{F\phi_\mathrm{a}(x)}{2RT}\right), \tag{5.8}$$

$$\frac{\partial \phi_\mathrm{a}(x)}{\partial x} = -\frac{2}{\mathrm{De}}\sinh\left(\frac{\phi_\mathrm{a}(x)}{2}\right). \tag{5.9}$$

We will show both the benchmarking results from using the analytical spatial derivative of the electric potential $\frac{\partial \phi_\mathrm{a}}{\partial x}$ (referred to as method A) and the FDM (see **??**) in place of the Migrative Velocity Solver.



(a) Influence of the relaxation time τ_i on the RMSE of the p^+ concentration c_+. The lowest RMSE is reached at $\tau = 1.25\,\text{lt}$ when method A is used, and $\tau \approx 1.5\,\text{lt}$ when the FDM is used.

(b) Influence of the relaxation time τ_i on the RMSE of the n^- concentration c_+. Both method A and the FDM prefer a lower relaxation time τ_i for the smallest RMSE.

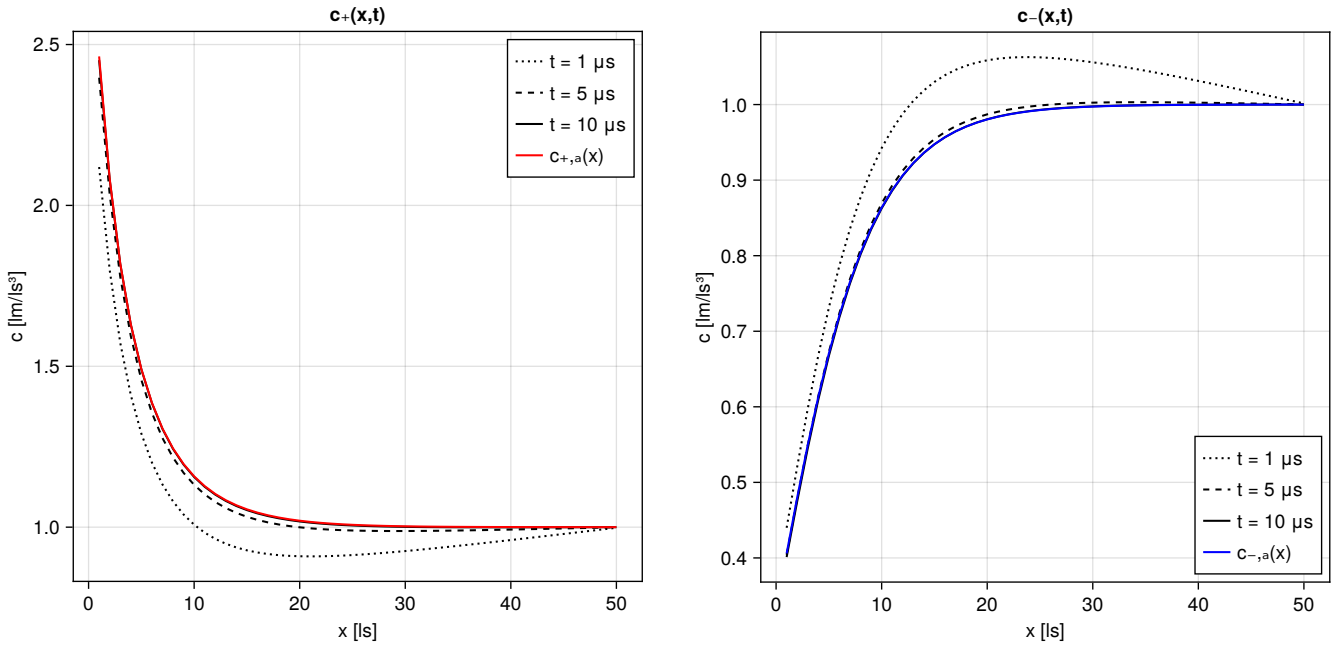
Figure 5.3: The RMSE of the p^+ and n^- concentrations $c_\pm$. Different behaviour of the RMSE in steady-state is observed between the two ions when the relaxation time τ_i changes. The size of the lattice space Δx impacts the RMSE too, where a lower Δx yields a lower RMSE.

From running the benchmarks for the p^+ and n^- concentrations $c_\pm$ separately (see Figure 5.3), we observe that the RMSE is influenced by the relaxation time τ_i — the difference in the shape of their graphs most likely caused by the migrative velocity u_i^m acting in opposite directions for the differently charged species p^+ and n^-. For the p^+ concentration c_+ (see Figure 5.3a), we find that an optimal value for the relaxation time τ_i exists for both method A and the FDM. The n^- concentration c_- (see Figure 5.3b) yields the lowest RMSE when a lower relaxation time τ_i is used.

Interestingly, the different methods do not have the same relaxation time τ_i yield the lowest RMSE. As the LBM is second order accurate ($\mathcal{O}(\Delta x^2)$), deviation compared to the analytical solution for the concentration $c_{\pm,\text{a}}$ is to be expected. As the migrative velocity u_i^m is directional, and has its direction be dependent on the valency z of the ions involved, we observe the following:[23]

- overall, as the relaxation time τ_i increases, the p^+ and n^- concentrations $c_\pm$ do not converge to the analytical solution for the concentration $c_{\pm,\text{a}}$ (see Subsection A.2), resulting in a higher RMSE;
- for the p^+ concentration c_+, we observe that the errors inherent to the LBM are cancelled out at a certain relaxation time τ_i "sweet spot", beyond which the errors compound each other;
- as the FDM yields a less accurate spatial derivative of the electric potential $\frac{\partial \phi}{\partial x}$, the relaxation time τ_i "sweet spot" shifts, as the FDM brings with it a bigger error;
- a slight shift between different values for the lattice spacing Δx when using the FDM is observed, indicating a different relaxation time τ_i "sweet spot" when the lattice spacing Δx changes.

From this, we will now take the relaxation time $\tau = 1.25$, and $\Delta x = \lambda/5$, as this yields similar accuracies for the p^+ and n^- concentrations $c_\pm$ whilst modelling the EDL with enough resolution (see Subsubsection 4.2.3). A simulation ran at these values is shown in Figure 5.4.



(a) The evolution of the p^+ concentration c_+.

(b) The evolution of the n^- concentration c_-.

Figure 5.4: The evolution of the p^+ and n^- concentrations $c_\pm$. The positive ions p^+ move towards the anode, whilst the negative ions n^- move away. Steady-state is reached around $t \approx 1\,\mu s$, where the p^+ and n^- concentrations $c_\pm$ approach the analytical solution for the concentration $c_{\pm,a}$.

Figure 5.4 shows how the simulation converges towards the analytical solution for the concentration $c_{\pm,a}$. The anode has the p^+ concentration c_+ move towards it, and the n^- concentration c_- move away from it. Note how more positive charges accumulate at the anode than negative charges leave, forming the EDL (see Subsubsection 2.4.4).

5.2.2 $\phi(s)$-LBM Model Benchmark

The benchmarking of the $\phi(s)$-LBM model follows the following flow chart[xv] (see Figure 5.5), where the Electrostatics Solver and the $c_i(t)$-LBM model are replaced with the concentration analytical solution $c_{\pm,\mathrm{a}}$.

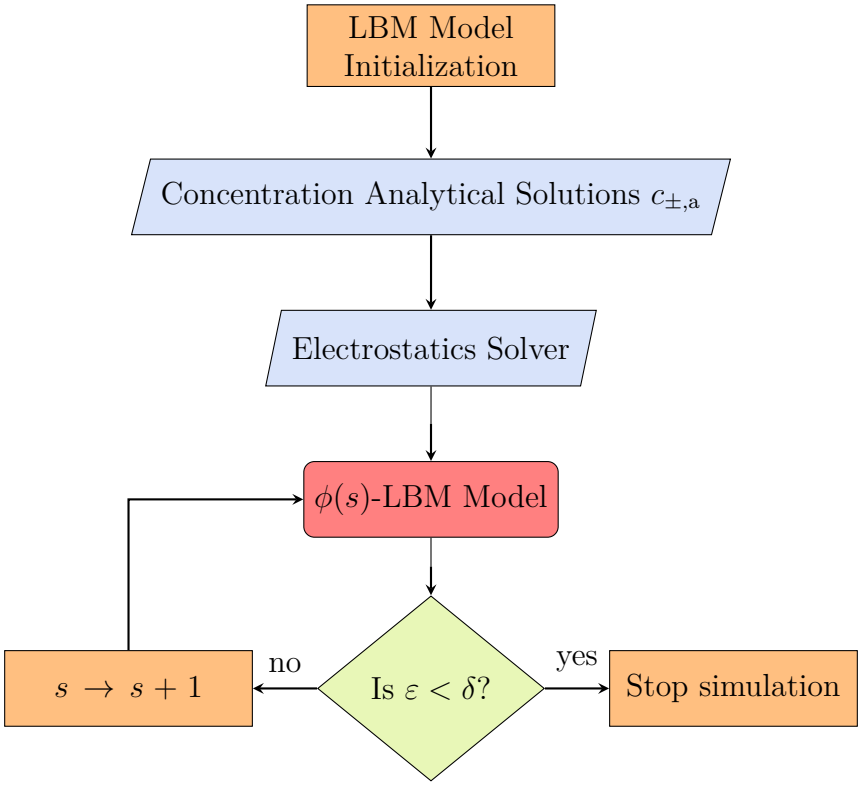


Figure 5.5: Flow chart of the simulation used for benchmarking the $\phi(s)$-LBM model.

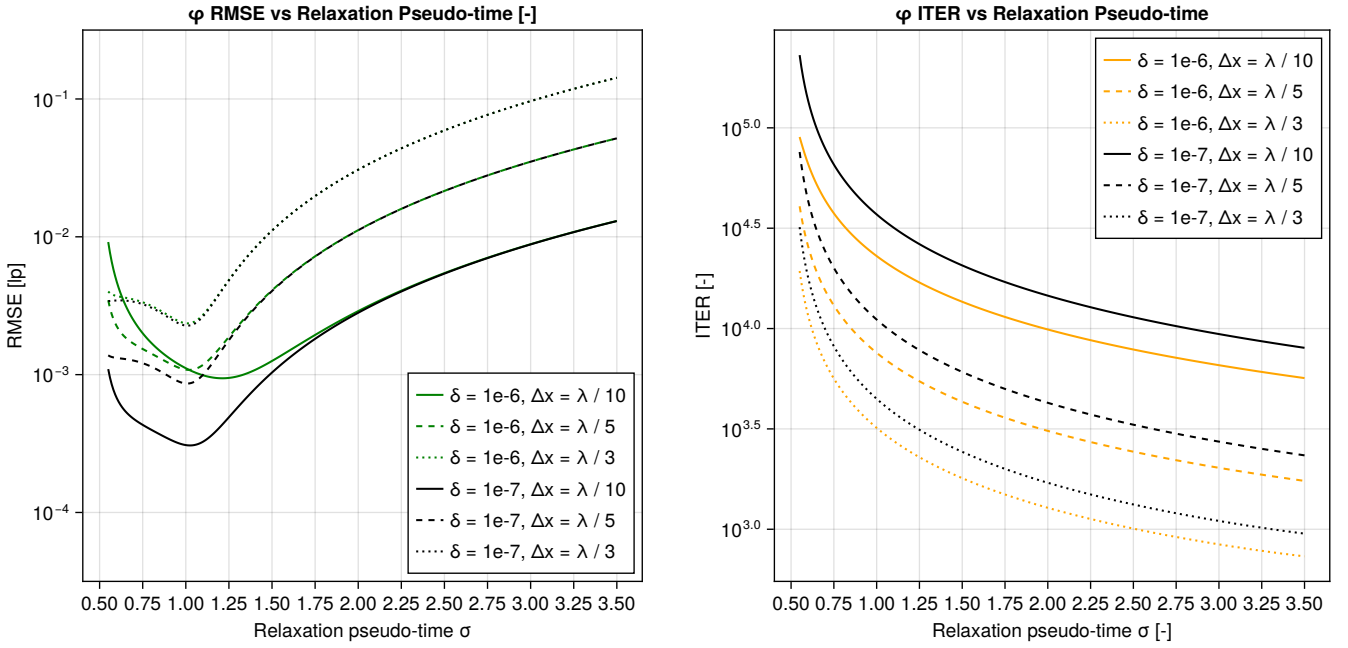
The $\phi(s)$-LBM model is ran until the criteria $\varepsilon < \delta$ has been reached at a pseudo-time s_{end}. The output is again compared to the analytical solution (see Equation 5.6) through the RMSE:

$$\mathrm{RMSE} = \sqrt{\frac{1}{l}\sum_{x}\Big(\phi(x, s = s_{\mathrm{end}}) - \phi_{\mathrm{a}}(x)\Big)^2}. \qquad [5.10]$$

The RMSE once more gives an indication by how much the electric potential ϕ deviates from the analytical solution for the electric potential ϕ_{a} in steady-state across the domain.

Different values for the threshold δ[xvi] are used, which will determine how many iterations or ITER are needed to reach convergence. The amount of iterations ITER needed to reach steady-state is then considered when choosing the value for the threshold δ.

[xv] No re-running of the Electrokinetics Solver, as no reactions take place in this benchmark.
[xvi] Only values for the threshold δ which yield a similar RMSE to the $c_i(t)$-LBM benchmarks are considered.



(a) Influence of the relaxation psuedo-time σ on the RMSE of the electric potential ϕ. The lowest RMSE is reached at $\sigma = 1$ for both threshold δ values used.

(b) Influence of the relaxation pseudo-time σ on the ITER needed to reach steady-state. As bigger pseudo-time-steps Δs are taken for larger relaxation pseudo-times σ, less iterations are needed.

Figure 5.6: The RMSE and ITER of the electric potential ϕ. The behaviour of the RMSE in steady-state seems unpredictable when the threshold δ or the lattice spacing Δx changes. ITER seems to drop exponentially as the relaxation pseudo-time σ decreases.

Figure 5.6a shows that the pseudo-kinetic theory applied to the Poisson equation (see Subsubsection 3.1.3) yields valid results, with an RMSE low enough to give an accurate electric potential ϕ. We again observe how the RMSE is affected by the pseudo-relaxation time, where the lowest RMSE is achieved at a relaxation pseudo-time of $\sigma \approx 1$.[xvii] The combination of the spatial step Δx being small ($\Delta x = \lambda/10$), and the threshold δ being too high ($\delta = 10^{-6}$) results in the criteria $\varepsilon < \delta$ to be reached too early, resulting in a higher overall error which prefers a higher relaxation pseudo-time σ to compensate.

Figure 5.6b shows how the amount of iterations ITER drops as the relaxation pseudo-time σ increases, which is expected as larger pseudo-time-steps Δs are taken, converging the electric potential ϕ to steady-state earlier.

From Figure 5.6, we observe the following:

- a relaxation pseudo-time σ too low or too high has the electric potential ϕ not converge to the analytical solution for the electric potential ϕ_a by either overshooting or undershooting it (see Subsection A.2), resulting in a higher RMSE;
- a spatial step Δx too small allows for the criteria $\varepsilon < \delta$ to be reached too early for the threshold δ values tested.

We will now take the relaxation pseudo-time $\sigma = 1$, and the threshold $\delta = 10^{-6}$, as this yields an accurate enough electric potential ϕ whilst keeping the amount of iterations ITER suitable for running simulations. A simulation ran at these values is shown in Figure 5.7.

[xvii] This difference in preferred relaxation pseudo-time σ compared to the preferred relaxation time τ_i (see Figure 5.3) could be attributed to there not being a pseudo-velocity flux present in the pseudo-transient Poisson equation (see Equation 3.10).

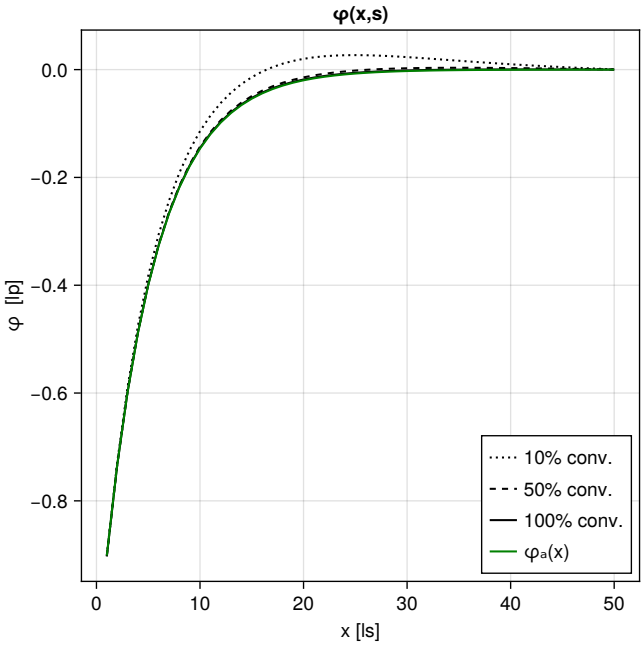


Figure 5.7: The evolution of the electric potential ϕ, given for 10%, 50%, and 10% steady-state convergence (conv.). Steady-state is reached after 7569 iterations, where the electric potential ϕ approaches the analytical solution for the electric potential ϕ_{a}.

Figure 5.7 shows how the simulation converges towards the analytical solution for the electric potential ϕ_{a}. The electric potential ϕ is held at a static electric potential ϕ_0 at the anode for these benchmarks, on the assumption that the electric potential ϕ near the anode is known and does not change.

5.2.3 Combined $c_i(t)$-LBM and $\phi(s)$-LBM Models Benchmark

The final analytical benchmark is performed on the combined $c_i(t)$-LBM and $\phi(s)$-LBM models, which now no longer depend on any analytical solutions (see Figure 5.8).

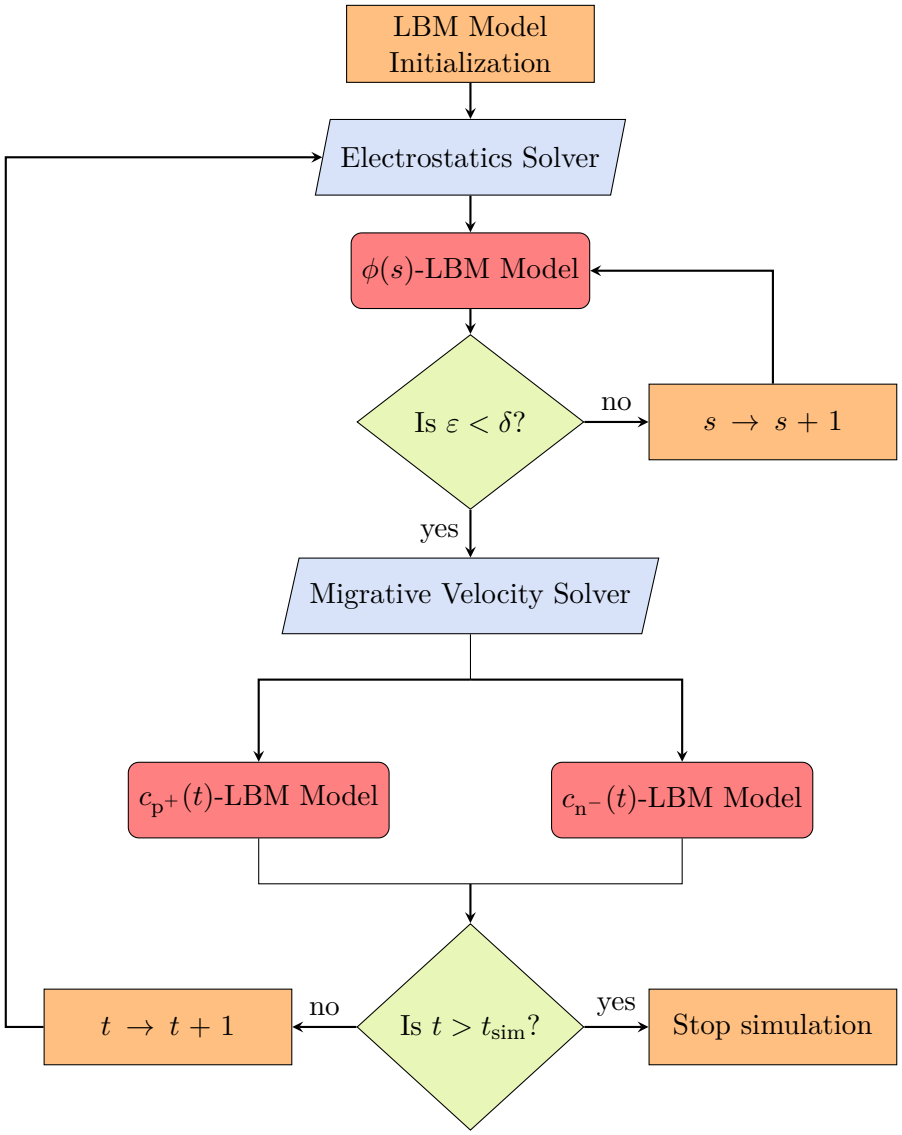
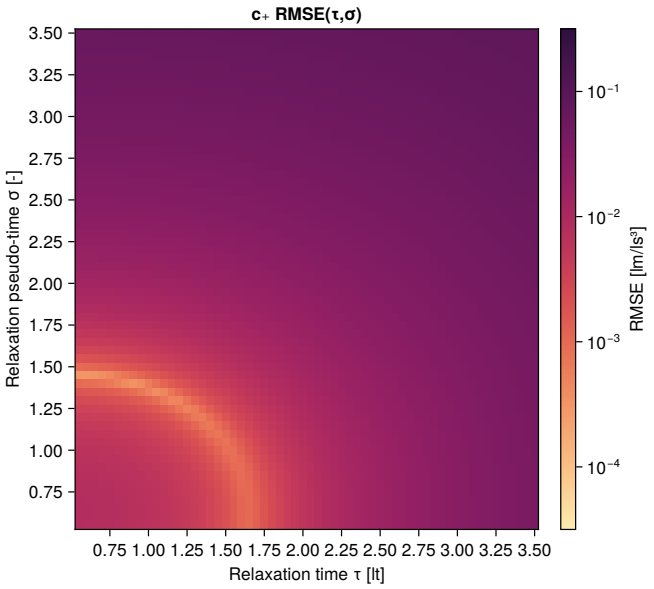
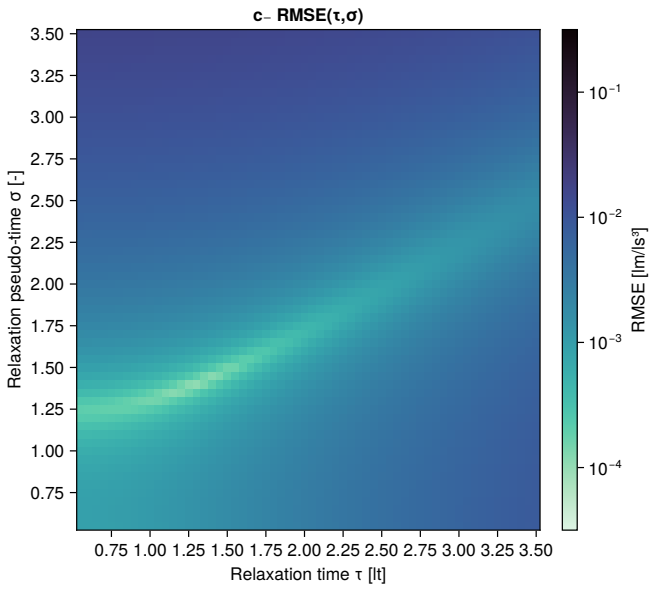


Figure 5.8: Flow chart of the simulation used for benchmarking the combined $c_i(t)$-LBM and $\phi(s)$-LBM models.

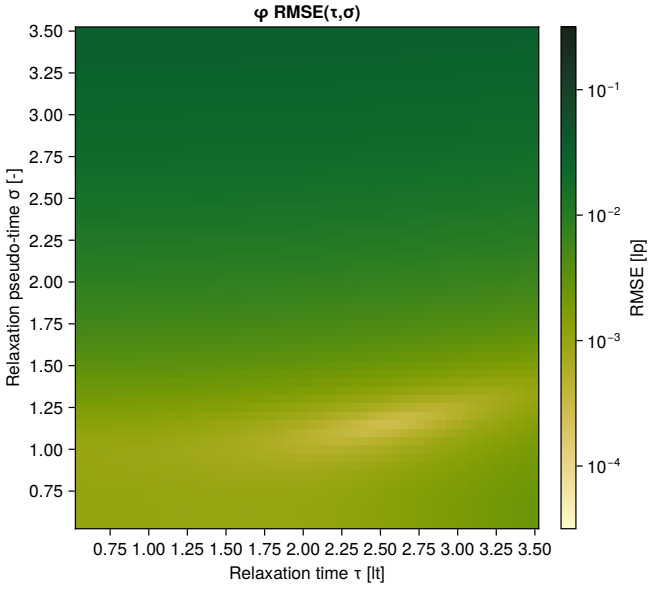
The $c_+(t)$-LBM, $c_-(t)$-LBM and $\phi(s)$-LBM models are ran at varying relaxation times τ_i and relaxation pseudo-times σ, all with a threshold $\delta = 10^{-6}$. Then, the RMSE (see Equation 5.7 and Equation 5.10) is calculated for each LBM model and plotted against the relaxation time τ_i and relaxation pseudo-time σ (see Figure 5.9).



(a) RMSE of the p^+ concentration c_+, preferring a lower relaxation pseudo-time σ as the relaxation time τ_i increases.



(b) RMSE of the n^- concentration c_-, preferring a higher relaxation pseudo-time σ as the relaxation time τ_i increases.



(c) RMSE of the electric potential ϕ, preferring a constant relaxation pseudo-time $\sigma \approx 1$ as the relaxation time τ_i increases.

Figure 5.9: The RMSE of the concentrations $c_\pm$ and the electric potential ϕ for varying relaxation times τ_i and relaxation pseudo-times σ — different relations between the variables are observed.

We observe "sweet spot" regions, where a combination of the relaxation time τ_i and the relaxation pseudo-time σ yields the lowest RMSE. These low-RMSE regions are caused by the $c_\pm(t)$-LBM models and the $\phi(s)$-LBM model both running at a less preferred relaxation time τ_i and relaxation pseudo-time σ, but their combination has their errors cancel out (one $c_\pm(t)$-LBM model overshoots the analytical solution, whilst the $\phi(s)$-LBM model undershoots it, see Subsection A.2). The values found in the previous two benchmarks of $(\tau, \sigma) = (1.5, 1)$ lies in the low-RMSE region seen in Figure 5.9a, but not in the one seen in Figure 5.9b, as the c_--LBM model prefers a lower relaxation time τ_i. The $\phi(s)$-LBM appears to yield a low RMSE for any relaxation time τ_i at a relaxation pseudo-time $\sigma \approx 1$, which could be caused again by the overshoot-undershoot errors of the $c_\pm(t)$-LBM models cancelling each other out.

5.3 COMSOL Benchmark

The simulation is ran again, now including the species introduced in Subsection 2.2, and the oxidation reaction of zinc to zincate (see Equation 2.1). This is calculated through the Electrokinetics Solver, and running the $c_i(t)$-LBM model for each species i. The domain Ω is kept the same as the previous benchmarks (see Figure 5.1); the values seen in Table 5.3 are used for this benchmark, which is expanded to include the diffusivity D_i of each species i together with the constants used by the Electrokinetics Solver; the boundary conditions seen in Table 5.4 now include the Neumann boundary condition for the electric potential ϕ at the anodic boundary Γ_a. A flow chart of the simulation can be seen in Figure 5.10.

Table 5.3: The values used by the simulation to run the COMSOL benchmarks.[17,35]

Constant	Value	Unit
Debye length λ	$9.71 \cdot 10^{-9}$	m
Domain length L	10λ	m
Simulation time t_sim	10^{-3}	s
Initial/Bulk concentrations c_0	1	$\mathrm{mol\,m^{-3}}$
Temperature T	298.15	K
Electrolyte relative permittivity $\epsilon_\mathrm{r,e}$	80	-
Standard oxidation potential E°_ox	1.2	V
Solid electric potential ϕ_s	1.25	V
Exchange current density J_0	1	$\mathrm{C\,m^{-2}\,s^{-1}}$
Diffusivity of K^+ D_{K^+}	$1.96 \cdot 10^{-9}$	$\mathrm{m^2\,s^{-1}}$
Diffusivity of OH^- D_{OH^-}	$5.27 \cdot 10^{-9}$	$\mathrm{m^2\,s^{-1}}$
Diffusivity of $Zn(OH)_4{}^{2-}$ $D_{Zn(OH)_4{}^{2-}}$	$0.10 \cdot 10^{-9}$	$\mathrm{m^2\,s^{-1}}$
Pseudo-diffusivity χ	1/6	-
Scaling constant γ	1/480	-
Relaxation pseudo-time $\tilde{\sigma}$	1.0	-
Threshold δ	10^{-6}	-

The solid electric potential ϕ_s is taken close to the standard oxidation potential E°_ox. As Equation 5.1 requires only one value for the diffusivity D_i to scale the space and time conversion factors $\mathcal{S}$ and $\mathcal{T}$, a reference diffusivity of $D_\mathrm{ref} = 2\times10^9\,\mathrm{m^2\,s^{-1}}$ is taken to yield a reference relaxation time of $\tau_\mathrm{ref} = 1.5\,\mathrm{lt}$. This yields respective relaxation times of $\tau_{OH^-} = 3.14\,\mathrm{lt}$, $\tau_{K^+} = 1.48\,\mathrm{lt}$, and $\tau_{Zn(OH)_4{}^{2-}} = 0.55\,\mathrm{lt}$.[xviii]

Table 5.4: Updated boundary conditions applied in the one-dimensional domain Ω for the anodic boundary Γ_a and the bulk boundary Γ_b.

Boundary	Boundary Condition	
	c_i	ϕ
Anode Γ_a	$\frac{\partial c_i(x_\mathrm{a},t)}{\partial x} = -\frac{\mathbf{N}_i^\mathrm{ox}(x_\mathrm{a},t)}{D_i} - \frac{z_i F}{RT} c_i(x_\mathrm{a},t)\nabla\phi(x_\mathrm{a},t)$	$\frac{\partial\phi(x_\mathrm{a},t)}{\partial x} = -\frac{\mathbf{J}(x_\mathrm{a},t)}{\chi\kappa(x_\mathrm{a},t)}$
Bulk Γ_b	$c_i(x_\mathrm{b},t) = c_{i,0}$	$\phi(x_\mathrm{b},t) = 0$

[xviii] Due to the diffusivity of OH^- being higher than that of K^+, OH^- ends up receiving a relatively high relaxation time τ_{OH^-} — although negative species prefer a lower relaxation time τ_i, it is still deemed acceptable to simulate with as the RMSE is still relatively low (see Figure 5.4b).

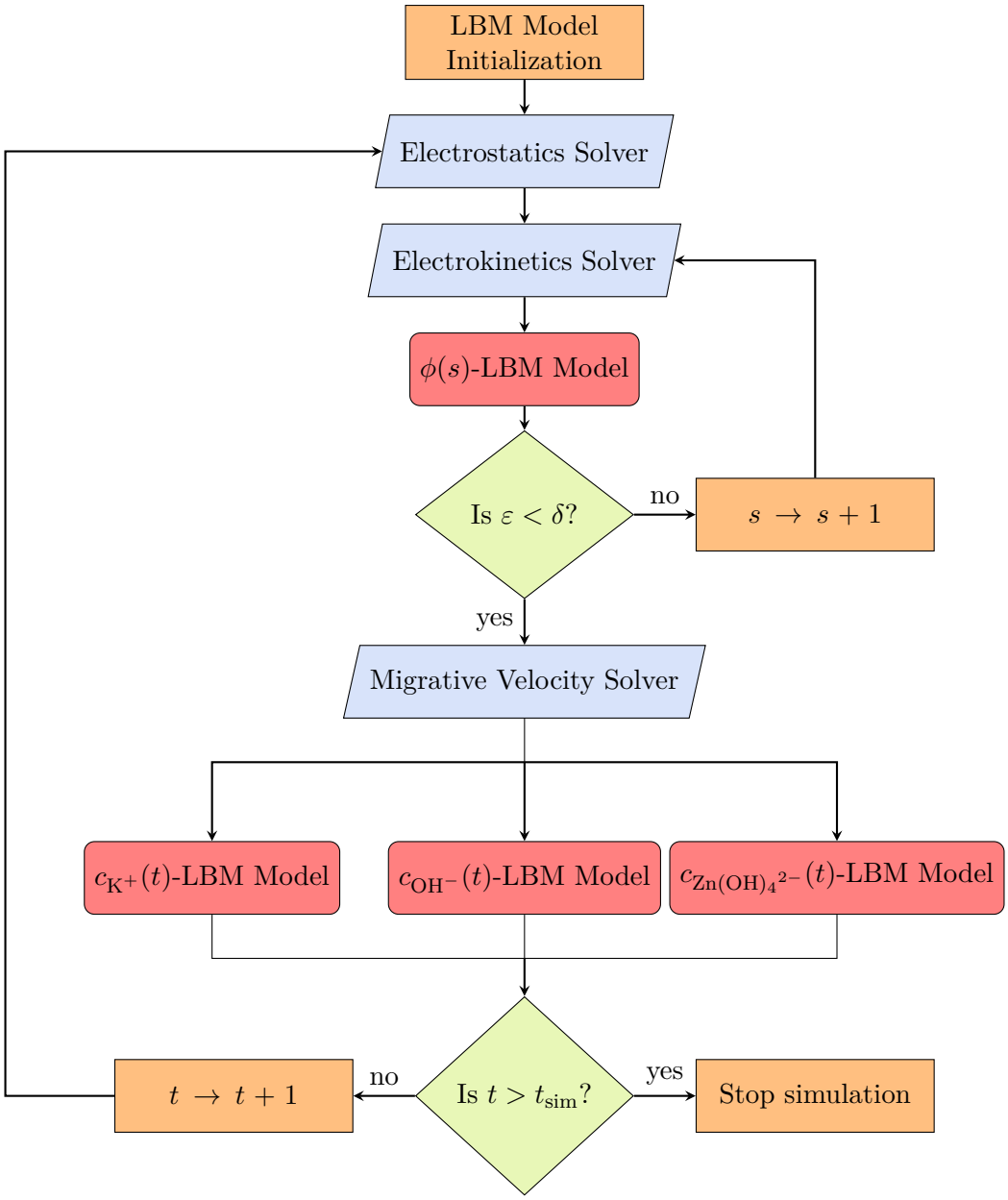
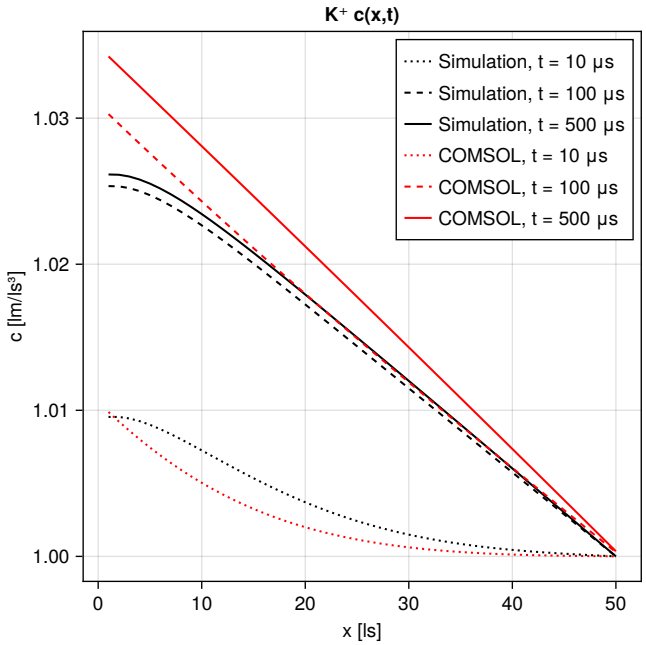


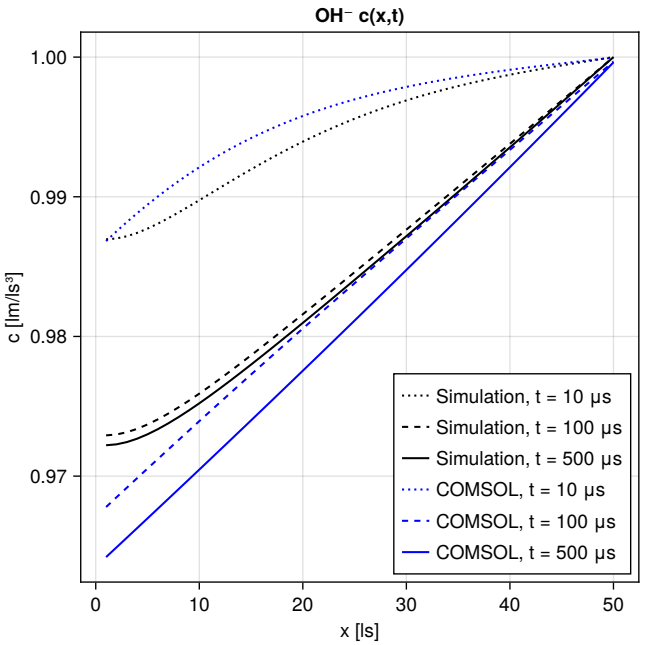
Figure 5.10: Flow chart of the simulation used for benchmarking with COMSOL.

The results of this benchmark, together with the results of a COMSOL model running the same simulation, are shown in Figure 5.11. The simulations ran for a time of $t_{sim} = 1\,\text{ms}$, and both reached steady-state at $t \approx 500\,\mu\text{s}$.

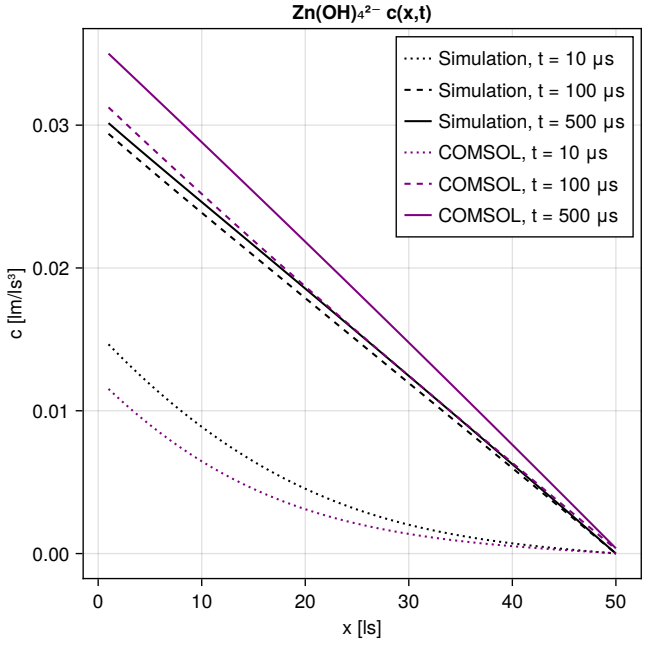
COMSOL uses different calculation methods for the evolution of the concentrations c_i and the electric potential ϕ (which are carried out through the finite-element method (FEM)), and also computes the electric potential ϕ through assuming electro-neutrality, not through solving the Poisson equation. It is therefore not expected that the LBM simulation and the COMSOL simulation will exactly yield the same results. Still, similar behaviour and comparable results were expected and are observed.[31,36]



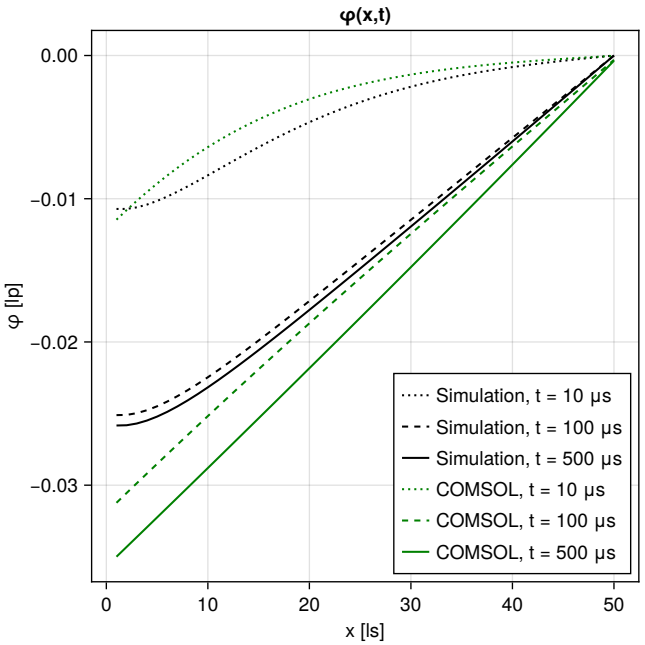
(a) The evolution of the K^+ concentration c_{K^+}.



(b) The evolution of the OH^- concentration c_{OH^+}.



(c) The evolution of the $Zn(OH)_4{}^{2-}$ concentration $c_{Zn(OH)_4{}^{2-}}$.



(d) The evolution of the electric potential ϕ.

Figure 5.11: The evolution of the concentrations c_i and the electric potential ϕ following from the LBM simulation and the COMSOL simulation. Similar behaviour as to the previous benchmarks is observed for the LBM simulation — the COMSOL simulation differs, mainly in the calculation of the electric potential ϕ.

The LBM simulation seem to have the concentrations c and electric potential ϕ evolve differently over time, where the largest discrepancy is observed at the anodic boundary Γ_a for the K^+ concentration c_{K^+} (see Figure 5.11a), the OH^- concentration c_{OH^-} (see Figure 5.11b) and the electric potential ϕ (see Figure 5.11d). Interestingly, the same can not be said about the evolution of the zincate concentration $c_{Zn(OH)_4{}^{2-}}$, which has the LBM simulation follow the same behaviour as the COMSOL simulation. The LBM simulation reaches different steady-state values than the COMSOL model.

6 Application

6.1 Precipitation Demonstration 47
6.2 External Electric Potential Demonstration 55
6.2.1 Perpendicular Electric Potential 56
6.2.2 Diagonal Electric Potential 61
6.2.3 Parallel Electric Potential 66

The benchmarking process has shown that the simulation can deliver results conform with the analytical solutions. Although no one-to-one congruence exists between the LBM simulation and the COMSOL simulation, similar behaviour in simulation the oxidation reaction was observed. Based on these benchmarks, the simulation will now be ran in 2D including precipitation to show an application of this simulation.

The two-dimensional domain Ω can be seen in Figure 6.1, consisting of an anodic boundary Γ_a next to carbon-black-alginate boundaries Γ_c. The bulk boundaries Γ_b are placed a distance of ten Debye lengths 10λ away from the anodic boundary Γ_a. We find for the height $H = 10\lambda$ and the length $L = 3H = 30\lambda$. The values used for this simulation can be seen in Table 6.1. The boundary conditions used can be seen in Table 6.2. A flow chart of the simulation can be seen in Figure 6.2.

Together with the concentrations c_i, the electric potential ϕ and the precipitation fraction p, we also calculate the current I (see Equation 2.15), which in its discretized form is given by

$$I(t) = \sum_{\mathbf{x}_\mathrm{a}} J(\mathbf{x}_\mathrm{a}, t)\Delta x^2; \qquad (6.1) \qquad\qquad I(t) = \sum_{\mathbf{x}_\mathrm{a}} J(\mathbf{x}_\mathrm{a}, t). \qquad [6.2]$$

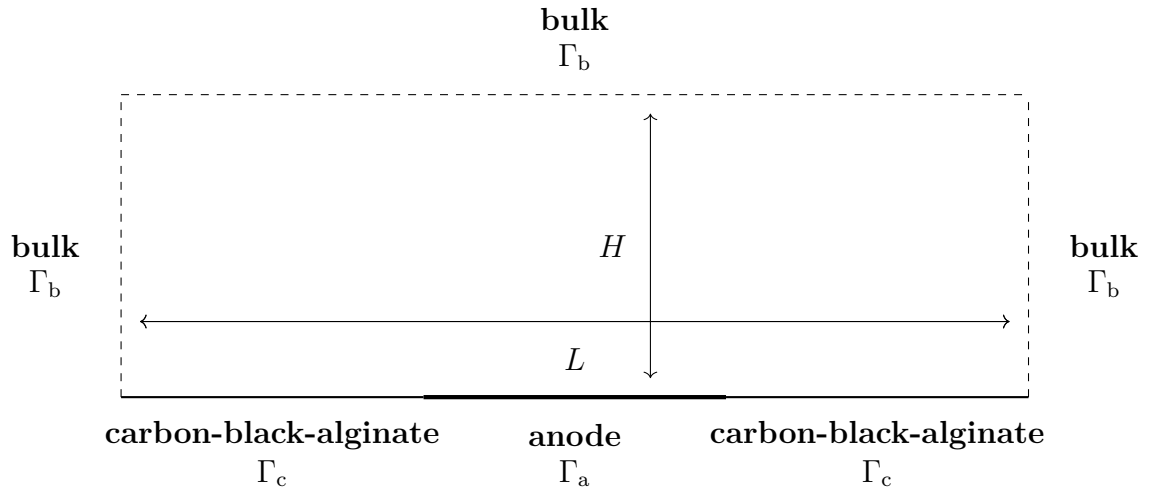


Figure 6.1: The two-dimensional (2D) domain Ω of length L and height H, consisting of an anodic boundary Γ_a (of size H), bulk boundary Γ_b, and carbon-black-alginate boundaries Γ_c (both of size H).

6.1 Precipitation Demonstration

Table 6.1: The values used by the simulation to demonstrate reaction-precipitation phenomena.[17,35]

Constant	Value	Unit
Debye length λ	$9.71 \cdot 10^{-9}$	m
Domain length L	10λ	m
Simulation time t_{sim}	10^{-3}	s
Initial/Bulk concentrations c_0	1	$\text{mol}\,\text{m}^{-3}$
Temperature T	298.15	K
Electrolyte relative permittivity $\epsilon_{\text{r,e}}$	80	-
Precipitate relative permittivity $\epsilon_{\text{r,p}}$	8	-
Standard oxidation potential E°_{ox}	1.2	V
Solid electric potential ϕ_{s}	1.25	V
Exchange current density J_0	1	$\text{C}\,\text{m}^{-2}\,\text{s}^{-1}$
Diffusivity of K^+ D_{K^+}	$1.96 \cdot 10^{-9}$	$\text{m}^2\,\text{s}^{-1}$
Diffusivity of OH^- D_{OH^-}	$5.27 \cdot 10^{-9}$	$\text{m}^2\,\text{s}^{-1}$
Diffusivity of $Zn(OH)_4{}^{2-}$ $D_{Zn(OH)_4{}^{2-}}$	$0.10 \cdot 10^{-9}$	$\text{m}^2\,\text{s}^{-1}$
Pseudo-diffusivity χ	1/6	-
Scaling constant γ	1/480	-
Relaxation pseudo-time $\tilde{\sigma}$	1.0	-
Threshold δ	10^{-6}	-
Standard Gibbs free energy of reaction ΔG°_{rxn}	-5.763	$\text{V}\,\text{C}\,\text{mol}^{-1}$
Solubility product K	$1.03 \cdot 10^{-2}$	$\text{mol}\,\text{m}^{-3}$
Zinc oxide molar volume M	$1.45 \cdot 10^{-5}$	$\text{mol}\,\text{m}^{-3}$
Reaction rate k	5	s^{-1}
Minimum precipitation $p_{\min}$	0.05	-

As the values for the reaction rate k and minimum precipitate fraction $p_{\min}$ (the amount of precipitate that needs to be present at a neighbouring lattice node for precipitation to take place at a position $\mathbf{x}$) are unknown, dummy values have been used for demonstration purposes of the Precipitation Solver.

Table 6.2: The boundary conditions applied in the two-dimensional domain Ω for the anodic boundary Γ_{a}, the bulk boundary Γ_{b}, and the carbon-black-alginate boundaries Γ_{c}.

Boundary	Boundary Condition	
	c_i	ϕ
Anode Γ_{a}	$\nabla_{\text{n}} c_i(\mathbf{x}_{\text{a}}, t) = -\frac{\mathbf{N}_i^{\text{ox}}(\mathbf{x}_{\text{a}},t)}{D_i} - \frac{z_i F}{RT} c_i(\mathbf{x}_{\text{a}}, t) \nabla\phi(\mathbf{x}_{\text{a}}, t)$	$\nabla_{\text{n}}\phi(\mathbf{x}_{\text{a}}, t) = -\frac{\mathbf{J}(\mathbf{x}_{\text{a}},t)}{\kappa(\mathbf{x}_{\text{a}},t)}$
Bulk Γ_{b}	$c_i(\mathbf{x}_{\text{b}}, t) = c_{i,0}$	$\phi(\mathbf{x}_{\text{b}}, t) = 0$
Carbon-black-alginate Γ_{c}	$\nabla_{\text{n}} c_i(\mathbf{x}_{\text{c}}, t) = \mathbf{0}$	$\nabla_{\text{n}}\phi(\mathbf{x}_{\text{c}}, t) = \mathbf{0}$

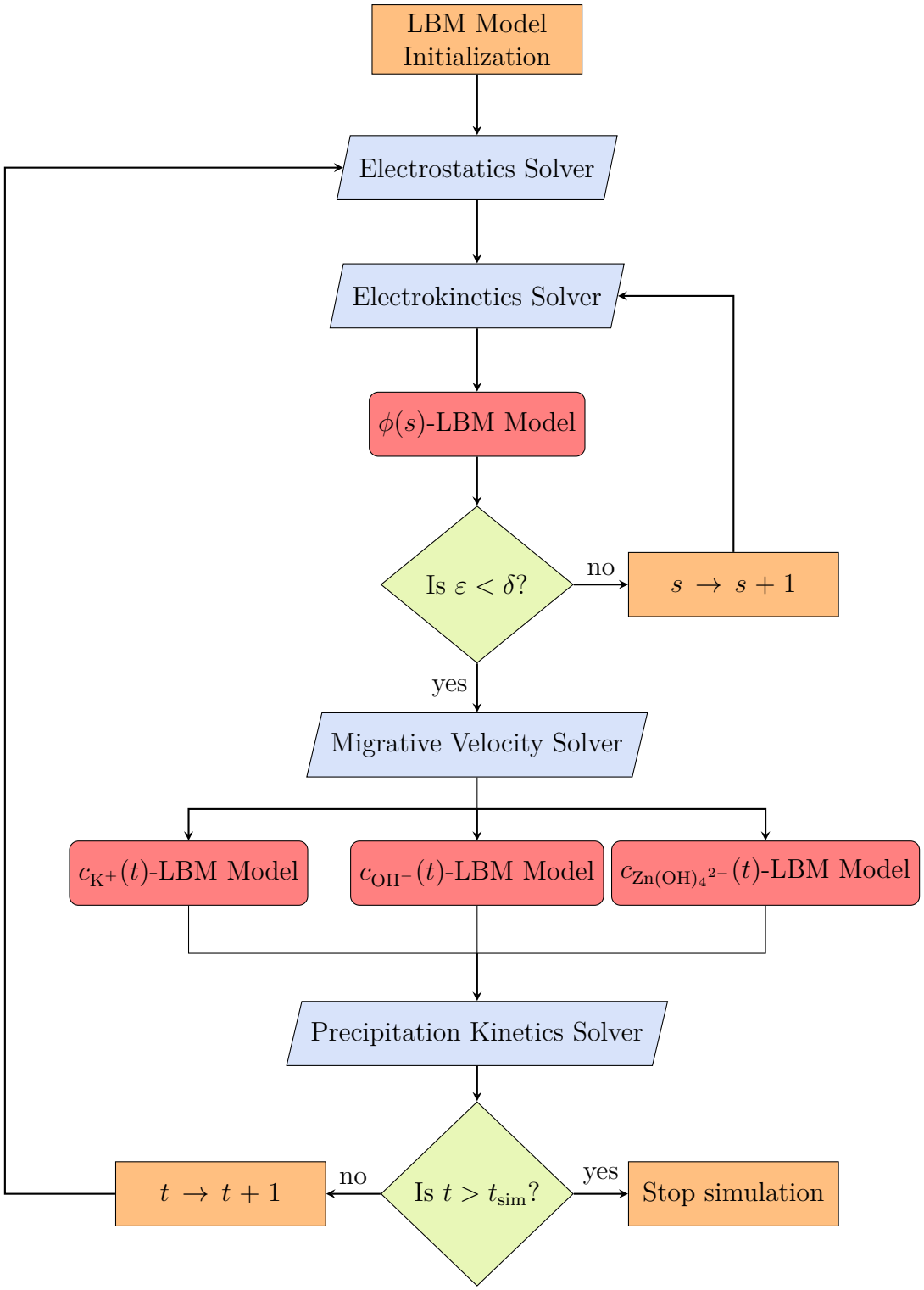


Figure 6.2: Flow chart of the simulation used for demonstrating reaction-precipitation phenomena.

The results following are of the concentrations c_i[xix], the precipitation fraction p, the Electric Potential ϕ for times $t = 100\,\mu s$, $t = 1\,ms$, $t = 5\,ms$ and $t = 10\,ms$ (shown from top to bottom), together with the evolution of the current I.

[xix]Note how the legends emphasise the difference from the initial bulk concentrations $c_{i,0}$.

6.1
Precipitation Demonstration

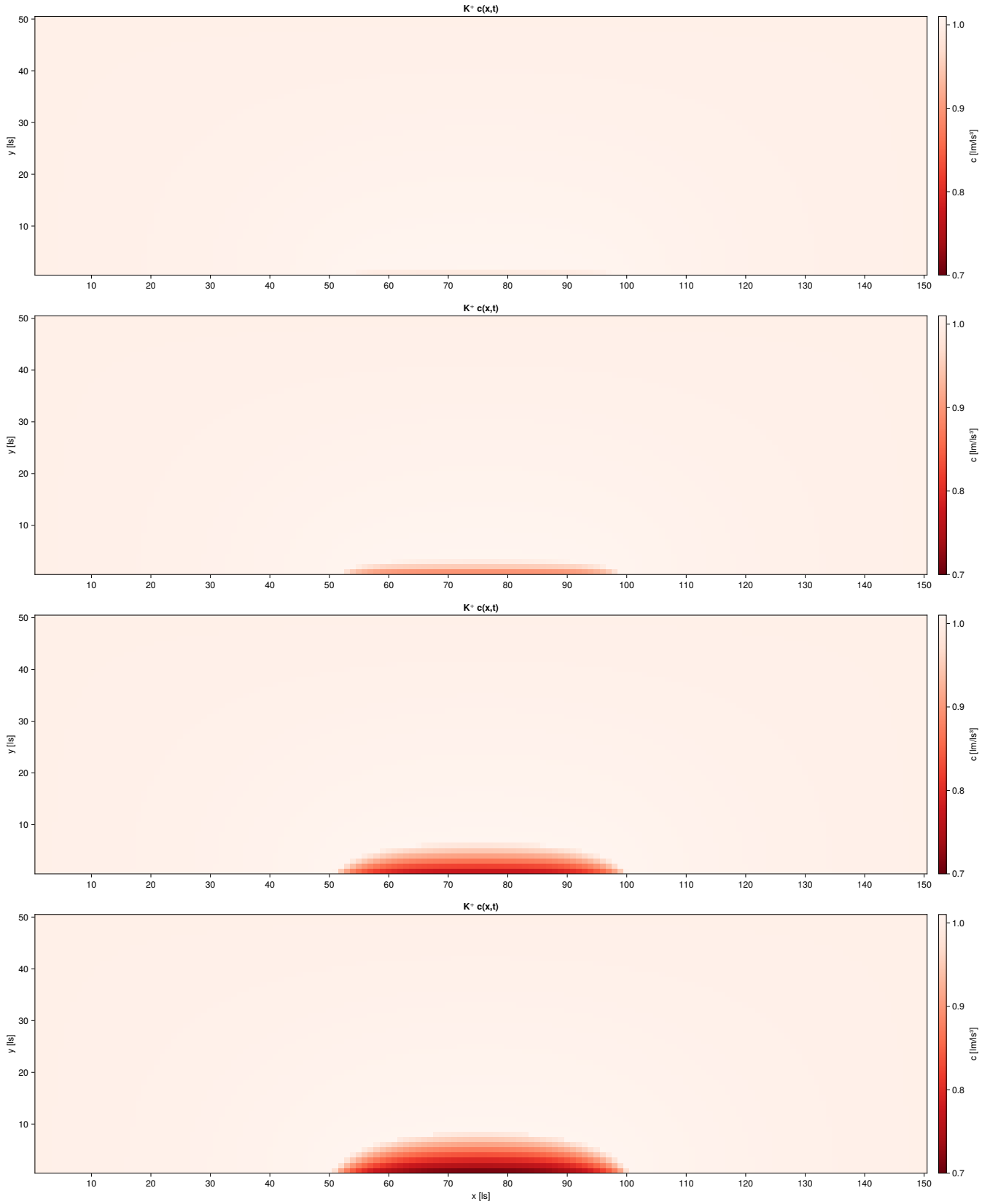


Figure 6.3: The evolution of the K^+ concentration c_{K^+} for times $t = 100\,\mu s, 1\,ms, 5\,ms$ and $10\,ms$.

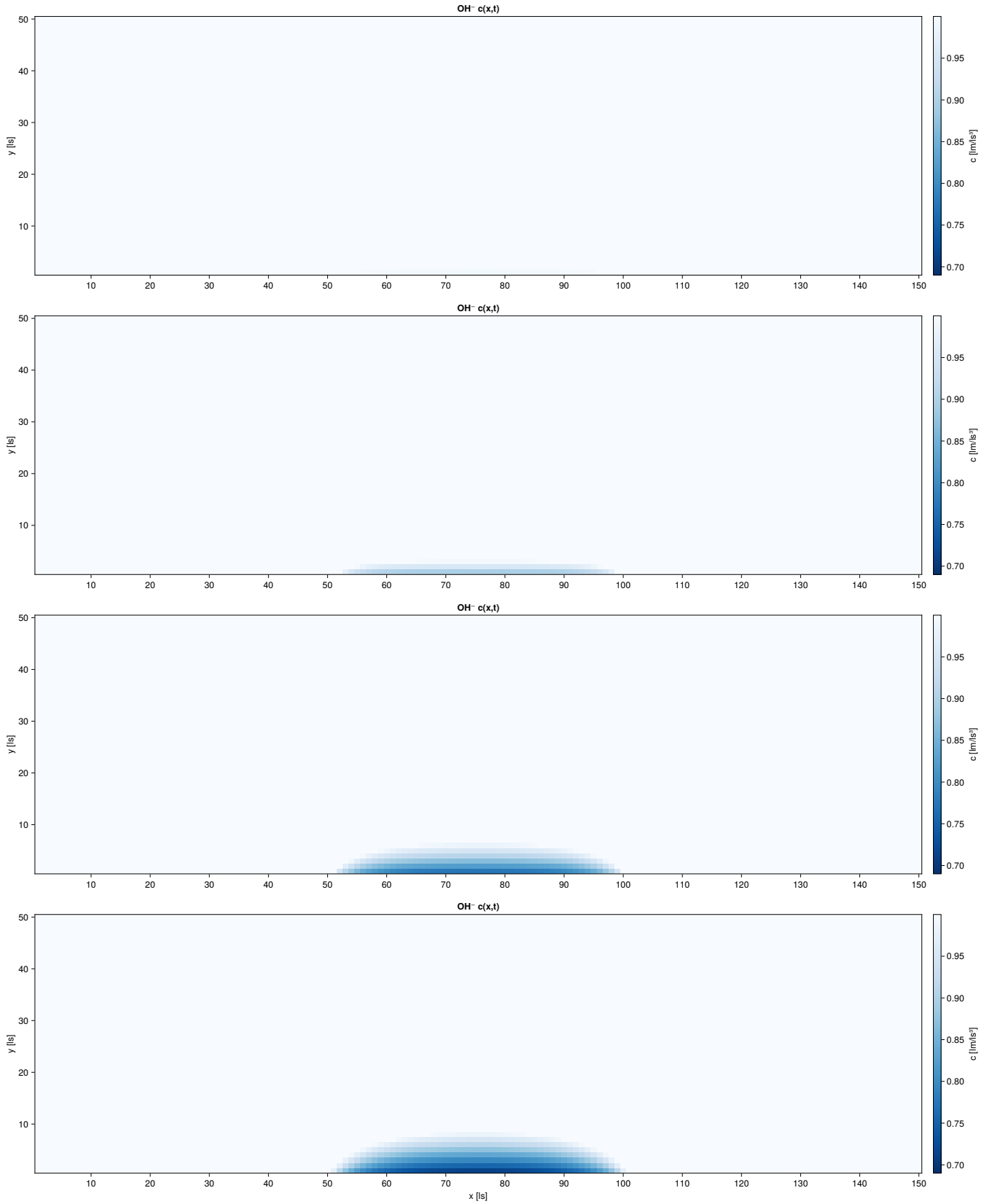


Figure 6.4: The evolution of the OH^- concentration c_{OH^-} for times $t = 100\,\mu s, 1\,ms, 5\,ms$ and $10\,ms$.

6.1
Precipitation Demonstration

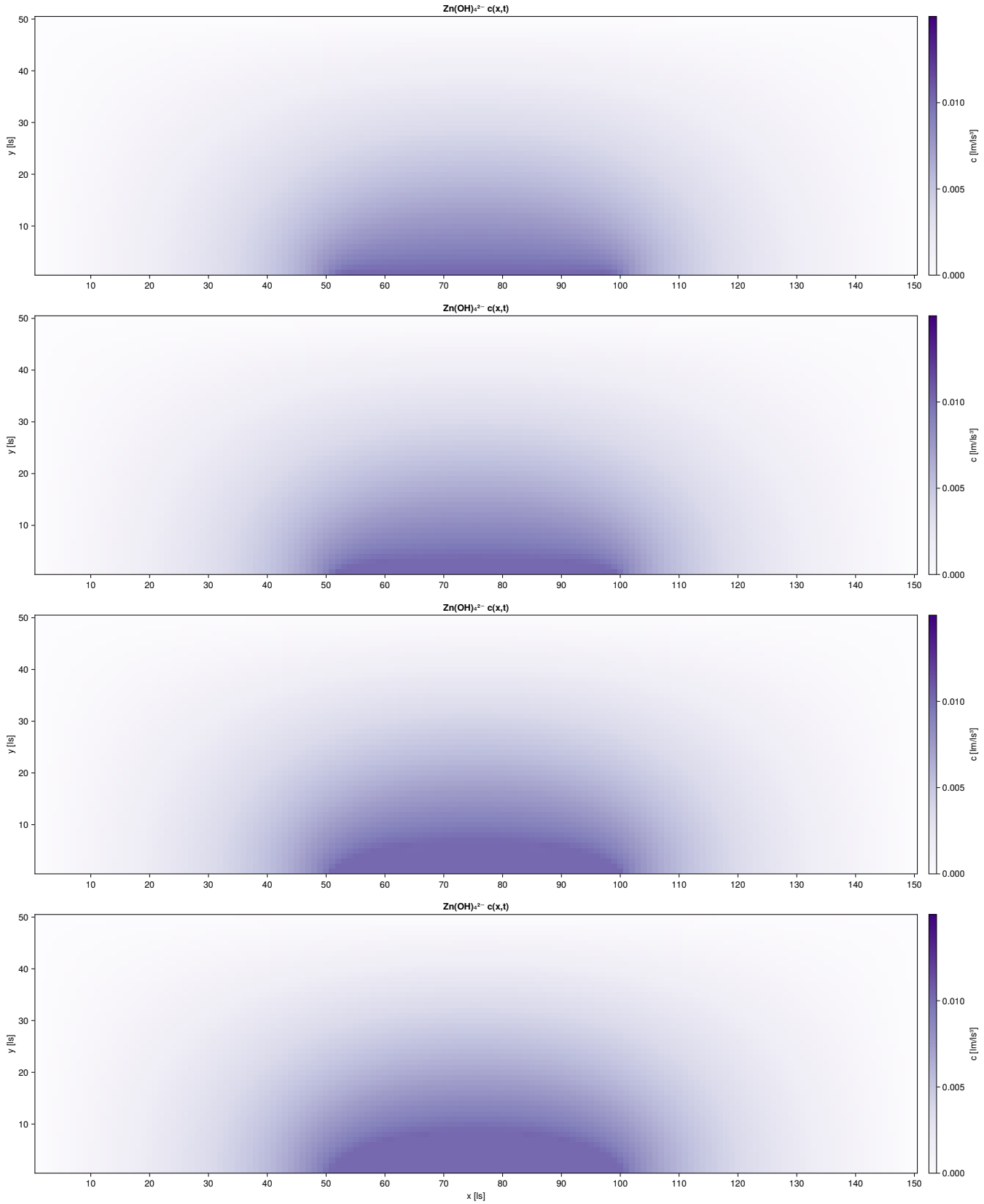


Figure 6.5: The evolution of the $Zn(OH)_4{}^{2-}$ concentration $c_{Zn(OH)_4{}^{2-}}$ for times $t = 100\,\mu s, 1\,ms, 5\,ms$ and $10\,ms$.

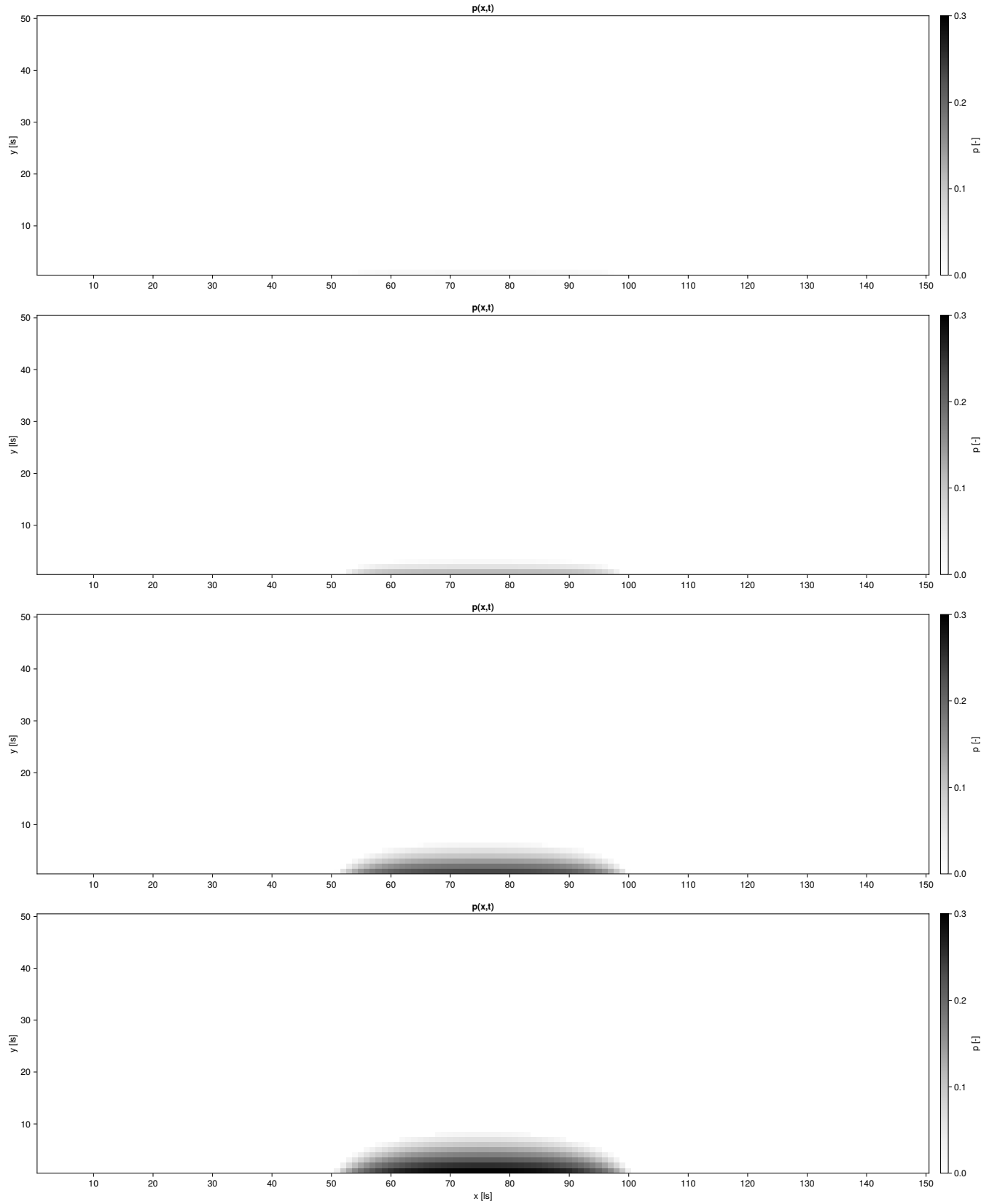


Figure 6.6: The evolution of the precipitation fraction p for times $t = 100\,\mu s, 1\,ms, 5\,ms$ and $10\,ms$.

6.1
Precipitation Demonstration

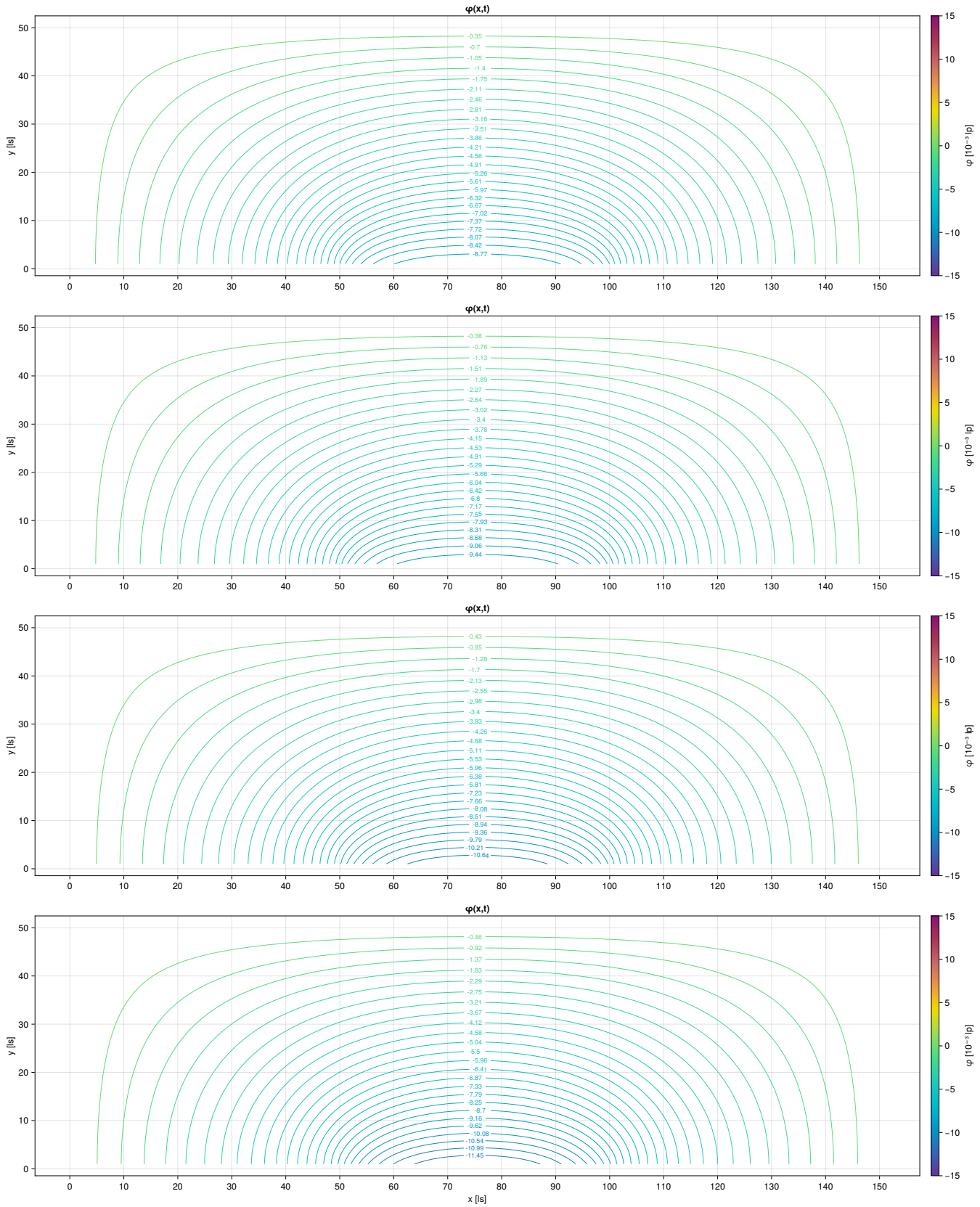


Figure 6.7: The evolution of the electric potential ϕ for times $t = 100\,\mu s, 1\,ms, 5\,ms$ and $10\,ms$.

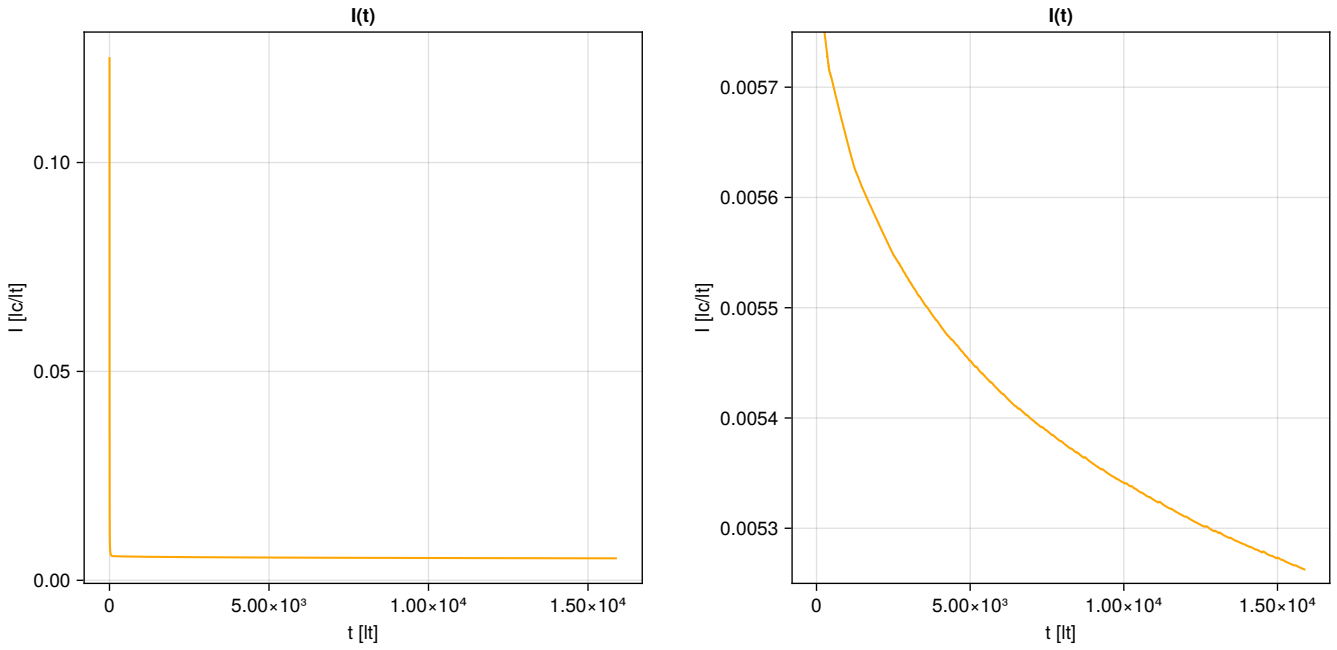


Figure 6.8: The evolution of the current I over time t. Initially, a sharp drop in concentration I is observed (left). When the current I has settled, we observe an exponential decline in I over time t (right).

The evolution of current I can be seen in Figure 6.8. The initial sharp drop in current I can be explained by the initial lack of $Zn(OH)_4{}^{2-}$ in the electrolyte, yielding a relatively high oxidation potential E_{ox} (see Equation 2.8 and Equation 2.9). This sharp drop in current I is then quickly followed up by exponential decline of the current I, caused by the precipitation forming at the anode. This limits the amount of OH^- able to reach the anode, limiting the amount of oxidation reactions able to take place, lowering the current density **J**.

6.2 External Electric Potential Demonstration

It is assumed that inside the beads, the zinc particle is neighboured by other zinc particles and carbon black strands. The simulations are ran again, now including the effects of the external electric potential ϕ_{ext} coming from these neighbouring charged components. The external electric potential ϕ_{ext} is assumed to be linear, centred on the middle of the domain Ω[xx], time-independent, and is held at an angle θ to the normal to the anode $\hat{\mathbf{n}}$ (see Figure 6.9):

$$\phi_{\text{ext}}(\mathbf{x}) = \phi_{\text{ext}}(x, y) = \phi_0 \left(\frac{x - l/2}{h} \cos\theta + \frac{y - h/2}{h} \sin\theta \right). \quad [6.3]$$

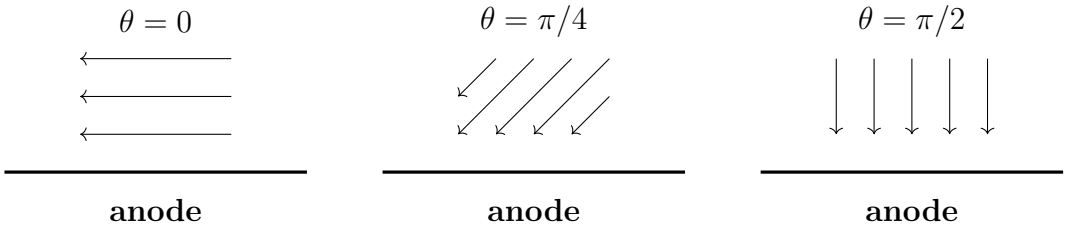


Figure 6.9: The direction of the external electric potential ϕ_{ext} relative to the anode for angles $\theta = 0$ (perpendicular), $\theta = \pi/4$ (diagonal) and $\theta = \pi/2$ (parallel).

The external electric potential ϕ_{ext} is then applied at the bulk boundaries Γ_{b} (see Table 6.3) To have the external electric potential ϕ_{ext} to be of similar magnitude as the electric potential ϕ, we take the static electric potential $\phi_0 = 0.01\,\text{lp}$ following from the previous precipitation demonstration.

Table 6.3: Caption.

Boundary	**Boundary Condition**	
	c_i	ϕ
Anode Γ_{a}	$\nabla_{\text{n}} c_i(\mathbf{x}_{\text{a}}, t) = -\frac{\mathbf{N}_i^{\text{ox}}(\mathbf{x}_{\text{a}}, t)}{D_i} - \frac{z_i F}{RT} c_i(\mathbf{x}_{\text{a}}, t) \nabla\phi(\mathbf{x}_{\text{a}}, t)$	$\nabla_{\text{n}}\phi(\mathbf{x}_{\text{a}}, t) = -\frac{\mathbf{J}(\mathbf{x}_{\text{a}}, t)}{\kappa(\mathbf{x}_{\text{a}}, t)}$
Bulk Γ_{b}	$c_i(\mathbf{x}_{\text{b}}, t) = c_{i,0}$	$\phi(\mathbf{x}_{\text{b}}, t) = \phi_{\text{ext}}(\mathbf{x}_{\text{b}})$
Carbon-black-alginate Γ_{c}	$\nabla_{\text{n}} c_i(\mathbf{x}_{\text{c}}, t) = \mathbf{0}$	$\nabla_{\text{n}}\phi(\mathbf{x}_{\text{c}}, t) = \mathbf{0}$

For the concentrations c_i and the precipitate fraction p, only slight differences to the precipitation demonstration were observed. Therefore, for the demonstration with the external electric potential ϕ_{ext}, the results are shown to emphasise on the difference in concentrations Δc_i and precipitation fraction Δp compared to the precipitation demonstration. They will not have their legend normalized, to better show the difference in concentrations Δc_i and precipitation fraction Δp at individual times t.

For all applied external electric potentials ϕ_{ext}, we observe slightly different evolutions of the concentrations c_i and the precipitate fraction p. The differences in concentrations Δc_i in the electrolyte are impacted by the external electric potentials ϕ_{ext}; the differences in concentrations Δc_i inside the precipitate are impacted mostly by the difference in the precipitation fraction Δp caused by the slight shift in how much precipitate forms. A negligible difference in the current ΔI was observed.

[xx]The lattice height h is taken to normalize the external electric potential ϕ_{x} over the domain Ω.

6.2.1 Perpendicular Electric Potential

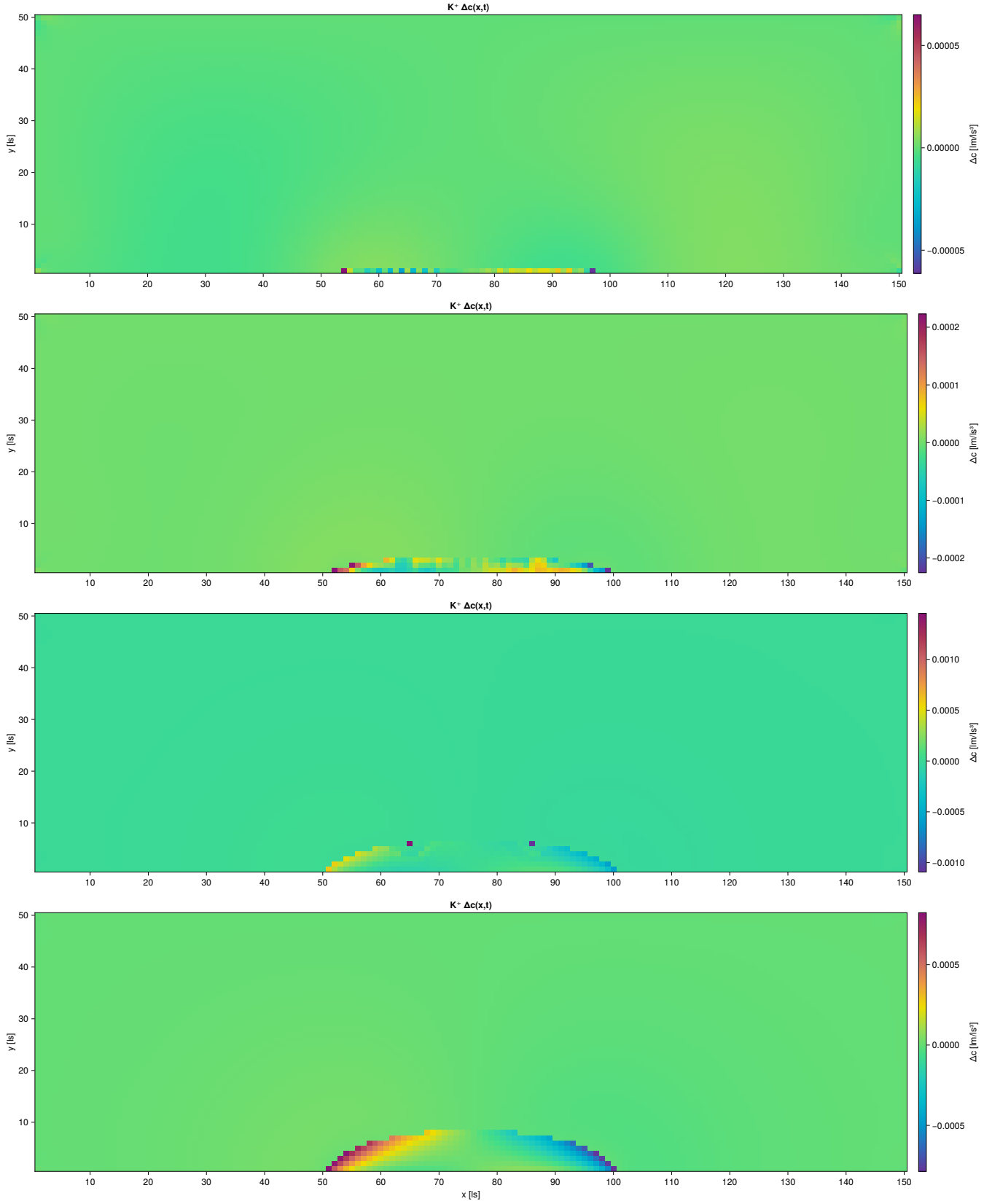


Figure 6.10: The evolution of the K^+ concentration c_{K^+} for times $t = 100\,\mu s, 1\,ms, 5\,ms$ and $10\,ms$ relative to Figure 6.3, where an external electric potential ϕ_{ext} is applied at an angle $\theta = 0$ (perpendicular).

6.2
External Electric Potential Demonstration

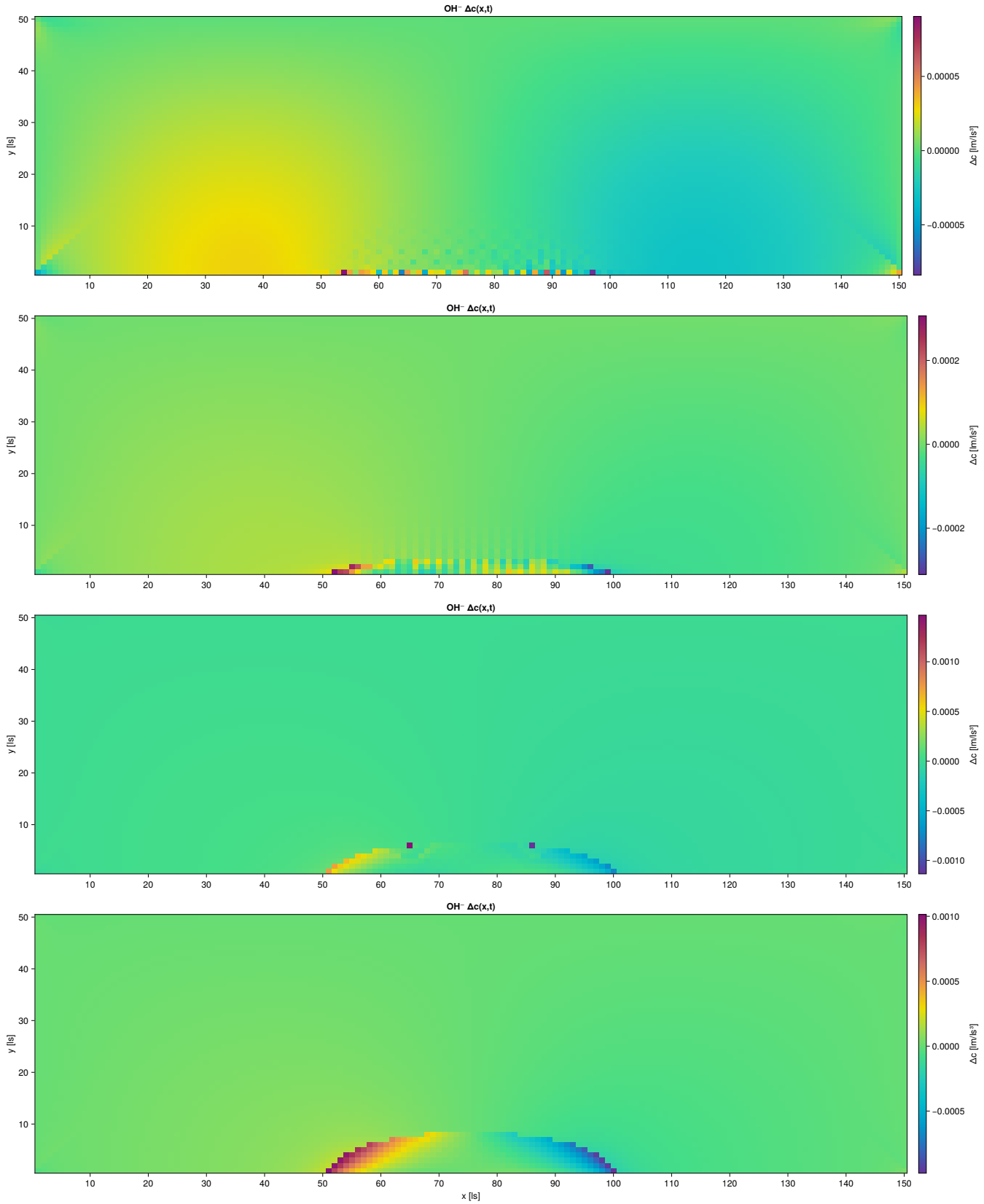


Figure 6.11: The evolution of the OH^- concentration c_{OH^-} for times $t = 100\,\mu s, 1\,ms, 5\,ms$ and $10\,ms$ relative to Figure 6.4, where an external electric potential ϕ_{ext} is applied at an angle $\theta = 0$ (perpendicular).

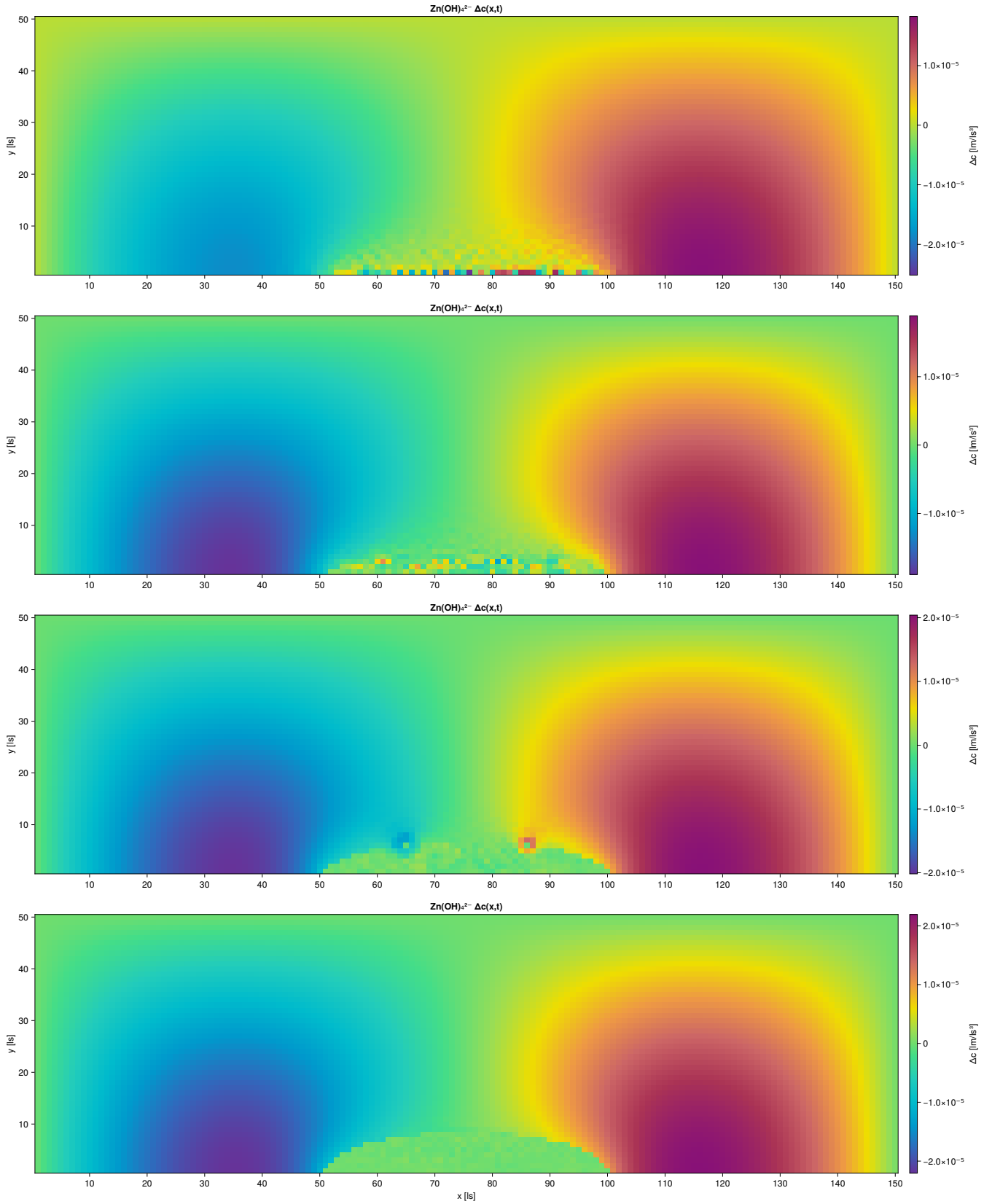


Figure 6.12: The evolution of the $Zn(OH)_4{}^{2-}$ concentration $c_{Zn(OH)_4{}^{2-}}$ for times $t = 100\,\mu s, 1\,ms, 5\,ms$ and $10\,ms$ relative to Figure 6.5, where an external electric potential ϕ_{ext} is applied at an angle $\theta = 0$ (perpendicular).



Figure 6.13: The evolution of the precipitation fraction p for times $t = 100\,\mu s, 1\,ms, 5\,ms$ and $10\,ms$ relative to Figure 6.6, where an external electric potential ϕ_{ext} is applied at an angle $\theta = 0$ (perpendicular).

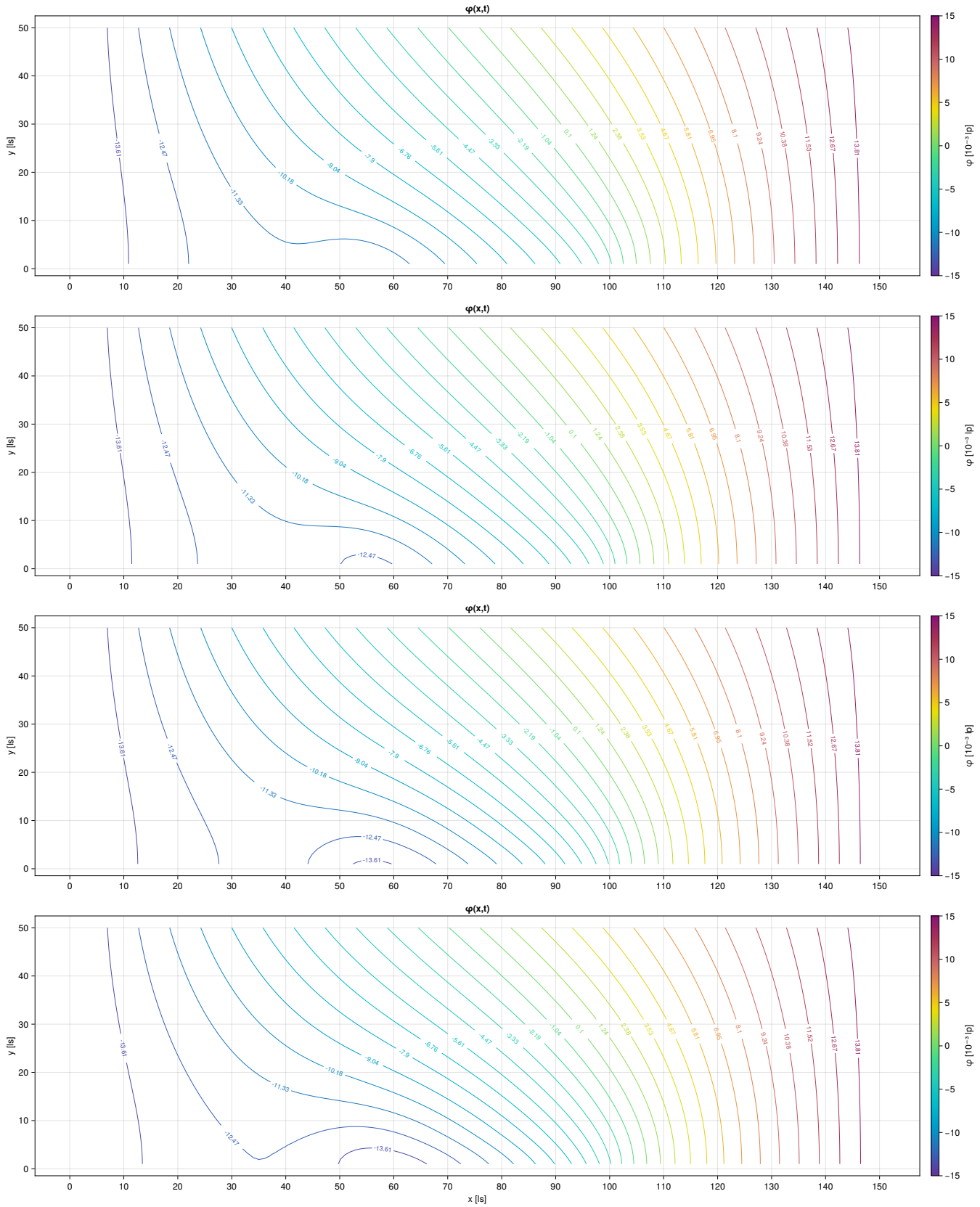


Figure 6.14: The evolution of the electric potential ϕ for times $t = 100\,\mu s, 1\,ms, 5\,ms$ and $10\,ms$, where an external electric potential ϕ_{ext} is applied at an angle $\theta = 0$ (perpendicular).

6.2.2 Diagonal Electric Potential

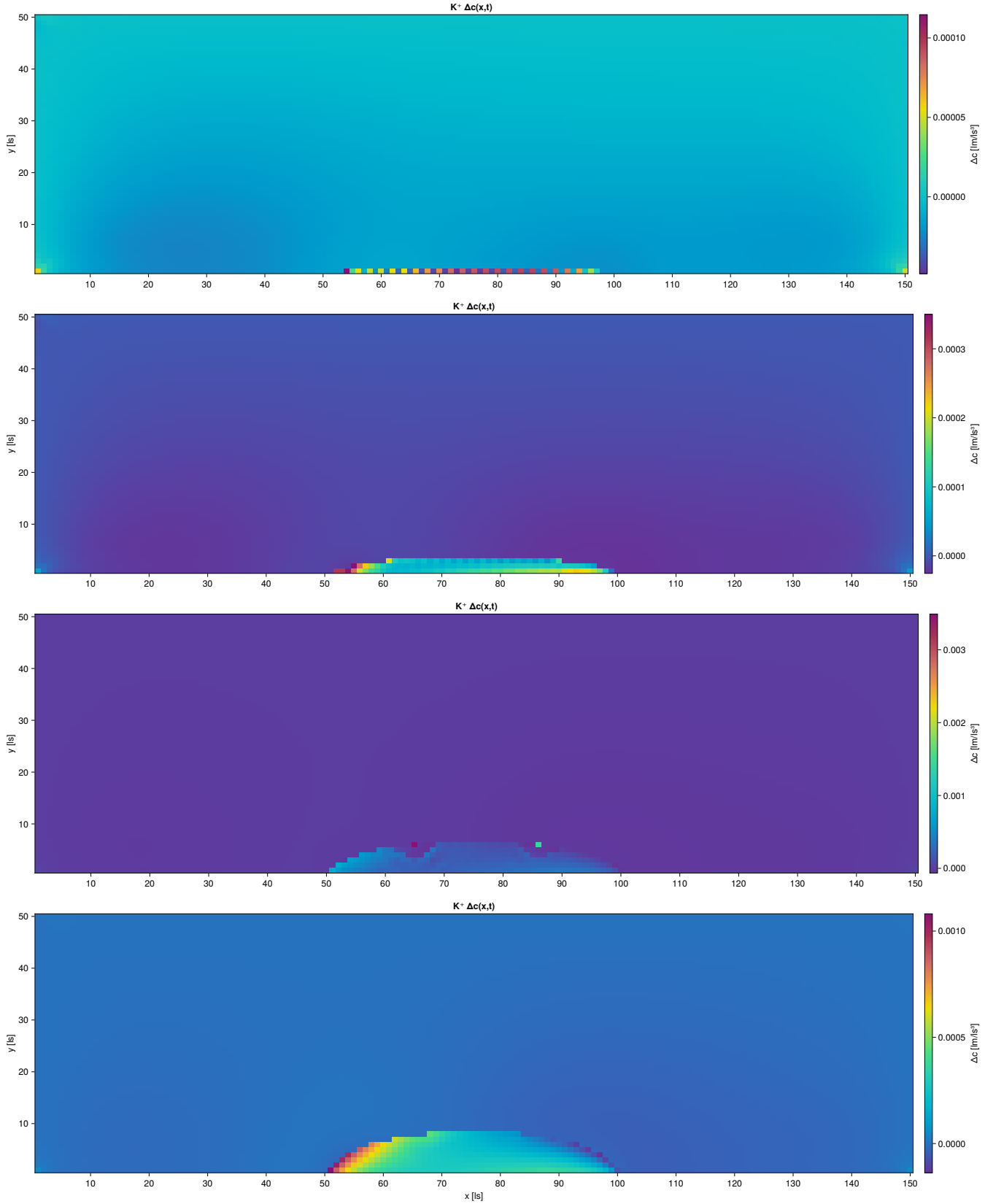


Figure 6.15: The evolution of the K^+ concentration c_{K^+} for times $t = 100\,\mu s, 1\,ms, 5\,ms$ and $10\,ms$ relative to Figure 6.3, where an external electric potential ϕ_{ext} is applied at an angle $\theta = \pi/4$ (diagonal).

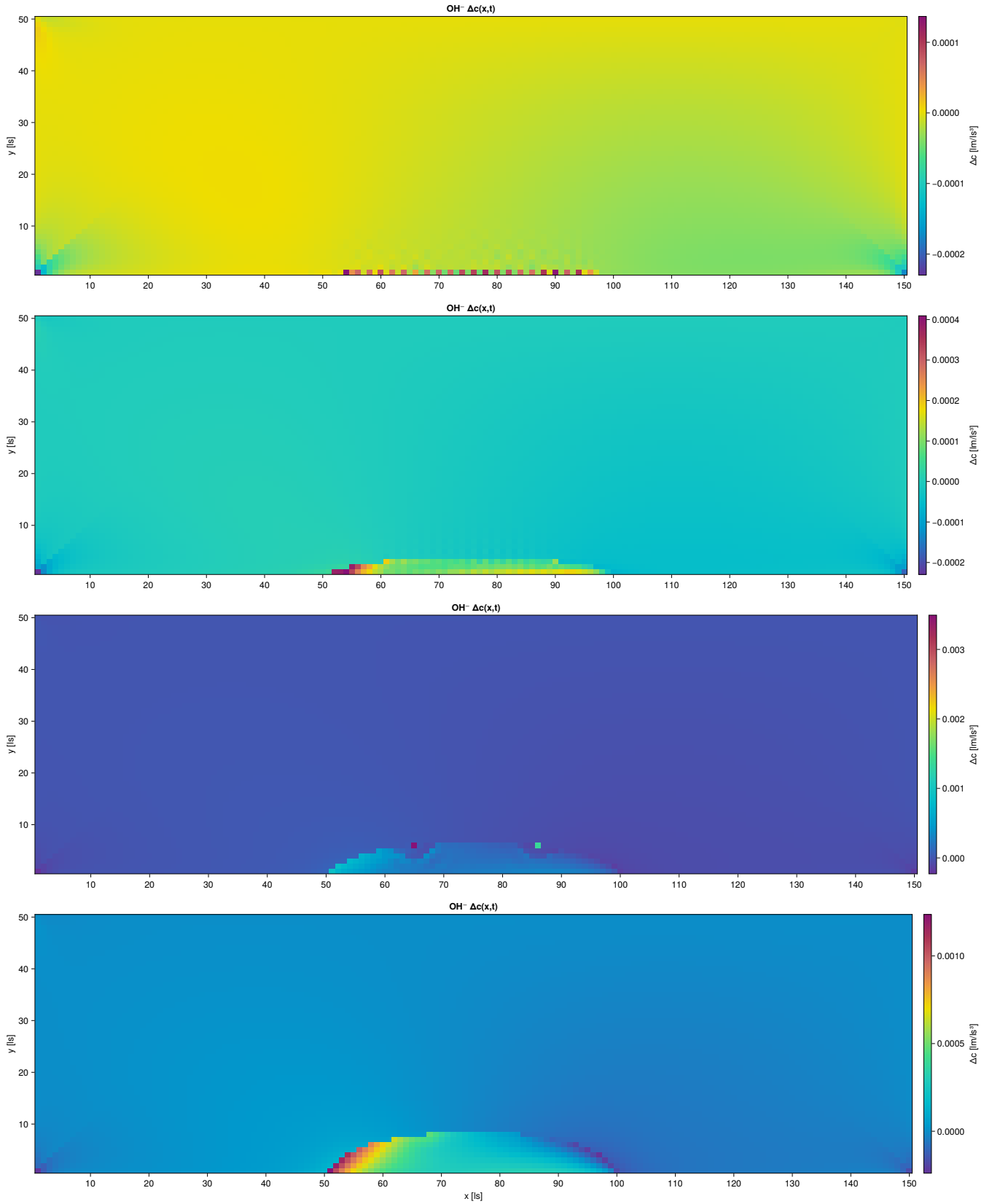


Figure 6.16: The evolution of the OH^- concentration c_{OH^-} for times $t = 100\,\mu s, 1\,ms, 5\,ms$ and $10\,ms$ relative to Figure 6.4, where an external electric potential ϕ_{ext} is applied at an angle $\theta = \pi/4$ (diagonal).

6.2
External Electric Potential Demonstration

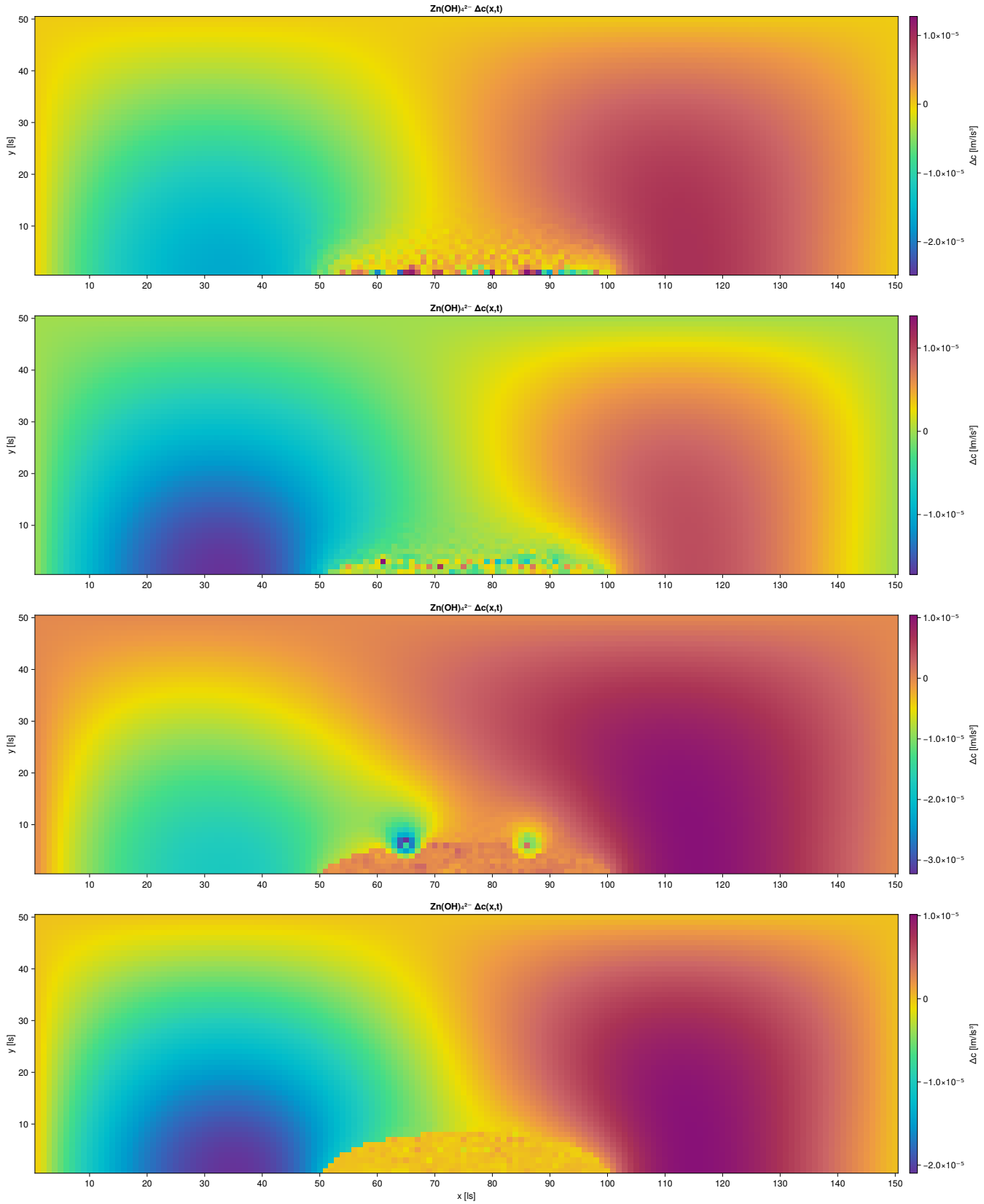


Figure 6.17: The evolution of the $Zn(OH)_4{}^{2-}$ concentration $c_{Zn(OH)_4{}^{2-}}$ for times $t = 100\,\mu s, 1\,ms, 5\,ms$ and $10\,ms$ relative to Figure 6.5, where an external electric potential ϕ_{ext} is applied at an angle $\theta = \pi/4$ (diagonal).

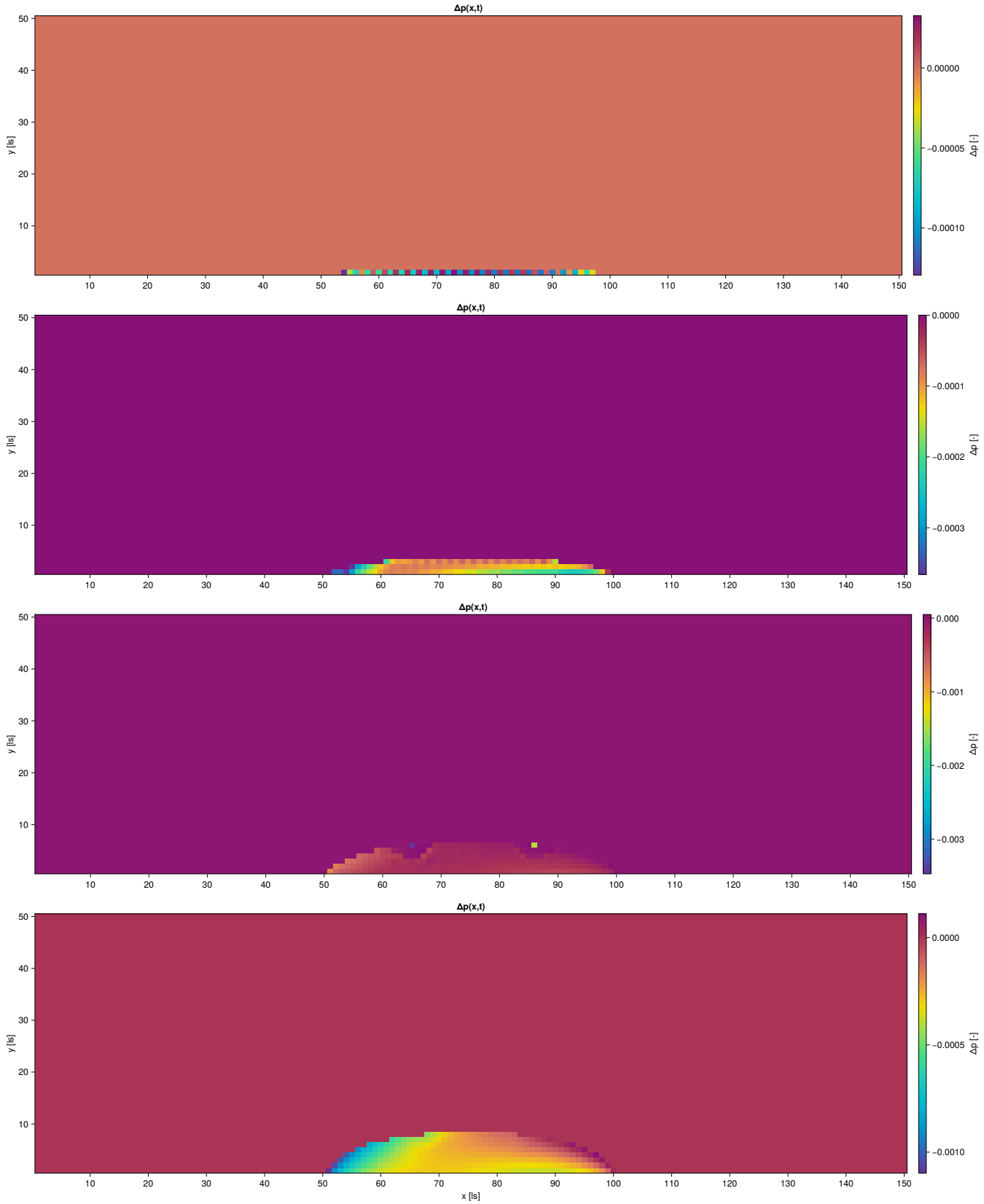


Figure 6.18: The evolution of the precipitation fraction p for times $t = 100\,\mu s, 1\,ms, 5\,ms$ and $10\,ms$ relative to Figure 6.6, where an external electric potential ϕ_{ext} is applied at an angle $\theta = \pi/4$ (diagonal).

6.2
External Electric Potential Demonstration

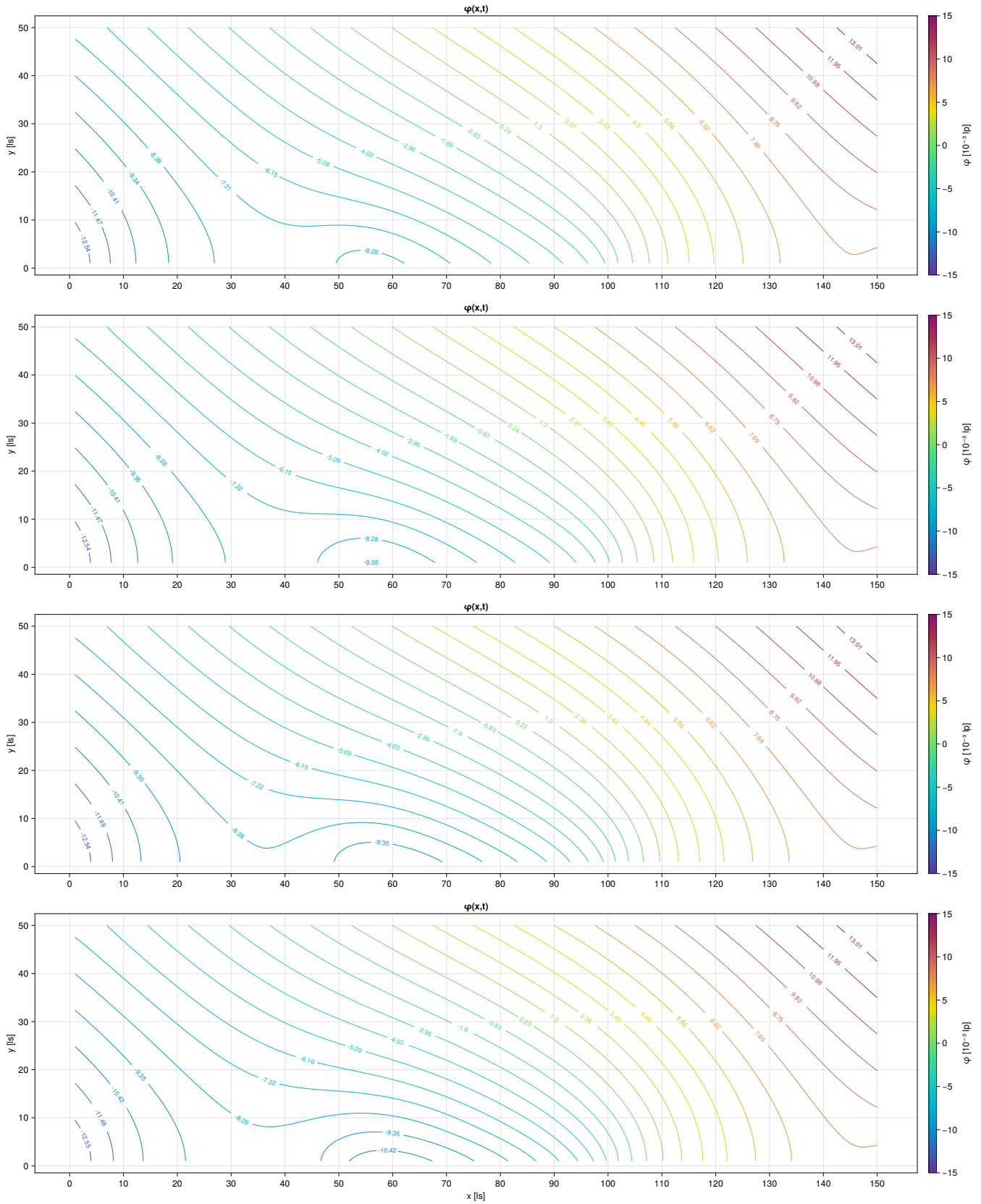


Figure 6.19: The evolution of the electric potential ϕ for times $t = 100\,\mu s, 1\,ms, 5\,ms$ and $10\,ms$, where an external electric potential ϕ_{ext} is applied at an angle $\theta = \pi/4$ (diagonal).

6.2.3 Parallel Electric Potential

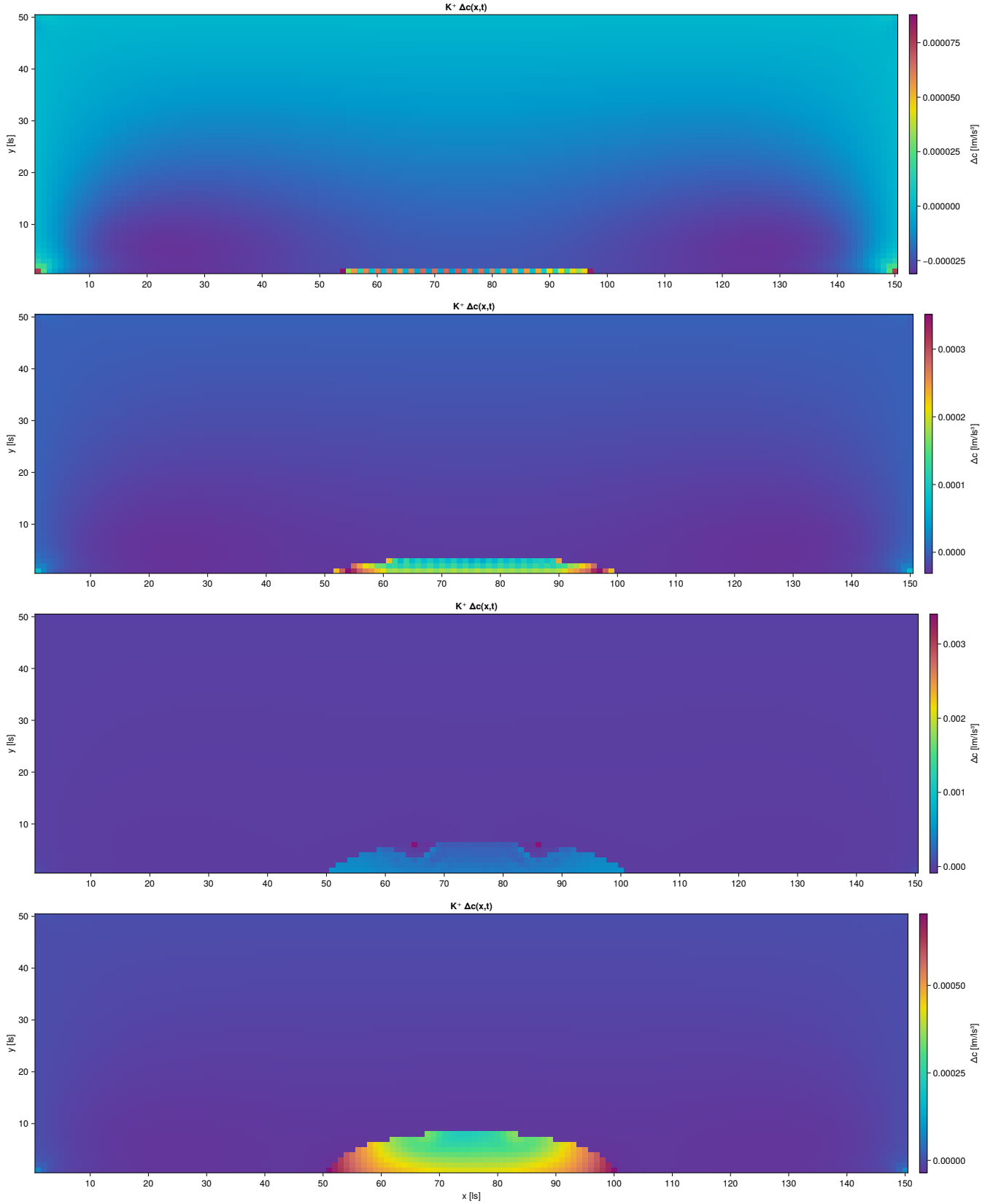


Figure 6.20: The evolution of the K^+ concentration c_{K^+} for times $t = 100\,\mu s, 1\,ms, 5\,ms$ and $10\,ms$ relative to Figure 6.3, where an external electric potential ϕ_{ext} is applied at an angle $\theta = \pi/2$ (parallel).

6.2
External Electric Potential Demonstration

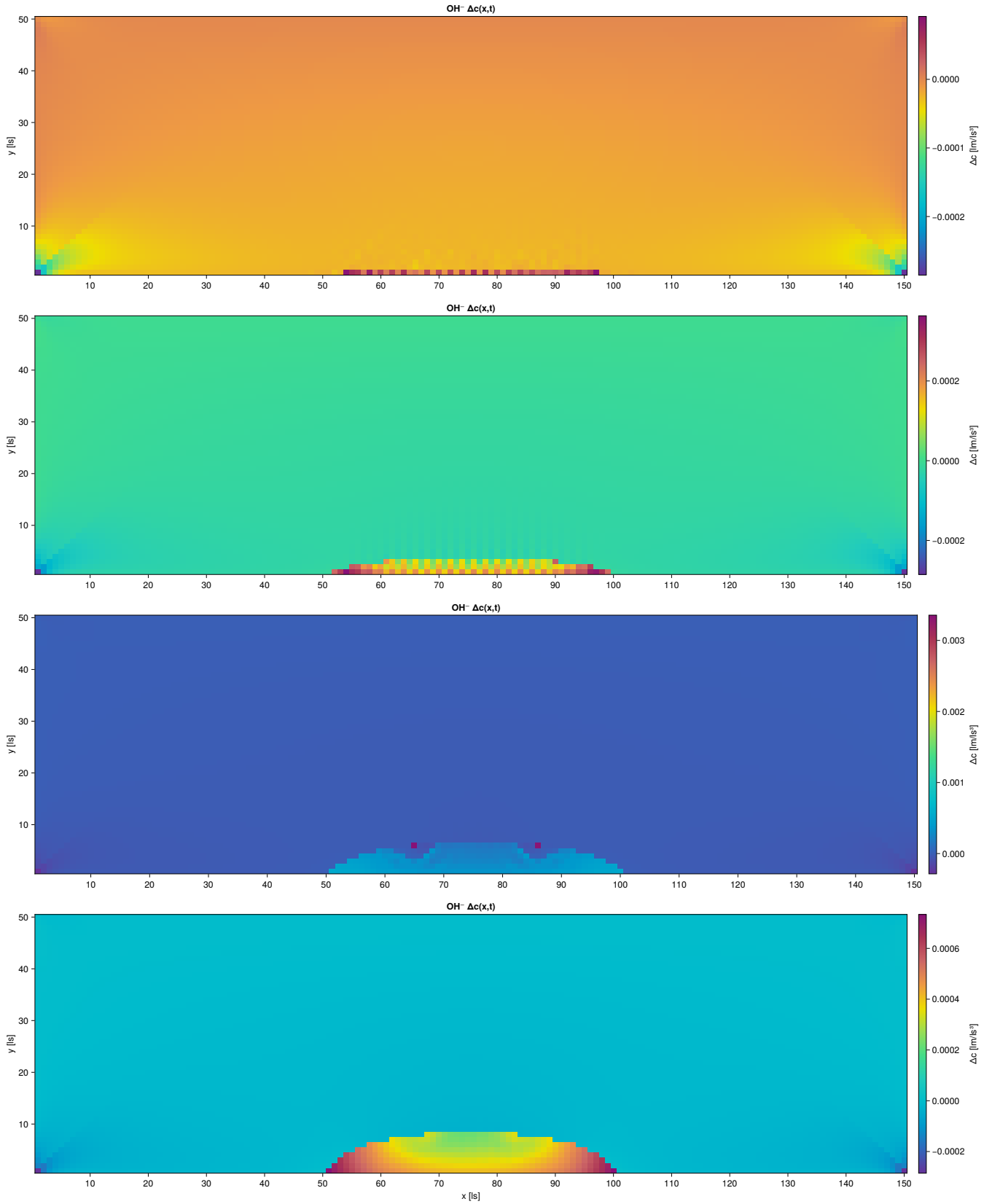


Figure 6.21: The evolution of the OH^- concentration c_{OH^-} for times $t = 100\,\mu s, 1\,ms, 5\,ms$ and $10\,ms$ relative to Figure 6.4, where an external electric potential ϕ_{ext} is applied at an angle $\theta = \pi/2$ (parallel).

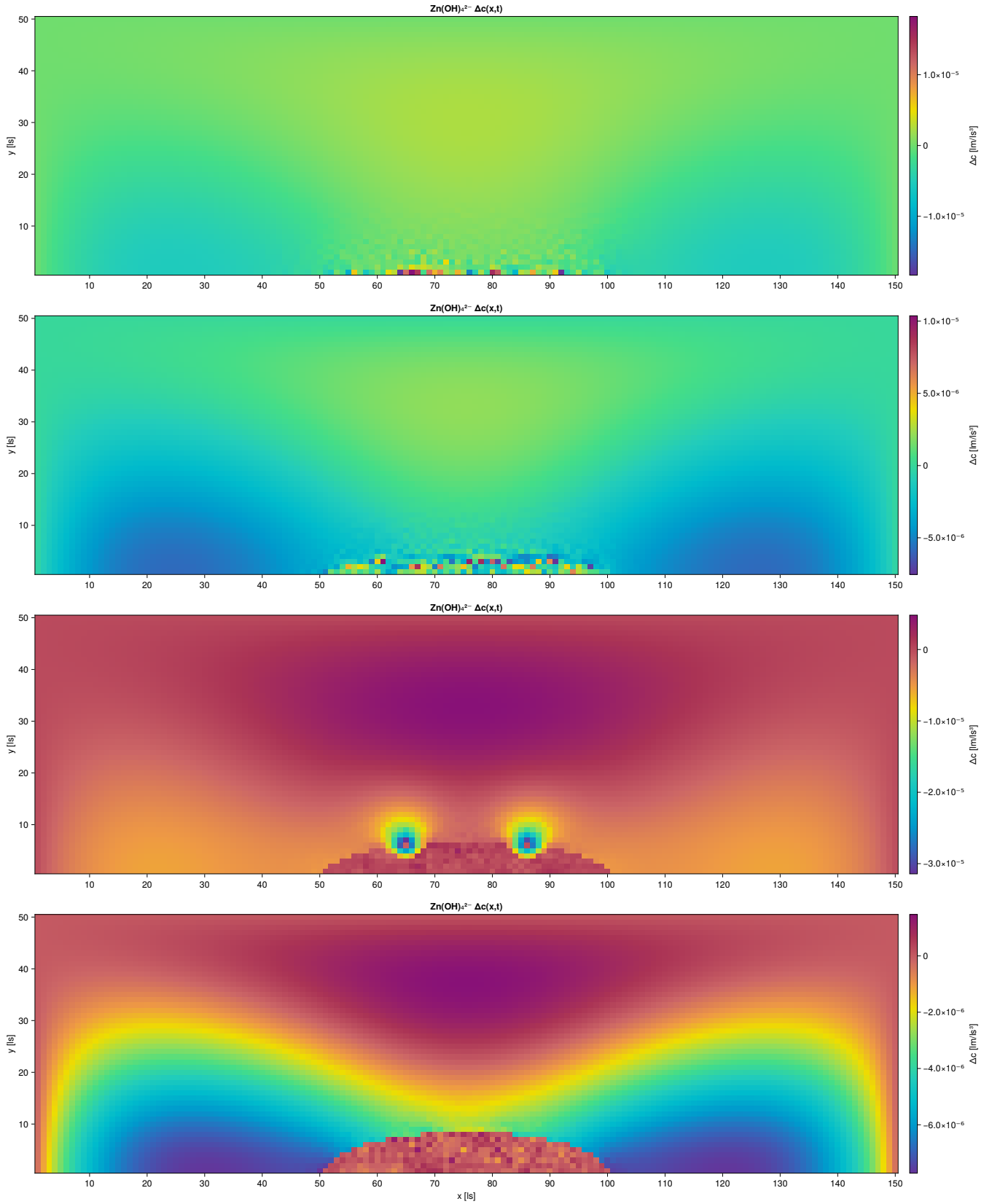


Figure 6.22: The evolution of the $Zn(OH)_4{}^{2-}$ concentration $c_{Zn(OH)_4{}^{2-}}$ for times $t = 100\,\mu s, 1\,ms, 5\,ms$ and $10\,ms$ relative to Figure 6.5, where an external electric potential ϕ_{ext} is applied at an angle $\theta = \pi/2$ (parallel).

6.2
External Electric Potential Demonstration

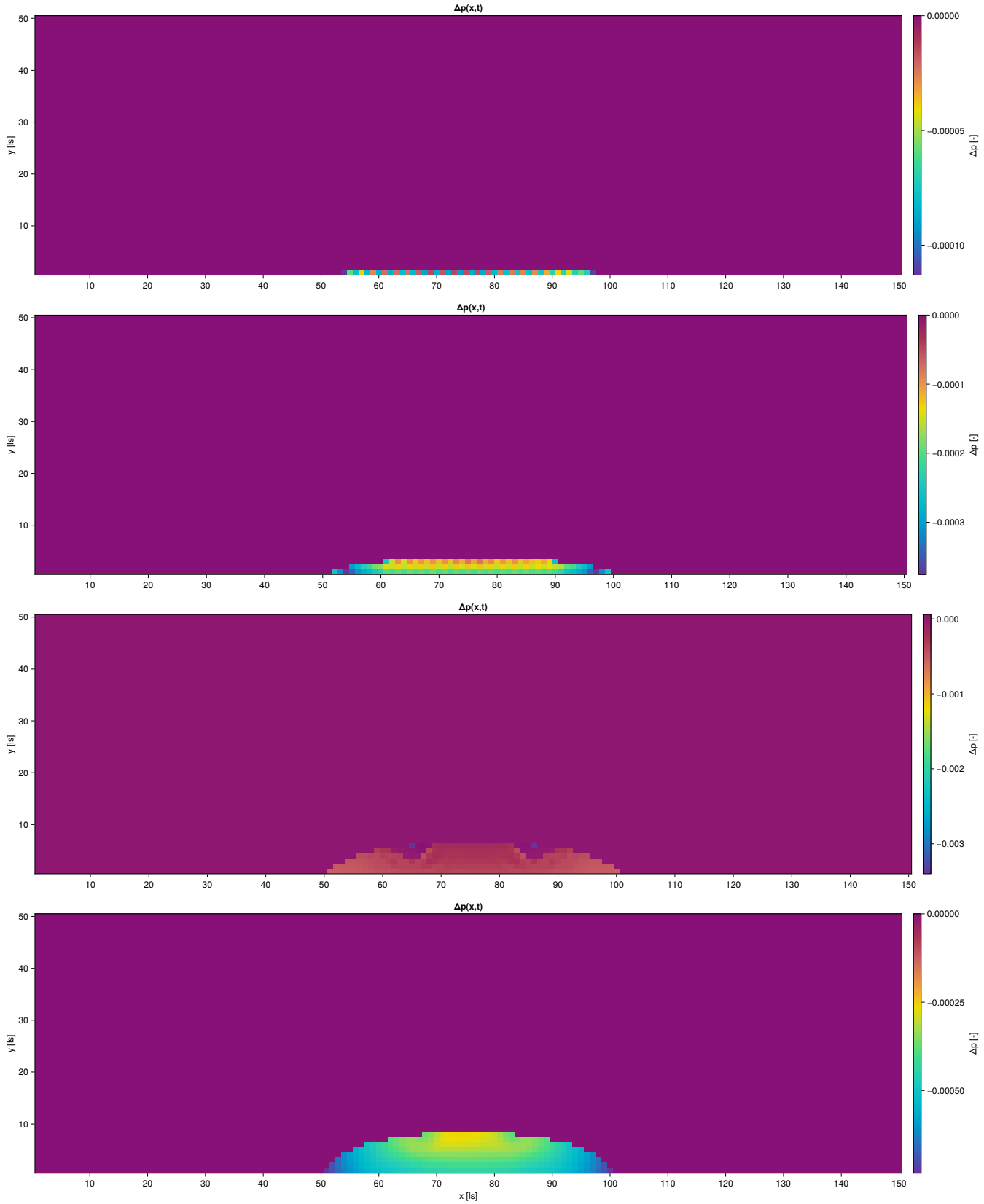


Figure 6.23: The evolution of the precipitation fraction p for times $t = 100\,\mu s, 1\,ms, 5\,ms$ and $10\,ms$ relative to Figure 6.6, where an external electric potential ϕ_{ext} is applied at an angle $\theta = \pi/2$ (parallel).

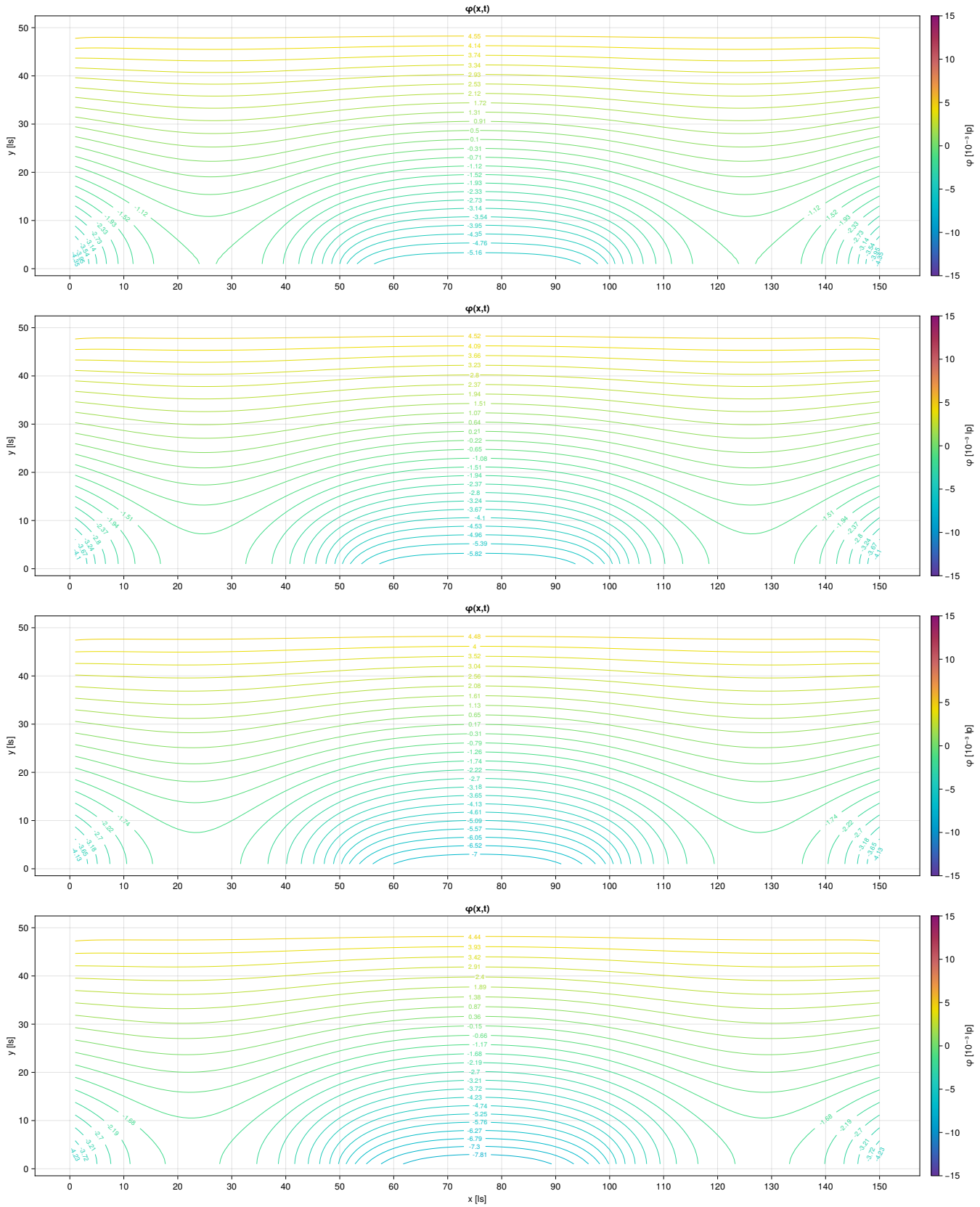


Figure 6.24: The evolution of the electric potential ϕ for times $t = 100\,\mu s, 1\,ms, 5\,ms$ and $10\,ms$, where an external electric potential ϕ_{ext} is applied at an angle $\theta = \pi/2$ (parallel).

7 Discussion

7.1 Validation and Practicality 71
7.1.1 Resolution Limitations 71
7.1.2 Analytical Conformity 71
7.1.3 COMSOL Discrepancy 71
7.1.4 Precipitation Evolution 72
7.2 Further Research 72
7.2.1 Relaxation Time Dependency 72
7.2.2 Experimental Verification 72
7.2.3 Mediator Molecule Precipitation 72
7.2.4 Precipitation Methodology 73
7.2.5 GPU Acceleration 73

After the benchmarking has yielded demonstrations of the simulation, the outcomes of the simulation are now discussed, together with recommendations on further research.

7.1 Validation and Practicality

7.1.1 Resolution Limitations

The choice of pH = 11 and therefore a bulk concentration of $c_0 = 1\,\mathrm{mol\,m^{-3}}$ pushes the limits of the "mesoscale" definition made in Subsubsection 3.1.1, as the bulk concentration c_0 impacts the Debye length λ and therefore the lattice spacing Δx (see Subsubsection 4.2.3). This has restricted the simulations ran in this thesis to a relatively tiny lattice spacing Δx to still correctly model the EDL. Simulations using the methods laid out in this thesis with a larger lattice spacing Δx are therefore more physically justified.

7.1.2 Analytical Conformity

From the analytical benchmarks (see Subsection 5.2), we observe that the LBM simulation is in agreement with the steady-state behaviour which is given by Gouy-Chapman theory, with deviations given through the RMSE in the range of 10^{-3} $\mathrm{lm\,ls^{-3}}$ and 10^{-3} lp for the $c_i(t)$-LBM and the $\phi(s)$-LBM respectively. These deviations (in the order of 0.1%) for the RMSE are relatively low, showing how the simulation is able to remain stable and yield accurate results.[23]

7.1.3 COMSOL Discrepancy

Running the LBM simulation next to a COMSOL simulation reveals clear differences in their steady-state behaviour (see Subsection 5.3). This is the case, most likely because of the different methods used for computing the electric potential ϕ, where the LBM simulation uses the pseudo-steady-state solution for the pseudo-transient Poisson equation, and the COMSOL simulation uses FEM to calculate for electro-neutrality. It might be argued that the LBM simulation and COMSOL simulation can not be compared one-for-one, although they do still share similar behaviour when approaching steady-state.[31,36]

7.1.4 Precipitation Evolution

From the precipitation demonstration (see Subsection 6.1), we observe a layer of precipitate forming on the anodic boundary Γ_a. The precipitate forms a spherical shell on top of the anode (see Figure 6.6), impeding the transport of OH^- reaching the anodic boundary Γ_a and therefore impacting the formation of $Zn(OH)_4{}^{2-}$. This causes less ZnO to precipitate, slowing down the growth of the precipitate fraction p. This behaviour is confirmed by the evolution of the current I (see Figure 6.8), which decays exponentially as time passes, indicating that less oxidation is taking place at the anodic boundary Γ_a.

From the external electric potential demonstrations (see Subsection 6.2), we observe how the external electric potential ϕ_{ext} has a minimal influence on the concentrations c_i and the precipitate fraction p, even though it impacts the electric potential ϕ greatly. The impact it did have, which affected the demonstration for every θ tried, shifted the precipitate fraction p of the precipitate, where more/less precipitate would form depending on the angle θ of the external electric potential ϕ_{ext} (see Figure 6.13, Figure 6.18 and Figure 6.23). Still, it can be argued that one can safely simulate only the effects of one zinc particle to make comments about the efficacy of the bead as a whole, as the differences in concentration Δc_i and precipitate fraction Δp are multiple orders of magnitude lower than their references.

The "checker board" pattern observed in some of the concentrations c_i and precipitate fraction p figures in Subsection 6.2 can be accounted for as numerical instabilities, which seem to disappear as the simulation runs for a longer time t.[37]

7.2 Further Research

This model can be expanded to the needs of any electrochemical problem obeying the PNP-equations, some suggestions for which are given below.

7.2.1 Relaxation Time Dependency

The RMSE of the simulation appears to be highly dependent on the relaxation time τ_i and relaxation pseudo-time σ used (see Section 5) — these effects can be mitigated by using an approach different than the BGK operator, such as a multiple relaxation time approach.[23,38]

7.2.2 Experimental Verification

The aim of this thesis was to make a "digital twin" to a ZRMFB. Although other student projects ran alongside this one who were developing a ZRMFB, no experimental results have been compared to this model. This model has only been verified analytically — a continuation of this project could include the verification to real experiments ran. This does not have to pertain to comparisons to ZRMFBs, as the simulation can be adapted to simulate any species i, oxidation/reduction reactions, and precipitation in an electrolyte.[15]

7.2.3 Mediator Molecule Precipitation

It is assumed that mediator molecules present in the electrolyte of the ZRMFB are too large to enter the porous beads. In test ran on ZRMFB, however, it was observed that the mediator molecules used could enter the beads, and even react with the zinc and potassium before it could react into zincate. This has not been modelled in this thesis, as this result was unexpected and deemed as unwanted behaviour.

7.2.4 Precipitation Methodology

The method used to implement precipitation into the simulation (see Subsubsection 2.2.2) through the Precipitation Solver allows for the formation of zinc oxide as layers covering the anode. As this was observed experimentally, this method sufficed. Precipitation in batteries commonly forms dendrites, forming fractal-like crystals on the anode. Dendritic growth has been modelled through the LBM before by assigning nucleation sites to the anode, and applying a phase-field model on the simulation as an additional LBM model running after the $c_i(t)$-LBM. This third LBM model then calculates the position-dependent likelihood of precipitate forming on pre-existing precipitate, allowing for the formation of dendrites.[32,33]

7.2.5 GPU Acceleration

The simulation is written in Julia, and is ran only on the CPU, where no parallel computing is implemented. The simulation ran in this thesis took in the order of seconds (for the benchmarks in Section 5) to multiple hours (for the precipitation demonstrations in Section 6). GPU-accelerated parallel computing could be implemented to combat the long running times of the simulation. If this model were to be expanded upon (additional species i, larger domain Ω, longer simulation times t_{sim}), this needs to be considered to decrease computational time.[39]

8 Conclusion

A simulation was created to simulate the reaction-precipitation phenomena which take place inside the beads of a ZRMFB. The coupled Poisson-Nernst-Planck equations, which govern the evolution of the concentrations c_i and electric potential ϕ, were recast through the Lattice Boltzmann Method. The discretization of the equations rely on kinetic theory and kinetic pseudo-theory, the latter of which was derived in this thesis through introducing the pseudo-diffusivity χ as a function of the permittivity ϵ and a scaling factor γ. This approach allowed us to model the Poisson equation as a pseudo-transient equation and use it in the LBM. The simulation consists of the $c_i(t)$-LBM model to iterate the concentrations c_i over time t, the $\phi(s)$-LBM model to iterate the electric potential ϕ over pseudo-time s, together with the Electrostatics, Electrokinetics, Migrative Velocity and Precipitation Solvers to compute macroscopic variables.

The LBM simulation was then able to simulate the evolution of concentrations c_i and electric potential ϕ conform with steady-state analytical solutions given through Gouy-Chapman theory. The LBM simulation yielded similar behaviour to a COMSOL simulation under matching circumstances, but did not yield the same steady-state behaviour — this has been explained through the inherent different methods used by the simulations, as COMSOL uses both a different computation method (FEM vs. LBM) and different methodology for computing the electric potential ϕ (by assuming electro-neutrality instead of calculating the electric potential ϕ through the Poisson equation).

The LBM simulation was then applied to simulate the reaction-precipitation phenomena. The evolution of the growth of the precipitate on the anodic boundary Γ_{a} was observed to form a spherical shell, impeding the oxidation reaction and therefore lowering the current I exponentially over time. Under the effects of an external electric potential ϕ_{ext}, the precipitate fraction p takes on marginally different values compared to there not being an external electric potential ϕ_{ext}, suggesting that each zinc particle can be modelled as a separate anode in the bead.

A Appendix

A.1 On the Process of Non-Dimensionalization 75
A.2 Effects of the Relaxation (Pseudo-)time on the (Pseudo-)Steady-State Solutions 75

A.1 On the Process of Non-Dimensionalization

The unit conversion factors defined in Subsection 4.1 have their derivations based on allowing the unit they represent to be defined on their characteristic value. For the charged ions, this means that populations move across 1 ls in 1 lt, where a concentration c_i of $1\,\mathrm{lm\,ls^{-3}}$ carries with it one 1 lc. Through making the equations dimensionless through the variable conversion factors $\mathcal{V}$ (see Equation 4.8), we observe the following:

- all mentions of the lattice spacing Δx and lattice time Δt drop out, as they equal unity;
- all equations regarding electric potential ϕ have the F/RT-fraction drop out, as it is contained in the definition of the lattice potential through the potential conversion factor $\mathcal{P}$
- all equations regarding charge have Faraday's constant F drop out, as it is contained in the definition of the lattice charge through the charge conversion factor $\mathcal{C}$.

A.2 Effects of the Relaxation (Pseudo-)time on the (Pseudo-)Steady-State Solutions

As previously established, the relaxation time τ_i and relaxation pseudo-time σ affect the (pseudo)-steady-state solution of the $c_i(t)$-LBM and $\phi(s)$-LBM models (see Section 5), where the concentration c_i or electric potential ϕ can either under- or overshoot the analytical solution. This behaviour can be seen in Figure A.1, Figure A.2, and Figure A.3.

Interestingly, the p^+ concentration c_+ seems to be impacted more by a change in relaxation time τ_i than then$^-$ concentration c_-. The electric potential ϕ also seems to be impacted significantly by a change in relaxation pseudo-time σ. It are these under- and overshoots that raise the RSME for the models ran.

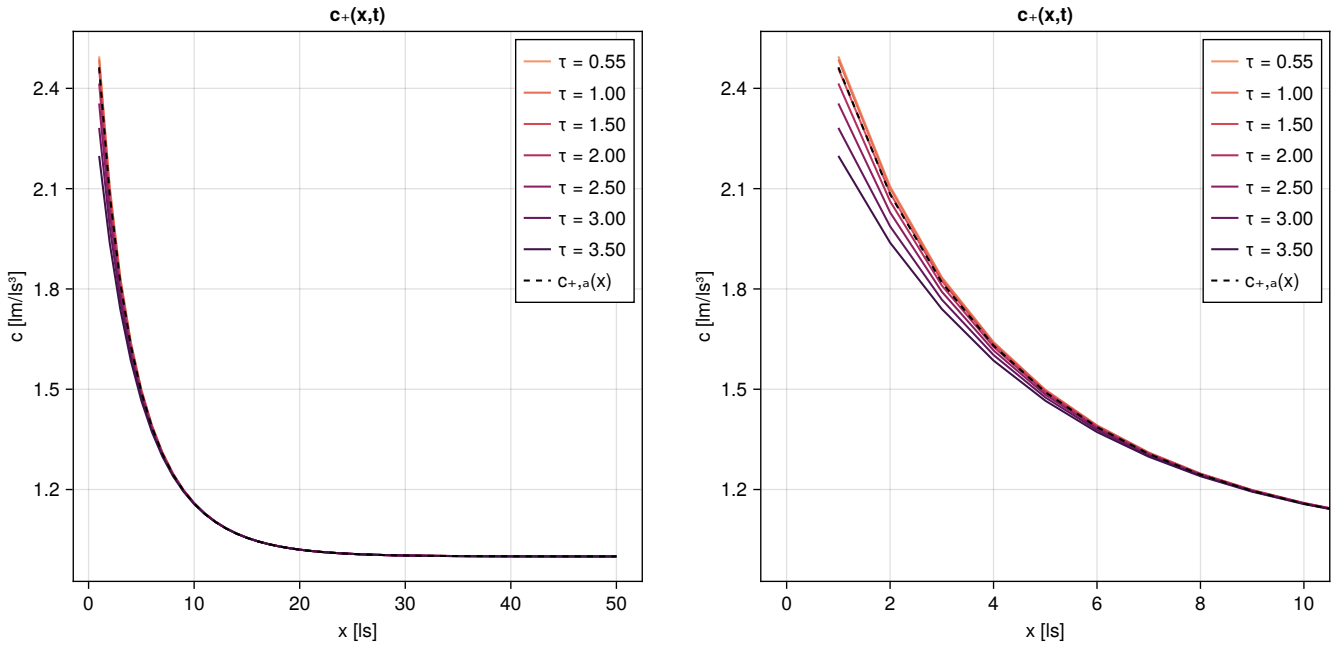


Figure A.1: The steady-state solutions of the p^+ concentration c_+ for a range of relaxation times τ_i. Although the steady-state solutions seem comparable to the analytical solution for the concentration $c_{+,a}$ (left), a discrepancy is observed close to the anodic boundary Γ_a (right): the simulation undershoots the analytical solution for the concentration $c_{+,a}$ for $\tau_i > 1.5$, and overshoots for $\tau_i < 0.5$.

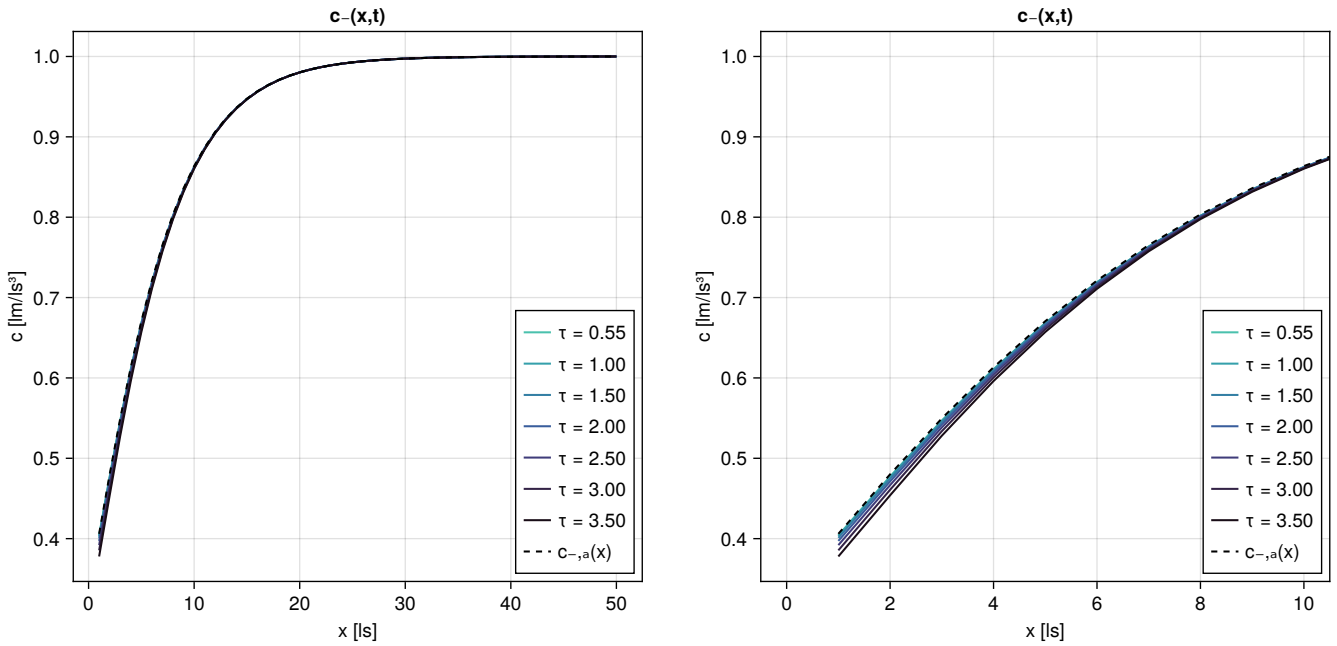


Figure A.2: The steady-state solutions of the n^- concentration c_- for a range of relaxation times τ_i. Although the steady-state solutions seem comparable to the analytical solution for the concentration $c_{-,a}$ (left), a discrepancy is observed close to the anodic boundary Γ_a (right): the simulation increasingly undershoots the analytical solution for the concentration $c_{+,a}$ as τ_i becomes larger.

A.2
Effects of the Relaxation (Pseudo-)time on the (Pseudo-)Steady-State Solutions

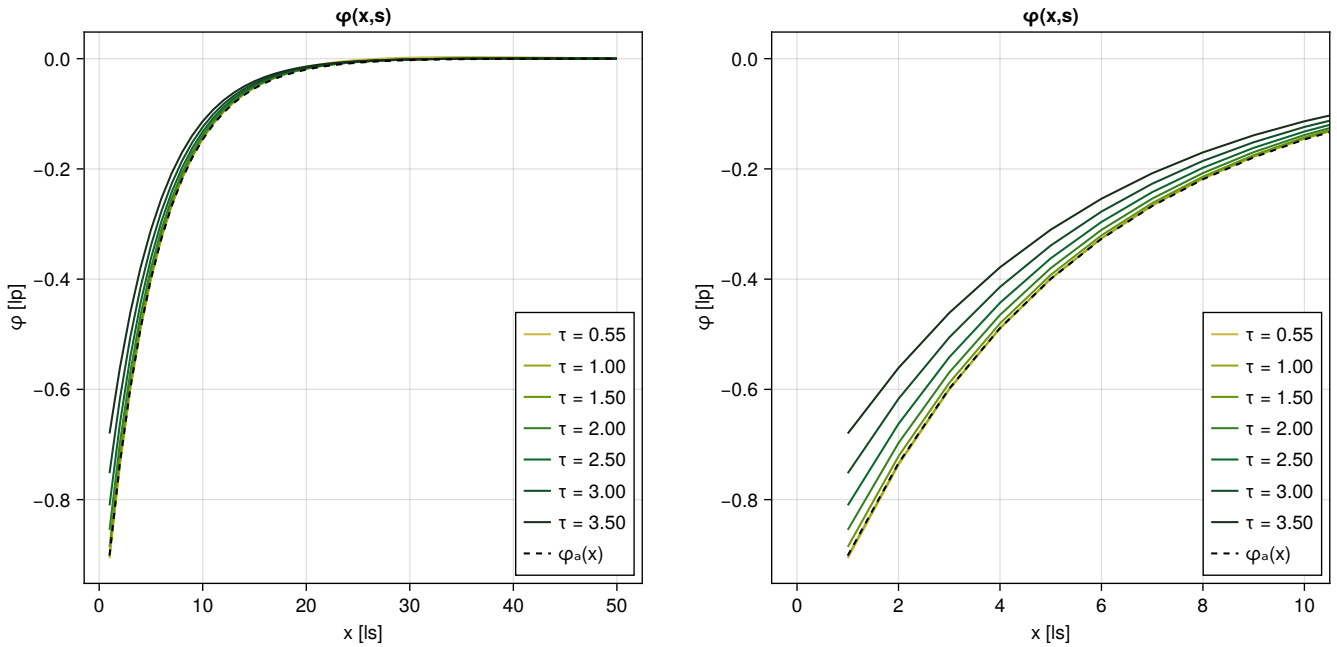


Figure A.3: The pseudo-steady-state solutions of the electric potential ϕ for a range of relaxation pseudo-times σ. Although the pseudo-steady-state solutions seem comparable to the analytical solution for the electric potential ϕ_a (left), a discrepancy is observed close to the anodic boundary Γ_a (right): the simulation undershoots the analytical solution for the electric potential ϕ_a for $\sigma < 1$, and overshoots for $\sigma > 1$.

Bibliography

Books

[1] M. H. Rashid. *Electric Renewable Energy Systems*. Ed. by M. H. Rashid. 1st ed. Academic Press, Nov. 2015.

[7] R. Chen, S. Kim, and Z. Chang. *Redox Flow Batteries: Fundamentals and Applications*. Ed. by M. Awad Ali Khalid. InTechOpen, Sept. 2017.

[12] Willem Haverkort. *Electrolysers, Fuel Cells and Batteries: Analytical Modelling*. 2nd ed. TU Delft OPEN Publishing, Mar. 2025.

[16] Weiwei Caia et al. *Rotating Electrode Methods and Oxygen Reduction Electrocatalysts*. Ed. by Wei Xing, Geping Yin, and Jiujun Zhang. Elsevier, 2014. Chap. 2, pp. 33–65.

[19] Andrew Zangwill. *Modern Electrodynamics*. 1st ed. Cambridge University Press, Feb. 2013.

[23] Timm Krüger et al. *The Lattice Boltzmann Method: Principles and Practice*. 1st ed. Graduate Texts in Physics. Springer, 2017.

[28] Harry Van den Akker and Robert F. Mudde. *Transport Phenomena: The Art of Balancing*. 1st ed. Delft Academic Press, 2014.

[35] James G. Speight. *Lange's Handbook of Chemistry*. 16th ed. McGraw-Hill, 2005.

[36] J. M. Thijssen. *Computational Physics*. 2nd ed. Cambridge University Press, 2007.

Articles

[2] F. Pan et al. "Redox Targeting of Anatase TiO2 for Redox Flow Lithium-Ion Batteries". In: *Advanced Energy Materials* 4 (2014).

[3] A. A. Kebede et al. "A comprehensive review of stationary energy storage devices for large scale renewable energy sources grid integration". In: *Renewable and Sustainable Energy Reviews* 159 (May 2022).

[4] A. Ashok and A. Kumar. "A comprehensive review of metal-based redox flow batteries: progress and perspectives". In: *Green Chemistry Letters and Reviews* 17.1 (Jan. 2024).

[5] H. Du et al. "Side Reactions/Changes in Lithium-Ion Batteries: Mechanisms and Strategies for Creating Safer and Better Batteries". In: *Advanced Materials* 36.29 (May 2024).

[6] J. Zheng et al. "Development Overview and Perspective of Semi-Solid Flow Batteries". In: *Batteries and Supercaps* 7.12 (Sept. 2024).

[8] E. Ventosa. "Semi-solid flow battery and redox-mediated flow battery: two strategies to implement the use of solid electroactive materials in high-energy redox-flow batteries". In: *Current Opinion in Chemical Engineering* 37 (Sept. 2022).

[9] E. Sánchez-Díez et al. "Redox flow batteries: Status and perspective towards sustainable stationary energy storage". In: *Journal of Power Sources* 481 (Jan. 2021).

[10] B. Zhang et al. "Tuning Zn2+ coordination tunnel by hierarchical gel electrolyte for dendrite-free zinc anode". In: *Science Bulletin* 67.9 (May 2022).

[13] Jian-Feng Xiong et al. "Recent progress of in-situ/operando characterization approaches of zinc-air batteries". In: *Chemical Synthesis* 9.19905 (July 2019).

[14] Shouguang Yao et al. "Simulation of dendritic growth of a zinc anode in a zinc–nickel single flow battery using the phase field-lattice Boltzmann method". In: *New Journal of Chemistry* 45 (Dec. 2020), pp. 1838–1852.

[15] Shiwen Deng et al. "The effect of current density on zinc deposition characteristics in zinc ion batteries". In: *Surfaces and Interfaces* 80.108281 (Dec. 2025).

[17] M. E. McMahon, R. J. Santucci Jr, and J. R. Scully. "Advanced chemical stability diagrams to predict the formation of complex zinc compounds in a chloride environment". In: *RSC Advances* 4.7 (Jan. 2024).

[18] Jukai Chen et al. "Localized corrosion behavior on a heterogeneous surface involving multicomponent reactive transport and morphology evolution". In: *Asia-Pacific Journal of Chemical Engineering* 20.2 (Oct. 2024).

[20] Long Jiang et al. "Electric double layer design for Zn-based batteries". In: *Energy Storage Materials* 62.102932 (Sept. 2023).

[21] H. J. Li, H.J.H. Clercx, and F. Toschi. "A study with the lattice Boltzmann method on the conversion efficiency of a packed-bed reactor with different oriented packed beads configurations". In: *Physics of Fluids* 34.11 (Nov. 2022).

[22] Xiaoyi He and Ning Li. "Lattice Boltzmann simulation of electrochemical systems". In: *Computer Physics Communications* 129 (2000).

[24] Zhenhua Chai and Baochang Shi. "A novel lattice Boltzmann model for the Poisson equation". In: *Applied Mathematical Modelling* 32 (June 2007).

[25] Jun Li et al. “Lattice Boltzmann Boundary Conditions for Flow, Convection-Diffusion and MHD Simulations”. In: *Applied Mathematical Modelling* 153 (Oct. 2025).

[26] Michael Junk and Zhaoxia Yang. “Outflow boundary conditions for the lattice Boltzmann method”. In: *Progress in Computational Fluid Dynamics* 8.1-4 (2008), pp. 38–48.

[27] François Dubois, Pierre Lallemand, and Mohamed Mahdi Tekitek. “On anti bounce back boundary condition for lattice Boltzmann schemes”. In: *Computers & Mathematics with Applications* 79.3 (Feb. 2020), pp. 555–575.

[29] Arūnas Burlingis and Rosita Norvaišienė. “Determination of the Optimal Fourier Number on the Dynamic Thermal Transmission”. In: *International Journal of Thermophysics* (Dec. 2016).

[30] Fabrizio Capuani, Ignacio Pagonabarraga, and Daan Frenkel. “Discrete solution of the electrokinetic equations”. In: *Journal of Chemical Physics* 121.2 (Apr. 2004).

[32] Shilin Mao et al. “An anisotropic lattice Boltzmann - phase field model for dendrite growth and movement in rapid solidification of binary alloys”. In: *npj Computational Materials* 10.63 (Mar. 2024).

[33] László Rátkai, Tamás Pusztai, and László Gránásy. “Phase-field lattice Boltzmann model for dendrites growing and moving in melt flow”. In: *npj Computational Materials* 5.113 (Nov. 2019).

[34] Rui Liu et al. “Pore-scale study of dynamic ion adsorption process in porous electrodes of capacitive deionization using lattice Boltzmann method”. In: *International Journal of Heat and Mass Transfer* 135 (Feb. 2019), pp. 769–781.

[37] Kazem Hejranfar, Hossein Hashemi Nasab, and Mohammad Hadi Azampour. “Arbitrary Lagrangian-Eulerian unstructured finite-volume lattice-Boltzmann method for computing two-dimensional compressible inviscid flows over moving bodies”. In: *Physical Review E* 101.023308 (Feb. 2020).

[38] Hiroaki Yoshida and Makoto Nagaoka. “Multiple-relaxation-time lattice Boltzmann model for the convection and anisotropic diffusion equation”. In: *Journal of Computational Physics* 229.20 (Oct. 2010), pp. 7774–7795.

Websites

[11] ReZilient. *The ReZilient project*. `https://rezilientproject.eu/`. 2023.

[31] COMSOL. *Detailed Explanation of the Finite Element Method (FEM)*. `https://www.comsol.com/multiphysics/finite-element-method`. Feb. 2017.

[39] Julia Programming Language. *Parallel Computing*. `https://docs.julialang.org/en/v1/manual/parallel-computing/`. Apr. 2026.